Graz University of Technology

Richard SCHUSSNIG BSc

Isoparametric Mixed Finite Elements in Kirchhoff-Love Plate Theory

MASTER'S THESIS

to achieve the university degree of

Diplom-IngenieurIn

Master's degree programme: Civil Engineering and Structural Engineering

submitted to

Graz University of Technology

Supervisor

Univ.-Prof. Dr.-Ing. habil. Thomas Peter Fries

Institute of Structural Analysis

Graz, May 2017

Affidavit

I declare that I have authored this thesis independently, that I have not used other than the declared sources/resources, and that I have explicitly indicated all material which has been quoted either literally or by content from the sources used. The text document uploaded to TUGRAZonline is identical to the present master's thesis.

Graz, May 2017 _____

Acknowledgements

I wish to express my deep sense of gratitude to Univ.-Prof. Dr.-Ing. habil. T.P. Fries for his valuable guidance, continuous encouragement and the numerous keen suggestions, which contributed immensely to the evolution of this work.

My sincerest thanks to every member of staff at the Institute of Structural Analysis for providing their help throughout various stages of development and countless discussions I could profit so much from.

Finally, my heartfelt thanks to my family and friends, without their endless and unconditional support the completion of this thesis would not have been possible.

Abstract

Within this thesis the biharmonic boundary value problem of the static isothermic Kirchhoff-Love plate with constant thickness is formulated as a system of four second order partial differential equations in the deflection and the internal moments of the plate. An isoparametric approach is chosen based on Lagrange finite elements in a conforming method.

The boundary conditions of the Kirchhoff-Love plate on curved boundaries are considered via Lagrange multipliers within the mixed weak formulation of the boundary value problem. Three different approaches to enforce boundary conditions to model simply supported, clamped, free or symmetry boundaries are investigated. The first two methods prescribe Neumann boundary conditions via evaluation of boundary terms and Dirichlet boundary conditions via the Point Collocation Method or Lagrange multipliers discretised by mapped Lagrange polynomials. The third method enforces both essential and natural boundary conditions by introducing Lagrange multipliers discretised by mapped Lagrange polynomials of different order.

The presented mixed formulations are verified with convergence studies using well-known analytical solutions of rectangular and circular plates as well as manufactured solutions for arbitrarily shaped domains with curved boundaries.

Zusammenfassung

Diese Arbeit befasst sich mit der approximativen Lösung der statischen isothermen Kirchhoff-Love Platte, deren Grundgleichung eine partielle Differentialgleichung vierter Ordnung ist. Um global stetige Ansatzfunktionen verwenden zu können wird die Bipotentialgleichung in ein System von vier partiellen Differentialgleichungen in der Durchbiegung und den Biege- und Torsionsmomenten überführt. Isoparametrische Lagrange Elemente werden eingesetzt, um die Lösung der Kirchhoff-Love Platte in krummlinig berandeten Gebieten näherungsweise zu berechnen.

Die Randbedingungen der Kirchhoff-Love Platte für momentenfrei gelagerte, eingespannte sowie freie Ränder und Symmetrieränder werden mit Lagrange'schen Multiplikatoren in schwacher Form erzwungen. Drei Methoden, die Randbedingungen vorzuschreiben, werden vorgestellt. Die ersten beiden Methoden setzen Neumann-Randbedingungen über die Auswertung der Randterme und die Dirichlet Randbedingungen über Lagrange Multiplikatoren in einem Punkt-Kollokationsverfahren bzw. mit abgebildeten Lagrange Polynomen am Rand des Gebietes. Die dritte präsentierte Methode erzwingt natürliche als auch essentielle Randbedingungen über Lagrangesche Multiplikatoren, diskretisiert durch Lagrange-Polynome von unterschiedlicher Ansatzordnung in schwacher Form.

Die Validierung der gemischten Formulierungen wird anhand von Konvergenzstudien mehrerer Testfälle vorgenommen. Dabei werden zum Vergleich Referenzlösungen mechanischer Probleme auf rechteckigen und runden Platten verwendet, oder für beliebige Platten mit krummlinigen Rändern Lösungen basierend auf der "method of manufactured solutions".

Contents

Notation

a	Scalar
$\boldsymbol{n}$	Vector
$\boldsymbol{R}$	Matrix or tensor
$\boldsymbol{R}^\top$	Transposed matrix or tensor
$w_{,i}$	Derivative of w with respect to i
Δ^2	biharmonic operator
Ω	Real domain
Γ_D	Dirichlet boundary
Γ_w	Dirichlet boundary with prescribed w
Γ_{m_n}	Dirichlet boundary with prescribed m_n
Γ_N	Neumann boundary
$\Gamma_{w,_n}$	Neumann boundary with prescribed $w_{,n}$
$\Gamma_{\bar{q}_n}$	Neumann boundary with prescribed $\bar{q}_n$
n_i	Component of the unit outward normal vector in direction i
w	Deformation of the plate normal to the mid-plane surface, bending
β_i	Angle of inclination of the mid-plane surface of the plate in direction i
p	Surface load per unit area acting on the plate
t	Thickness of the plate
E	Young's modulus
ν	Poisson's ratio
$\boldsymbol{\sigma}$	Linearised Cauchy stress tensor
K	Bending stiffness, flexural rigidity of the plate
m_i	Bending or twisting moment per unit length in direction i
q_i	Transverse shear force per unit length in direction i
$\bar{q}_i$	Effective shear force per unit length in direction i
F_c	Force concentrated in the corners of the plate
$\hat{w}$	Prescribed value, shown for w here

1 Introduction

Thin plates as widely used structural members are modelled as two-dimensional solids, loaded in perpendicular direction to the midsurface of the plane plate. The assumptions of *Kirchhoff* [12] lead to a governing partial differential equation of fourth order for the deflection normal to the midsurface. Within the Kirchhoff-Love plate theory, strains are defined as functions of the second derivatives of the displacement w. As a result the inter-element continuity conditions are imposed on the deflections as well as on their derivatives. These conditions may be met e.g. via construction of $\mathcal{C}^1$-continuous finite elements or applying mixed or hybrid variational formulations [18, 4, 5].

Within this thesis the governing equation of the static isothermic Kirchhoff-Love plate with constant thickness is, following *Ahrens et al.* [1], formulated as a system of four second order partial differential equations, such that the continuity requirements are reduced to $\mathcal{C}^0$ and the internal moments of the thin plate are directly obtained from solving the emerging linear system of equations. Lagrange elements are therefore sufficient and used in an isoparametric approach, which is easily incorporated in an existing finite element code.

The boundary conditions of the Kirchhoff-Love plate on curved polygonal boundaries are presented and introduced as Lagrange multipliers into the mixed weak formulation of the boundary value problem. In doing so three approaches were taken to prescribe Neumann and Dirichlet data along the boundary of the domain. Within the first two methods, Neumann boundary conditions are enforced via the evaluation of boundary terms and Dirichlet boundary conditions on the one hand via Lagrange multipliers discretised by spaces of Dirac-delta functions, which is known as the Point Collocation Method [8], or on the other hand via mapped one-dimensional Lagrange Polynomials. The third method introduces Lagrange multipliers for both essential and natural boundary conditions, which are discretised by mapped one-dimensional Lagrange polynomials of different order.

The arising minimization problem under linear constraints must fulfil the Babuška-Brezzi stability criterion which is shown numerically by completion of convergence studies using solutions obtained via the manufactured solution method as well as several other reference solutions on a non-uniform mesh with curved boundaries. For the mathematical analysis of this problem the reader is referred to *Babuška* [3], *Boffi et al.* [5], *Brezzi* [6] , *Ciarlet et al.* [7] and the references therein. In the numerical results, it is shown that higher-order convergence rates are achieved for a number of different problems. Thereby, it is found that a mixed FEM is a very attractive method for approximating Kirchhoff-Love plates with no need for increased continuity requirements.

2 Kirchhoff-Love Plate Theory

The Kirchhoff-Love plate theory or classical plate theory was first derived by *Love* [13] based on assumptions proposed by *Kirchhoff* [12]. For thin plates this theory yields satisfactory results considering lateral loading or bending moments acting along the boundary of the plate and is therefore widely used in engineering science as well as in engineering practice.
Within the classical plate theory, the following assumptions are made [17]:

- The midsurface of the plate remains neutral during the whole deformation, i.e. strains in the middle plane are neglected.
- Points on a plane normal to the midsurface remain on the plane normal to the midsurface after deformation.
- The normal stress component in thickness direction σ_{zz} is negligible compared to the in-plane normal stresses σ_{xx} and σ_{yy}.

Within this thesis bending of homogeneous isotropic and isothermic plates with constant thickness and time independent behaviour are considered. The constitutive relation applied is the generalized linear-elastic Hook's law. In combination with the restrictions stated above this implies a plane stress state. The a-priori non-zero shear components of the linearised Cauchy stress tensor $\boldsymbol{\sigma}$ are directly linked to the transverse loading p via equilibrium and do not contribute to plate deflection. Thus all stress and strain components at every point in the plate are described as functions of the transverse displacement w. The governing linear partial differential equation on the domain Ω is therefore expressed solely in w and together with Dirichlet and Neumann boundary conditions on the corresponding partitions of the boundary of the domain Γ_{D} and Γ_{N} complete the boundary value problem. In the following the underlying model equations taken from [17, 2] are summarized using a Cartesian coordinate system. Matrix notation is avoided for the sake of simplicity when deriving the needed boundary terms.

2.1 Kinematics

Due to the small deflections of the plate linearization is carried out and the curvature κ of any given plane parallel to the midplane surface is written in terms of the deflection w. As depicted in figure 2.1, the following relations may be derived using the plates angle of inclination β_i at the point in i-direction and the in-plane displacements u_x and u_y:

$$\begin{gathered}
\beta_x := w_{,x} \quad , \quad \beta_y := w_{,y} \\
u_x := -sin(\beta_x)\, z \approx -\beta_x\, z \quad , \quad u_y := -sin(\beta_y)\, z \approx -\beta_y\, z \\
\kappa_x := -\beta_{x,x} = -w_{,xx} \quad , \quad \kappa_y := -\beta_{y,y} = -w_{,yy} \quad , \quad \kappa_{xy} := -\beta_{x,y} = -w_{,xy} = -\beta_{y,x} =: \kappa_{yx}
\end{gathered} \tag{2.1}$$

The strains in x and y directions due to pure bending of a thin plate at a distance z from the neutral midplane surface are:

$$\epsilon_{xx} = u_{x,x} = z\,\kappa_x \quad , \qquad \epsilon_{yy} = u_{y,y} = z\,\kappa_y \tag{2.2}$$

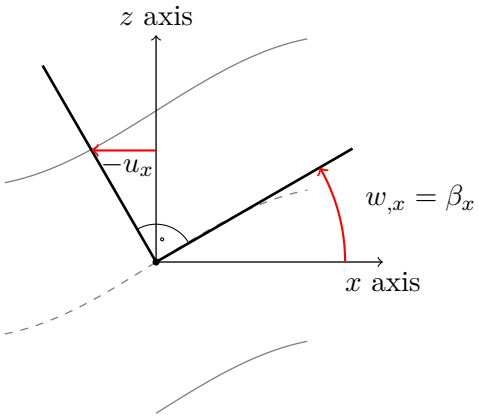

Fig. 2.1: Kinematics of a thin plate in x-direction

The non-zero shear strain components are:

$$\gamma_{xy} = \gamma_{yx} := u_{x,y} + u_{y,x} = \beta_{x,y} + \beta_{y,x} = -2z\, w_{,xy} = 2z\, \kappa_{xy} \tag{2.3}$$

The strains in the Kirchhoff-Love plate theory are linear functions in the distance from the midplane surface z and second derivatives of the deflection of the midplane surface, which are equal to the corresponding curvatures at any given point.

2.2 Internal Forces and Equilibrium

The assumption of pure plate bending, allowing for transverse loading and bending moments per unit length acting on the Neumann boundary Γ_{N}, implies that the normal stress components are integrated over the thickness of the plate resulting in expressions for the bending moments m_x and m_y and the twisting moment m_{xy} all defined per unit length:

$$m_x := \int_{-t/2}^{t/2} \sigma_{xx}\, z \quad \mathrm{d}z \quad , \qquad m_y := \int_{-t/2}^{t/2} \sigma_{yy}\, z \quad \mathrm{d}z \quad , \qquad m_{xy} = m_{yx} := \int_{-t/2}^{t/2} \tau_{xy}\, z \quad \mathrm{d}z \tag{2.4}$$

The equality of the twist moments per unit length m_{xy} and m_{yx} follows from the symmetry of the corresponding stresses, which is a necessary condition for fulfilling the balance of angular momentum [9] and can easily be seen considering equation 2.3.
Analogously to the normal stress components the shear stress components are integrated over the plate thickness resulting in the shear forces:

$$q_x := \int_{-t/2}^{t/2} \tau_{xz}\, z \quad \mathrm{d}z \quad , \qquad q_y := \int_{-t/2}^{t/2} \tau_{yz}\, z \quad \mathrm{d}z \tag{2.5}$$

In figure 2.2 all internal forces per unit length acting on a differential element of the plate are shown. Using the above relations 2.4 and 2.5 the linearized local balance of linear and angular momentum considering a surface loading per unit area $p(x, y)$ result in:

$$q_{x,x} + q_{y,y} = -p \tag{2.6}$$

$$m_{xy,x} + m_{y,y} = q_y \tag{2.7}$$

$$m_{x,x} + m_{yx,y} = q_x \tag{2.8}$$

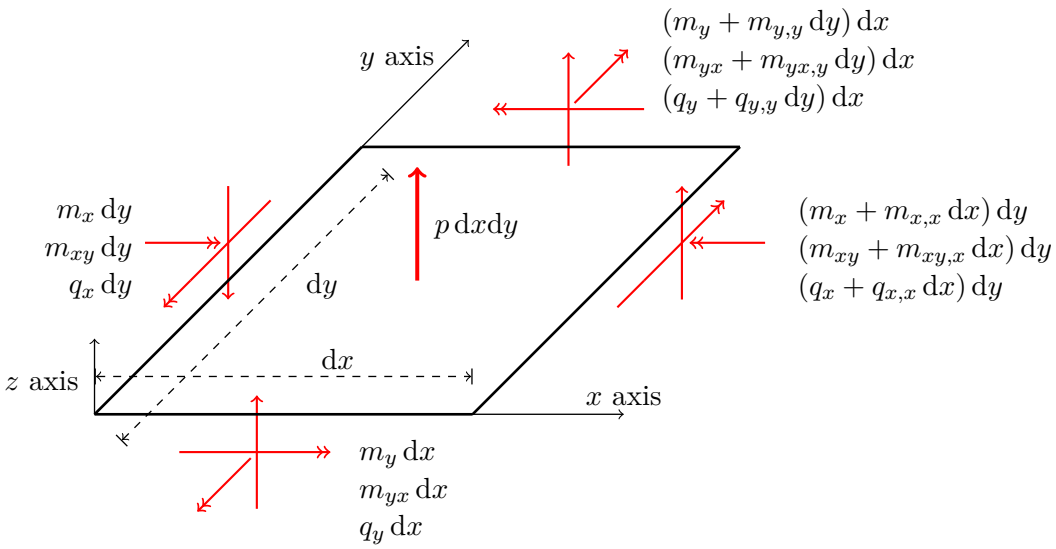

Fig. 2.2: Internal forces acting on a differential element of the Kirchhoff-Love plate

Substituting q_x and q_y in 2.6 and using $m_{xy} = m_{yx}$ from 2.4 yields the local equilibrium in terms of the bending and twisting moments per unit length of the plate:

$$m_{x,xx} + 2\,m_{xy,xy} + m_{y,yy} = -p \tag{2.9}$$

2.3 Constitutive relation

The generalized linear-elastic Hooks law for plain stress analysis neglecting normal stress components acting transversely to the midplane surface with Young's modulus E and Poisson's ratio ν yields:

$$\epsilon_{xx} := \frac{1}{E}\left(\sigma_{xx} - \nu\,\sigma_{yy}\right) \quad , \qquad \epsilon_{yy} := \frac{1}{E}\left(\sigma_{yy} - \nu\,\sigma_{xx}\right) \quad , \qquad \gamma_{xy} := \frac{2}{E}\left(1+\nu\right)\tau_{xy} \tag{2.10}$$

Using the equations 2.1, 2.2 and 2.4 from above the constitutive relation is expressed in terms of the moments per unit length and the flexural rigidity K of the plate:

$$\begin{aligned} m_x &= -K\left(w_{,xx} + \nu\,w_{,yy}\right) \\ m_y &= -K\left(w_{,yy} + \nu\,w_{,xx}\right) \\ m_{xy} &= -K\left(1-\nu\right)w_{,xy} \qquad \text{with :} \qquad K = \frac{E\,t^3}{12\left(1-\nu^2\right)} \end{aligned} \tag{2.11}$$

Substituting these expressions in the local equilibrium 2.9 results in the governing linear partial differential equation of Kirchhoff-Love plate bending:

$$w_{,xxxx} + 2\,w_{,xxyy} + w_{,yyyy} = \frac{p}{K} \qquad \text{or} \qquad \Delta^2\,w = \frac{p}{K} \tag{2.12}$$

Applying boundary conditions and solving equation 2.12 provides the deflection of the midplane surface $w(\boldsymbol{x})$ of the thin plate. In the process of designing a plate as a structural member not only the deformation, but also the internal forces, stresses and strains are of particular interest. Hence the following relations are provided to solve for the desired quantities in a postprocessing step, considering the deformation w and all bending and twisting moments m_x, m_y and m_{xy}, which are primary variables of the mixed method introduced in chapter 3.

2.4 Stress and strain recovery

The constitutive relation expressed in the internal forces of the Kirchhoff-Love plate in equations 2.11 is rewritten using the relation between the second derivative of the deflection and the curvature in equation 2.1 as:

$$\begin{aligned} \kappa_x &= \frac{1}{K\,(1-\nu^2)}\,(m_x - \nu\, m_y) \\ \kappa_y &= \frac{1}{K\,(1-\nu^2)}\,(m_y - \nu\, m_x) \\ \kappa_{xy} &= \frac{1}{K\,(1-\nu^2)}\,(1+\nu)\, m_{xy} \end{aligned} \tag{2.13}$$

Further inserting into 2.2 and 2.3 gives the following expressions of the strains as functions of the bending and twisting moments per unit length:

$$\begin{aligned} \epsilon_{xx} &= z\,\kappa_x = \frac{z}{K\,(1-\nu^2)}\,(m_x - \nu\, m_y) \\ \epsilon_{yy} &= z\,\kappa_y = \frac{z}{K\,(1-\nu^2)}\,(m_y - \nu\, m_x) \\ \gamma_{xy} &= 2z\,\kappa_{xy} = \frac{2z}{K\,(1-\nu^2)}\,(1+\nu)\, m_{xy} \end{aligned} \tag{2.14}$$

Finally using the constitutive relation 2.10 yields:

$$\sigma_x = \frac{12}{t^3}\, z\, m_x \quad , \qquad \sigma_y = \frac{12}{t^3}\, z\, m_y \quad , \qquad \tau_{xy} = \frac{12}{t^3}\, z\, m_{xy} \tag{2.15}$$

The shear stress components acting normal to the midplane surface of the plate is recovered most efficiently using the equilibrium equations 2.7 and 2.8, i.e. partially differentiating the bending and twisting moments m_x, m_y and m_{xy}:

$$\tau_{xz} = (m_{x,x} + m_{xy,y})\,\frac{6}{t^3}\left(\frac{t^2}{4} - z^2\right) \quad , \qquad \tau_{yz} = (m_{y,y} + m_{xy,x})\,\frac{6}{t^3}\left(\frac{t^2}{4} - z^2\right) \tag{2.16}$$

It is highlighted, that the strains are computed directly from the bending and twisting moments, while all entries of the linearised Cauchy stress tensor $\boldsymbol{\sigma}$ may only be recovered using the solutions to the mixed method as well as their first derivatives. Describing these quantities in terms of the deflection w of the plate results in relations involving higher derivatives. To preserve the numerical accuracy of the presented mixed method, the above relations are considered.
The boundary value problem consists of the partial differential equation of the Kirchhoff-Love plate in the domain Ω and appropriate Dirichlet and Neumann boundary conditions on the boundary $\partial\Omega$. To formulate the latter for arbitrarily shaped boundaries, transformation equations for the internal moments and shear forces are introduced in the next section.

2.5 Transformation equations

Considering the definitions of the bending and twisting moments and the shear forces per unit length in equations 2.4 and 2.5 the desired quantities may be derived by expressing the components of the stress tensor $\boldsymbol{\sigma}$ in a coordinate system rotated by an angle φ about the z axis, which is normal to the midplane surface [2]. The angle of rotation is defined positive in counter-clockwise direction, as depicted in figure 2.3.

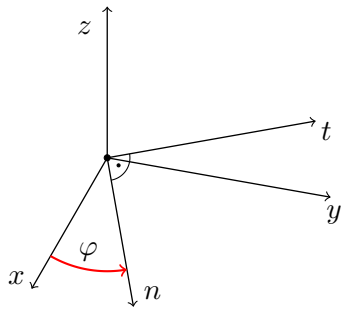

Fig. 2.3: xyz coordinate system and rotated ntz coordinate system

The second order tensor $\boldsymbol{\sigma}$ is transformed by pre- and postmultiplying with the orthogonal tensor of second order $\boldsymbol{R}$ and its transpose [9]:

$$\boldsymbol{R} = \begin{pmatrix} cos(\varphi) & -sin(\varphi) & 0 \\ sin(\varphi) & cos(\varphi) & 0 \\ 0 & 0 & 1 \end{pmatrix} \quad , \quad \text{with} \quad det\,(\boldsymbol{R}) = 1 \quad \text{and} \quad \boldsymbol{R}^{-1} = \boldsymbol{R}^{\top} \tag{2.17}$$

$$\boldsymbol{\sigma'} = \boldsymbol{R} \cdot \boldsymbol{\sigma} \cdot \boldsymbol{R}^{\top} \quad \Longleftrightarrow \quad \boldsymbol{\sigma} = \boldsymbol{R}^{\top} \cdot \boldsymbol{\sigma'} \cdot \boldsymbol{R} \tag{2.18}$$

Using the latter expression of equation 2.18 and the definitions of the internal forces in 2.4 and 2.5 the internal forces defined in a rotated coordinate system ntz are expressed in the initial xyz coordinate system:

$$\begin{aligned} m_n &= m_x\, cos^2(\varphi) + m_y\, sin^2(\varphi) + m_{xy}\, sin(2\,\varphi) \\ m_t &= m_x\, sin^2(\varphi) + m_y\, cos^2(\varphi) - m_{xy}\, sin(2\,\varphi) \\ m_{nt} &= (m_y - m_x)\, sin(\varphi)\, cos(\varphi) + m_{xy}\, cos(2\,\varphi) \\ q_n &= q_x\, cos(\varphi) + q_y\, sin(\varphi) \\ q_t &= -q_x\, sin(\varphi) + q_y\, cos(\varphi) \end{aligned} \tag{2.19}$$

The xyz coordinates of a point are transformed into the ntz coordinate system using:

$$x = n\, cos(\varphi) - t\, sin(\varphi) \quad , \qquad y = n\, sin(\varphi) + t\, cos(\varphi) \quad , \qquad z = z \tag{2.20}$$

Differentiating a scalar function $w(\boldsymbol{x})$ with respect to the ntz coordinates considering the chain rule gives:

$$\begin{aligned} w_{,n} &= w_{,x}\, x_{,n} + w_{,y}\, y_{,n} = w_{,x}\, cos(\varphi) + w_{,y}\, sin(\varphi) \\ w_{,t} &= w_{,x}\, x_{,t} + w_{,y}\, y_{,t} = -w_{,x}\, sin(\varphi) + w_{,y}\, cos(\varphi) \\ w_{,z} &= w_{,z} \end{aligned} \tag{2.21}$$

The above relations are used to formulate boundary conditions to model different types of physical boundaries of the Kirchhoff-Love plate. The emphasis therein lies on prescribing natural and essential boundary conditions on curved boundaries, which are later approximated using isoparametric finite elements. Robin or mixed boundary conditions, which may be utilised to model e.g. elastic supports, are not considered.

2.6 Boundary conditions

As the governing equation 2.12 of the Kirchhoff-Love plate is a fourth-order problem, enforcing two independent displacement or force quantities in every point of the boundary is sufficient and necessary

[2]. Revisiting the kinematics and kinetics of a differential plate element one may observe, that on a boundary of such an element of the plate three kinetic quantities, namely m_n, m_{nt} and q_n, and three kinematic quantities w, $w_{,n}$ and $w_{,t}$ are defined. The assumption of zero shear deformation in equation 2.1 of the plate allowed for a simplification and is inevitable for the model reduction in thin plate bending.
To circumvent this problem, the so-called effective shear force was introduced by *Kirchhoff* [12], which is a quantity defined per unit length.

2.6.1 Effective shear force

In a point on a arbitrarily shaped boundary of a thin plate the bending moment per unit length producing normal stresses in direction normal to the boundary m_n, the twisting moment per unit length m_{nt} as well as the shear force per unit length q_n, both the latter two producing shear stresses in the local tz plane, act as depicted in figure 2.4.

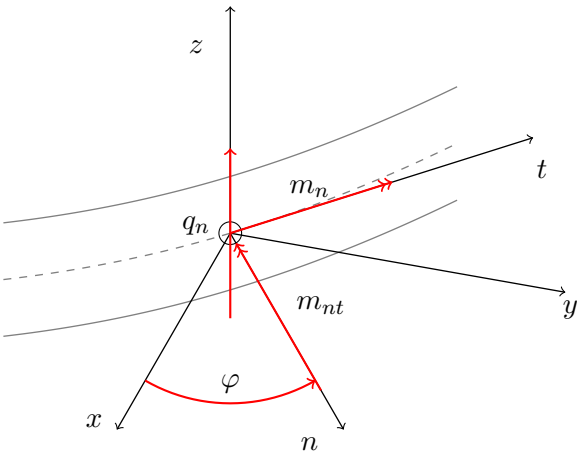

Fig. 2.4: Internal forces acting on an edge of a thin plate

Saint Venant's principle states, that the stress state of any given continuum does not change considerably, if a surface traction, which is in equilibrium with itself, is applied to a small partition of the surface of the continuum [2]. To reduce the number of boundary conditions to two, the twisting moment per unit length is decomposed statically equivalent into pairs of forces acting in the boundary-plane, as shown in figure 2.5.
This allows for the summation of the shear force q_n and the pair of forces induced by the twisting moment m_{nt} per unit length acting on the boundary [17, 2]:

$$\bar{q}_n = q_n + m_{nt,t} \tag{2.22}$$

The resulting disturbances in the stress state of the plate will only affect a small region alongside the boundary, which is of the same order as the thickness of the plate [17, 14]. Therefore a loss of accuracy is expected if the plate is comparatively thick or the influence of the part of the Neumann boundary, on which the effective shear force is prescribed $\Gamma_{\bar{q}_n} \subset \partial\Omega$, is not negligible.
It is noted, that the individual quantities of the shear force and the twisting moment per unit length are not prescribed individually. Hence it is not possible to apply boundary conditions on these quantities. Moreover prescribing the desired value for the effective shear force is not identically equal to prescribing the individual values and will in general not result in exactly the same values.
The decomposition of the twisting moment per unit length acting on the edge of the plate has a drastic consequence for the points on the boundary, in which a discontinuity of the twisting moment

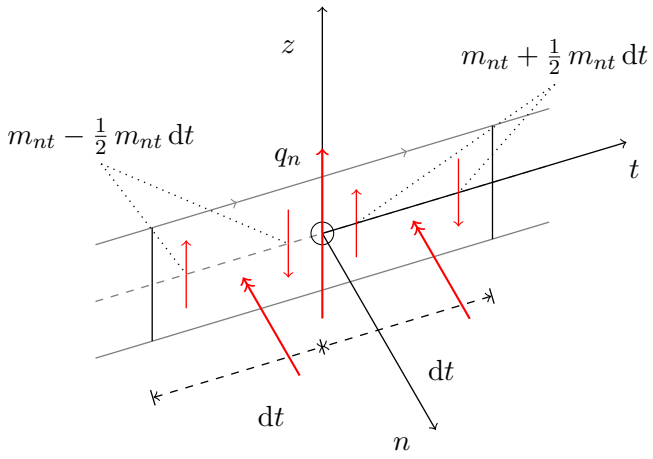

Fig. 2.5: Internal forces acting on an edge of a thin plate

per unit length is present. This is e.g. the case in the corners of the plate and at points, where the thickness of the plate changes. As depicted in figure 2.6, which shows a corner with two adjacent edges coinciding at an arbitrary angle, a force concentrated at the corner of the plate, denoted by F_c, arises [17, 2].

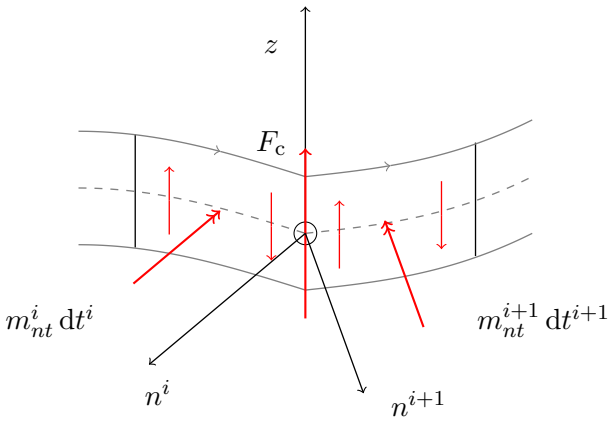

Fig. 2.6: Concentrated force in the corners F_c arising from the twisting moments

The force in the corner is a function of the twisting moments per unit length at the corner m_{nt}^{i} and m_{nt}^{i+1}, with i and $i+1$ indicating two consecutive boundary sections and equals the negative reaction force R_c in the corner [17, 2]:

$$F_\mathrm{c} = m_{nt}^{i+1} - m_{nt}^{i} = -R_\mathrm{c} \tag{2.23}$$

The successive sections of the boundary are defined positively in the counter-clockwise direction such that a positive i.e. lifting force in the corner F_c points into the positive z direction. After solving for the primary variables and utilising equations 2.19 the concentrated forces in the corners are computed in a postprocessing step:

$$\begin{aligned} F_\mathrm{c} &= (m_y - m_x)\left[sin(\varphi^{i+1})\, cos(\varphi^{i+1}) - sin(\varphi^{i})\, cos(\varphi^{i})\right] + \\ &\quad + m_{xy}\left[cos(2\,\varphi^{i+1}) - cos(2\,\varphi^{i})\right] \\ &= \frac{1}{2}\,(m_y - m_x)\left[sin(2\,\varphi^{i+1}) - sin(2\,\varphi^{i})\right] + m_{xy}\left[cos(2\,\varphi^{i+1}) - cos(2\,\varphi^{i})\right] \end{aligned} \tag{2.24}$$

An angle $\alpha = \frac{\pi}{2}$ of two neighbouring boundary sections gives a force in the corner equal to $F_c = -2\,m_{nt}$ for a simply supported plate and thus a lifting reaction force $R_c = 2\,|m_{xy}|$. For an angle $\alpha = 0$ or $\alpha = 2\,\pi$, which implies $\varphi^i = \varphi^{i+1}$, the resulting force in the corner vanishes.
The forces F_c are a consequence of the assumption of zero shear deformation made in the Kirchhoff-Love plate model, therefore choosing the thin plate bending model implies in general the presence of forces in the corners of the plate.
Nevertheless the force in the corner itself is not a boundary condition of the boundary value problem, but the bearing of the plate in the corners must withstand the arising forces. If the forces in the corners cannot build up, the load-bearing effect of a plate with shear deformations extends to the Reissner-Mindlin plate theory which is not considered herein [17].
The introduction of the effective shear force enables the derivation of the boundary conditions to model certain physical boundary types.

2.6.2 Clamped boundary

At a clamped boundary both the deflection w of a plate and the partial derivative of the bending surface normal to the edge of the plate $w_{,n}$ on Γ_w, $\Gamma_{w,n} \subset \partial\Omega$ are prescribed [17, 2]:

$$\begin{aligned} w\Big|_{\Gamma_w} &= \hat{w} && \text{with :} \quad \hat{w} && \ldots \text{ prescribed deflection} \\ w_{,n}\Big|_{\Gamma_{w,n}} &= \hat{w}_{,n} && \text{with :} \quad \hat{w}_{,n} && \ldots \text{ prescribed rotation} \end{aligned} \tag{2.25}$$

The partial derivative tangential to the boundary may, in general, be non-zero and depends on the given Dirichlet data for the deflection on the boundary Γ_w. Figure 2.7 shows the local ntz coordinate system at a point on the boundary of a plate and the prescribed values for a clamped edge.

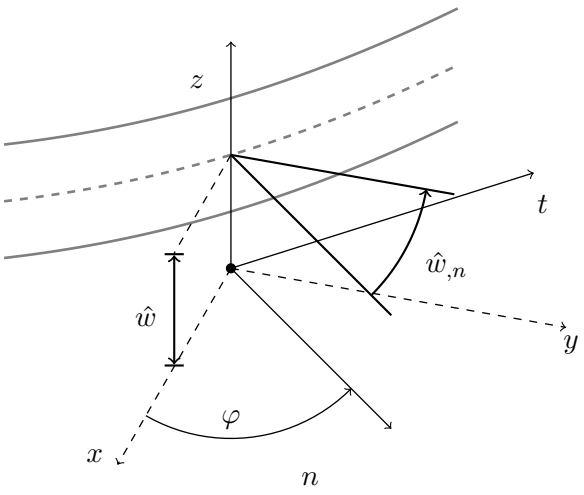

Fig. 2.7: Boundary conditions in w and $w_{,n}$ at a clamped boundary

2.6.3 Pinned boundary

The mathematical modelling of a pinned edge within thin plates includes prescribing Dirichlet data for both the deflections w and the bending moment per unit length m_n normal to the boundary $\Gamma_{m_n} \subset \partial\Omega$ [17, 2]:

$$w\Big|_{\Gamma_w} = \hat{w} \quad , \qquad m_n\Big|_{\Gamma_{m_n}} = \hat{m}_n$$

$$\text{with :} \qquad \hat{m}_n \quad ... \quad \text{prescribed bending moment} \tag{2.26}$$

Prescribing a value $\hat{m}_n$ for the internal bending moment is equivalent to loading the plate with an external bending moment with same magnitude but opposite sign. This follows from Cauchy's Lemma [9].
In figure 2.8 a pinned edge of a thin plate and the boundary conditions are depicted.

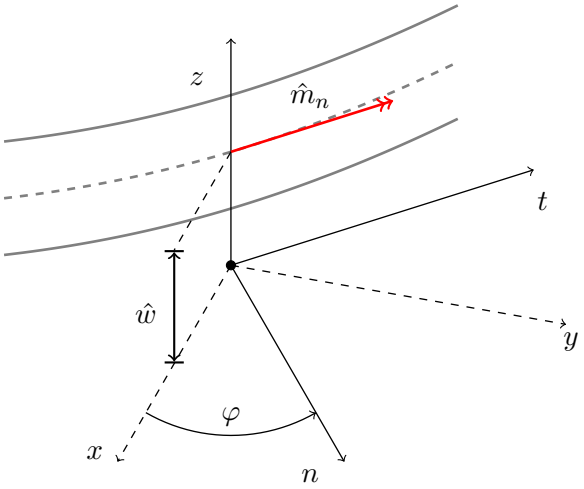

Fig. 2.8: Boundary conditions in w and m_n on a pinned boundary

2.6.4 Free boundary

A free edge in the Kirchhoff-Love plate theory is defined as a boundary, on which the bending moment per unit length m_n normal to the edge as well as the effective shear force $\bar{q}_n$ normal to the boundary $\Gamma_{\bar{q}_n} \subset \partial\Omega$ are prescribed [17, 2]:

$$m_n\Big|_{\Gamma_{m_n}} = \hat{m}_n \quad , \qquad \bar{q}_n\Big|_{\Gamma_{\bar{q}_n}} = \hat{\bar{q}}_n$$

$$\text{with :} \qquad \hat{\bar{q}}_n \quad ... \quad \text{prescribed effective shear force} \tag{2.27}$$

For inhomogeneous boundary conditions the loading terms considered must be introduced into equation 2.27 with an opposite sign due to Cauchy's lemma [9]. The convention for a positive effective shear force is illustrated in figure 2.9.

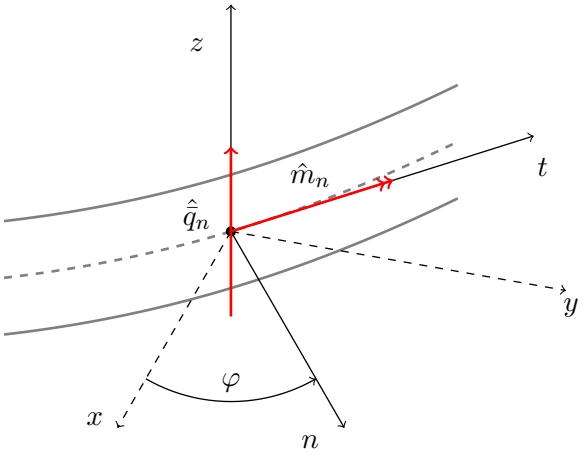

Fig. 2.9: Boundary conditions in m_n and $\bar{q}_n$ at a free boundary

2.6.5 Symmetry boundary

Symmetry boundary conditions are introduced into the present boundary value problem by prescribing Neumann boundary data for the partial derivative in normal direction to the boundary $w_{,n}$ and the effective shear force normal to the boundary $\bar{q}_n$ [17, 2]:

$$w_{,n}\Big|_{\Gamma_{w,n}} = 0 \quad , \qquad \bar{q}_n\Big|_{\Gamma_{\bar{q}n}} = 0 \tag{2.28}$$

As discussed thoroughly in 2.6.1 the individual quantities m_{nt} and q_n contributing to the effective shear force $\bar{q}_n$ are not enforced separately. Therefore these quantities will in general not fulfil the homogeneous Neumann boundary condition stated, but their sum will approximate the desired value. In figure 2.10 a symmetry boundary is depicted including the local ntz coordinate system.

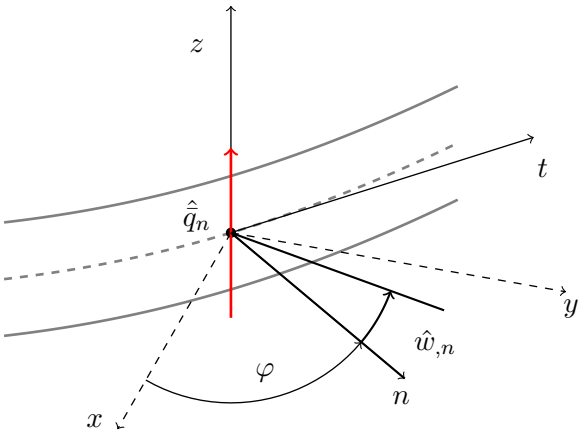

Fig. 2.10: Boundary conditions in $w_{,n}$ and $\bar{q}_n$ at a symmetry boundary

It is noted, that the twisting moment per unit length m_{nt} in the corners of the plate and therefore the force F_c is not part of any of the above boundary conditions. Nevertheless, using other variational formulations than the one presented within this thesis, they may be prescribed in terms of a single force loading at the corner, which is not considered. The influence of this inconsistency within the formulation of the problem is adressed in chapter 4.
The formulated boundary conditions complete the boundary value problem of Kirchhoff-Love plate bending.

3 Application of the Mixed Finite Element Method

Further analysis of the strong form of the governing equation of Kirchhoff-Love plate theory 2.12 reveals the need for an ansatz, whose function values as well as the first derivatives at interelement boundaries are globally continuous. The construction of $\mathcal{C}^1$-continuous shape functions, typically involving complex construction methods or Hermite-type elements, is circumvented utilising a mixed finite element formulation. Therefore Lagrange-type elements are sufficient for the approximation of the boundary value problem. In the following an approach using one field for the deflection and three fields for the internal moments of the Kirchhoff-Love plate with emphasis on the enforcement of both essential and natural boundary conditions is taken. For further mathematical analysis of the problem the reader is referred to *Boffi et al.* [5] and *Ciarlet et al.* [7] and the references therein.

3.1 Mixed Formulation of the Boundary Value Problem

The derivation of a multi-field formulation of the problem is based on [1] and reformulates equations 2.1, 2.9 and 2.13 from chapter 2, which are repeated at this point:

$$\kappa_x = -w_{,xx} \quad , \qquad \kappa_y = -w_{,yy} \quad , \qquad \kappa_{xy} = -w_{,xy} = \kappa_{yx} \tag{2.1 revisited}$$

$$m_{x,xx} + 2\, m_{xy,xy} + m_{y,yy} = -p \tag{2.9 revisited}$$

$$\begin{aligned} \kappa_x &= \frac{1}{K\,(1-\nu^2)}\,(m_x - \nu\, m_y) \\ \kappa_y &= \frac{1}{K\,(1-\nu^2)}\,(m_y - \nu\, m_x) \\ \kappa_{xy} &= \frac{1}{K\,(1-\nu^2)}\,(1+\nu)\, m_{xy} \end{aligned} \tag{2.13 revisited}$$

The kinematic relation in Kirchhoff-Love plate theory enables one to combine the constitutive relation expressed in bending and twisting moments 2.13 and the kinematics 2.1 of the plate:

$$w_{,xx} + \frac{1}{K\,(1-\nu^2)}\,(m_x - \nu\, m_y) = 0 \tag{3.1}$$

$$w_{,yy} + \frac{1}{K\,(1-\nu^2)}\,(m_y - \nu\, m_x) = 0 \tag{3.2}$$

$$2\, w_{,xy} + \frac{2}{K\,(1-\nu^2)}\,(1+\nu)\, m_{xy} = 0 \tag{3.3}$$

The boundary value problem in strong form considering inhomogeneous Dirichlet and Neumann Boundary conditions is, given the plate Ω with flexural rigidity K and loading p in Ω:

$$
\left\{
\begin{array}{l}
\text{find } w,\ m_x,\ m_y \text{ and } m_{xy} \text{ in } \Omega, \text{ such that} \\
\\
\begin{aligned}
m_{x,xx} + 2\, m_{xy,xy} + m_{y,yy} &= -p && \text{in } \Omega \subset \mathbb{R}^2\,, \\
w_{,xx} + \frac{1}{K\,(1-\nu^2)}\,(m_x - \nu\, m_y) &= 0 && \text{in } \Omega \subset \mathbb{R}^2\,, \\
w_{,yy} + \frac{1}{K\,(1-\nu^2)}\,(m_y - \nu\, m_x) &= 0 && \text{in } \Omega \subset \mathbb{R}^2\,, \\
2\, w_{,xy} + \frac{2}{K\,(1-\nu^2)}\,(1+\nu)\, m_{xy} &= 0 && \text{in } \Omega \subset \mathbb{R}^2\,, \\
w &= \hat{w} && \text{on } \Gamma_w \subset \partial\Omega\,, \\
w_{,n} &= \hat{w}_{,n} && \text{on } \Gamma_{w,n} \subset \partial\Omega\,, \\
m_n &= \hat{m}_n && \text{on } \Gamma_{m_n} = \partial\Omega \setminus \Gamma_{w,n}\,, \\
\bar{q}_n &= \hat{\bar{q}}_n && \text{on } \Gamma_{\bar{q}_n} = \partial\Omega \setminus \Gamma_w\,.
\end{aligned}
\end{array}
\right. \tag{3.4}
$$

It is noted that matrix notation is not introduced, since the field equations in 3.4 are rewritten to apply the Neumann boundary conditions.
In the following the derivation of the weak form of the boundary value problem and three methods to prescribe Neumann and Dirichlet data are presented.

3.2 Weak Form of the Multi-Field Boundary Value Problem

To derive a variational formulation of the boundary value problem, each field-equation in 3.4 is multiplied by a test function, indicated by ϕ, before integration over the domain is carried out. Integration by parts leads to line integrals and evaluations in the corners of the plate, through which one may enforce the Neumann boundary conditions. Alternatively the Neumann boundary conditions may be enforced adopting other methods, out of the numerous possibilities the method chosen is to introduce Lagrange multipliers denoted by λ with corresponding test functions μ.
For both the deflection of the plate w and the bending moment m_n Dirichlet boundary conditions on the respective boundaries must hold, but the bending moment normal to an edge is not a primary variable of any field. Therefore the Lagrange Multiplier Method is utilised again.
The stiffness matrix of an element is formulated based on the following methods, which will be referred to as method 1, 2 and 3 in the following, to impose the boundary conditions:

Methods used to apply Boundary Conditions

1. Enforce Dirichlet boundary conditions via Lagrange multipliers, discretised by a space of Dirac delta functions, whose degrees of freedom live on the respective boundary, and apply Neumann boundary conditions via evaluation of line integrals and evaluations in the corners added to the stiffness matrix.
2. Same as above, but discretise the Lagrange multipliers by a space of mapped Lagrange shape functions.
3. Enforce both the Dirichlet and Neumann boundary conditions via Lagrange multipliers, discretised by spaces of mapped Lagrange shape functions of different polynomial degree.

Multiplying each field-equation in 3.4 by a test function and integrating over the domain gives:

$$\int_\Omega \phi_w \, (m_{x,xx} + 2\, m_{xy,xy} + m_{y,yy}) \quad \mathrm{d}\Omega = -\int_\Omega \phi_w \, p \quad \mathrm{d}\Omega \tag{3.5}$$

$$\int_\Omega \phi_{m_x} \, w_{,xx} \quad \mathrm{d}\Omega + \int_\Omega \phi_{m_x} \, \frac{1}{K\,(1-\nu^2)} \, (m_x - \nu\, m_y) \quad \mathrm{d}\Omega = 0 \tag{3.6}$$

$$\int_\Omega \phi_{m_y} \, w_{,yy} \quad \mathrm{d}\Omega + \int_\Omega \phi_{m_y} \, \frac{1}{K\,(1-\nu^2)} \, (m_y - \nu\, m_x) \quad \mathrm{d}\Omega = 0 \tag{3.7}$$

$$\int_\Omega \phi_{m_{xy}} \, 2\, w_{,xy} \quad \mathrm{d}\Omega + \int_\Omega \phi_{m_{xy}} \, \frac{2}{K\,(1-\nu^2)} \, (1+\nu)\, m_{xy} \quad \mathrm{d}\Omega = 0 \tag{3.8}$$

Next, all of the field equations are reformulated, such that only first derivatives remain and the Neumann and Dirichlet boundary conditions may be prescribed by evaluating line integrals on the corresponding boundaries if needed.

3.2.1 Recasting Equation 3.5

The local equilibrium is rewritten such that Neumann boundary conditions on $\bar{q}_n$ may be prescribed and only first derivatives of the test functions remain. Integration by parts of equation 3.5 and introducing line loads $\hat{q}_x$ and $\hat{q}_y$ leads to:

$$\begin{aligned}
&-\int_\Omega \phi_{w,x}\, m_{x,x} \quad \mathrm{d}\Omega \quad &&+\int_\Gamma \phi_w \, m_{x,x}\, n_x \quad \mathrm{d}\Gamma \\
&-\int_\Omega \phi_{w,y}\, m_{y,y} \quad \mathrm{d}\Omega \quad &&+\int_\Gamma \phi_w \, m_{y,y}\, n_y \quad \mathrm{d}\Gamma \\
&-\int_\Omega \phi_{w,x}\, m_{xy,y} \quad \mathrm{d}\Omega \quad &&+\int_\Gamma \phi_w \, m_{xy,y}\, n_x \quad \mathrm{d}\Gamma \\
&-\int_\Omega \phi_{w,y}\, m_{xy,x} \quad \mathrm{d}\Omega \quad &&+\int_\Gamma \phi_w \, m_{xy,x}\, n_x \quad \mathrm{d}\Gamma \\
=&-\int_\Omega \phi_w \, p \quad \mathrm{d}\Omega \quad &&-\int_\Gamma \phi_w \, (\hat{q}_x\, n_x + \hat{q}_y\, n_y) \quad \mathrm{d}\Gamma
\end{aligned} \tag{3.9}$$

The line loads $\hat{q}_x$ and $\hat{q}_y$ correspond to the shear forces inside the domain on *inter*element boundaries and may be used to prescribe a line load $\hat{q}_n$ on a curved interelement boundary. Nevertheless these terms are dropped for simplicity.
Using the equations of local equilibrium in terms of the internal forces of the plate 2.7 and 2.8,

$$m_{xy,x} + m_{y,y} = q_y \qquad \text{(2.7 revisited)}$$
$$m_{x,x} + m_{yx,y} = q_x \qquad \text{(2.8 revisited)}$$

the boundary terms may be rewritten as:

$$\int_\Gamma \phi_w \left[(m_{x,x} + m_{xy,y})\, n_x + (m_{y,y} + m_{xy,y})\, n_y \right] \quad \mathrm{d}\Gamma \quad = \quad \int_\Gamma \phi_w \, (q_x\, n_x + q_y\, n_y) \quad \mathrm{d}\Gamma \tag{3.10}$$

To prescribe Neumann boundary data for the effective shear force $\bar{q}_n = \hat{\bar{q}}_n$ via evaluation of the boundary terms, the definition of effective shear force 2.22 as well as transformation equations of the internal forces 2.19 are used:

$$\begin{aligned} \bar{q}_n = \quad & q_n & & + m_{nt,t} \quad = \\ = \quad & q_x\, cos(\varphi) + q_y\, sin(\varphi) & & + \frac{\partial}{\partial t}\left[(m_y - m_x)\, sin(\varphi)\, cos(\varphi) + m_{xy}\, cos(2\,\varphi)\right] \end{aligned} \tag{3.11}$$

$$\implies \quad \bar{q}_n = \hat{\bar{q}}_n = q_n + m_{nt,t} \qquad \Longleftrightarrow \begin{cases} q_x = (\hat{\bar{q}}_n - m_{nt,t} - q_y\, sin(\varphi))\, \frac{1}{cos(\varphi)} \\ q_y = (\hat{\bar{q}}_n - m_{nt,t} - q_x\, cos(\varphi))\, \frac{1}{sin(\varphi)} \end{cases} \tag{3.12}$$

Further using $n_x = cos(\varphi)$ and $n_y = sin(\varphi)$ and inserting 3.12 into 3.10 gives:

$$\begin{aligned} & \int_{\Gamma_{\bar{q}_n}} \phi_w\ (q_x\, n_x + q_y\, n_y) \quad \mathrm{d}\Gamma_{\bar{q}_n} \quad = \\ = \quad & \int_{\Gamma_{\bar{q}_n}} \phi_w \left[\frac{\overbrace{n_x}^{=1}}{cos(\varphi)} (\hat{\bar{q}}_n - m_{nt,t} - q_y\, sin(\varphi)) + \frac{\overbrace{n_y}^{=1}}{sin(\varphi)} (\hat{\bar{q}}_n - m_{nt,t} - q_x\, cos(\varphi)) \right] \quad \mathrm{d}\Gamma_{\bar{q}_n} \quad = \\ = \quad & \int_{\Gamma_{\bar{q}_n}} \phi_w \left[\hat{\bar{q}}_n - (m_{y,y} - m_{xy,x})\, sin(\varphi) + \hat{\bar{q}}_n - (m_{x,x} - m_{xy,y})\, cos(\varphi) - 2\, m_{nt,t} \right] \quad \mathrm{d}\Gamma_{\bar{q}_n} \end{aligned}$$

In a final step the term involving the derivative of twisting moment in tangential direction $m_{nt,t}$ is rewritten using integration by parts and the transformation equations 2.19:

$$\begin{aligned} & \int_{\Gamma_{\bar{q}_n}} \phi_w \left[\hat{\bar{q}}_n - (m_{y,y} - m_{xy,x})\, sin(\varphi) + \hat{\bar{q}}_n - (m_{x,x} - m_{xy,y})\, cos(\varphi) - 2\, m_{nt,t} \right] \quad \mathrm{d}\Gamma_{\bar{q}_n} \quad = \\ = \quad & \int_{\Gamma_{\bar{q}_n}} \phi_w \left[2\, \hat{\bar{q}}_n - (m_{y,y} - m_{xy,x})\, sin(\varphi) - (m_{x,x} - m_{xy,y})\, cos(\varphi) \right] \quad \mathrm{d}\Gamma_{\bar{q}_n} \\ & + \int_{\Gamma_{\bar{q}_n}} 2\, \phi_{w,t}\, m_{nt} \quad \mathrm{d}\Gamma_{\bar{q}_n} - 2\, \phi_w\, m_{nt} \overbrace{n_t}^{=0}\Big|_{\mathrm{C}} \quad = \\ = \quad & - \int_{\Gamma_{\bar{q}_n}} \phi_w \left[(m_{y,y} - m_{xy,x})\, sin(\varphi) + (m_{x,x} - m_{xy,y})\, cos(\varphi) \right] \quad \mathrm{d}\Gamma_{\bar{q}_n} \\ & + \int_{\Gamma_{\bar{q}_n}} 2\, \phi_w\, \hat{\bar{q}}_n \quad \mathrm{d}\Gamma_{\bar{q}_n} + \int_{\Gamma_{\bar{q}_n}} 2\, \phi_{w,t} \left[(m_y - m_x)\, sin(\varphi)\, cos(\varphi) + m_{xy}\, cos(2\,\varphi) \right] \quad \mathrm{d}\Gamma_{\bar{q}_n} \\ = \quad & - \int_{\Gamma_{\bar{q}_n}} \phi_w \left[(m_{y,y} - m_{xy,x})\, sin(\varphi) + (m_{x,x} - m_{xy,y})\, cos(\varphi) \right] \quad \mathrm{d}\Gamma_{\bar{q}_n} + \int_{\Gamma_{\bar{q}_n}} 2\, \phi_w\, \hat{\bar{q}}_n \quad \mathrm{d}\Gamma_{\bar{q}_n} \\ & + \int_{\Gamma_{\bar{q}_n}} 2 \left[- \phi_{w,x}\, sin(\varphi) + \phi_{w,y}\, cos(\varphi) \right] \left[(m_y - m_x)\, sin(\varphi)\, cos(\varphi) + m_{xy}\, cos(2\,\varphi) \right] \quad \mathrm{d}\Gamma_{\bar{q}_n} \end{aligned} \tag{3.13}$$

Applying integration by parts on the line integral over the term including $m_{nt,t}$ gives a sum of point measures at the corners of the domain Ω, which is equal to zero if any of its components is zero. The twisting moment and thus the concentrated force in the corners F_{c} cannot be set, since the tangential component of the unit outward normal n_t is always zero.Transforming the twisting moment m_{nt} in equation 3.12 before integrating by parts leads to an equivalent factor, which is also identically equal to zero for any angle φ. Inserting 3.13 into local equilibrium 3.5 yields the final representation, which is presented in section 3.3.
The Neumann boundary condition within methods 1 and 2 from the list in section 3.2 is enforced by evaluating the boundary terms 3.13 accordingly on the corresponding parts of the boundary $\Gamma_{\bar{q}_n}$. On parts of the boundary, on which the effective shear force is not prescribed, or if the chosen method to set the Neumann boundary conditions is 3, which involves Lagrange multipliers for all boundary

conditions, the initial boundary terms in 3.9 are evaluated.
Line integrals over the boundary, which are not used to enforce boundary conditions, are evaluated and added to the corresponding rows and columns in the stiffness matrix after making an ansatz and discretising the problem, while line integrals including one test function and Neumann boundary data are added to the load vector, as described in section 3.4.3.
For the unknown $\hat{\tilde{q}}_n$ the deflection w of the thin plate is the conjugated quantity, hence the boundary terms vanish for homogenious Dirichlet boundary conditions on the deflection field. If the effective shear force is set using boundary term evaluation, derivatives of the deflection field are also involved. Thus the boundary terms are identically equal to zero on a clamped boundary with homogenious Dirchlet data on w.

3.2.2 Recasting Equations 3.6 and 3.7

Equations 3.6 and 3.7 are rewritten such that Neumann boundary conditions on $w_{,n} = \hat{w}_{,n}$ may be prescribed and only first derivatives of the test functions remain. Integration by parts of the first terms of these equations, which include second derivatives of the deflection, gives:

$$\begin{aligned}
\int_\Omega \phi_{m_x}\, w_{,xx} \quad \mathrm{d}\Omega &= -\int_\Omega \phi_{m_x,x}\, w_{,x} \quad \mathrm{d}\Omega + \int_\Gamma \phi_{m_x}\, w_{,x}\, n_x \quad \mathrm{d}\Gamma \\
\int_\Omega \phi_{m_y}\, w_{,yy} \quad \mathrm{d}\Omega &= -\int_\Omega \phi_{m_y,y}\, w_{,y} \quad \mathrm{d}\Omega + \int_\Gamma \phi_{m_y}\, w_{,y}\, n_y \quad \mathrm{d}\Gamma
\end{aligned} \tag{3.14}$$

Analogous to 3.2.1 the line integrals over the whole boundary of the domain must be evaluated, if the normal derivative of the plates' deflection is not prescribed. To set Neumann boundary data on the slope of the plate via the boundary terms, the boundary terms in 3.14 are recast:

$$w_{,n} = w_{,x}\, cos(\varphi) + w_{,y}\, sin(\varphi) \tag{3.15}$$

$$\Longrightarrow \qquad w_{,n} = \hat{w}_{,n} = w_{,x}\, cos(\varphi) + w_{,y}\, sin(\varphi) \qquad \Longleftrightarrow \begin{cases} w_{,x} = (\hat{w}_{,n} - w_{,y}\, sin(\varphi))\, \frac{1}{cos(\varphi)} \\ w_{,y} = (\hat{w}_{,n} - w_{,x}\, cos(\varphi))\, \frac{1}{sin(\varphi)} \end{cases} \tag{3.16}$$

By inserting into 3.14 Neumann boundary conditions on $w_{,n}$ are enforced:

$$\begin{aligned}
\int_{\Gamma_{w,n}} \phi_{m_x}\, w_{,x}\, n_x \quad \mathrm{d}\Gamma_{w,n} &= \int_{\Gamma_{w,n}} \phi_{m_x}\, \frac{\overbrace{n_x}^{=1}}{cos(\varphi)}\, (\hat{w}_{,n} - w_{,y}\, sin(\varphi)) \quad \mathrm{d}\Gamma_{w,n} \quad = \\
&= \int_{\Gamma_{w,n}} \phi_{m_x}\, \hat{w}_{,n} \quad \mathrm{d}\Gamma_{w,n} - \int_{\Gamma_{w,n}} \phi_{m_x}\, w_{,y}\, sin(\varphi) \quad \mathrm{d}\Gamma_{w,n}
\end{aligned} \tag{3.17}$$

$$\begin{aligned}
\int_{\Gamma_{w,n}} \phi_{m_y}\, w_{,y}\, n_y \quad \mathrm{d}\Gamma_{w,n} &= \int_{\Gamma_{w,n}} \phi_{m_y}\, \frac{\overbrace{n_y}^{=1}}{sin(\varphi)}\, (\hat{w}_{,n} - w_{,x}\, cos(\varphi)) \quad \mathrm{d}\Gamma_{w,n} \quad = \\
&= \int_{\Gamma_{w,n}} \phi_{m_y}\, \hat{w}_{,n} \quad \mathrm{d}\Gamma_{w,n} - \int_{\Gamma_{w,n}} \phi_{m_y}\, w_{,x}\, cos(\varphi) \quad \mathrm{d}\Gamma_{w,n}
\end{aligned} \tag{3.18}$$

Again integrals, which are not used to prescribe boundary conditions, are added to the stiffness matrix after making an ansatz and discretising the boundary value problem, while the other terms are evaluated and added to the right hand side of the linear system of equations.

3.2.3 Recasting Equation 3.8

Integration by parts applied to the terms involving second derivatives in the governing equation on the twisting moment field yields:

$$\begin{aligned}\int_{\Omega} \phi_{m_{xy}}\, 2\, w_{,xy} \quad \mathrm{d}\Omega = &- \int_{\Omega} \phi_{m_{xy},x}\, w_{,y} \quad \mathrm{d}\Omega + \int_{\Gamma} \phi_{m_{xy}}\, w_{,y}\, n_x \quad \mathrm{d}\Gamma \\ &- \int_{\Omega} \phi_{m_{xy},y}\, w_{,x} \quad \mathrm{d}\Omega + \int_{\Gamma} \phi_{m_{xy}}\, w_{,x}\, n_y \quad \mathrm{d}\Gamma \end{aligned} \tag{3.19}$$

The chosen form of the line integral over the whole boundary of the domain is not used to prescribe any boundary data. However it is explicitly highlighted, that the first three field equations may be used to enforce Neumann boundary conditions in $\bar{q}_n$ and $w_{,n}$ respectively, but there is no line integral available and no integral over the domain may be rewritten to prescribe the bending moment normal to an edge of the plate with producing a factor, which is bounded for any angle φ. Thus an alternative approach in prescribing this condition is taken in formulating Lagrange multipliers, which are introduced in the following section.

3.2.4 Lagrange Multipliers

In order to set essential boundary conditions on curved edges in the deflection and the bending moment normal to the edge Lagrange multipliers are introduced. While the deflection w could be prescribed utilising the Kronecker-delta property of the employed Lagrange shape functions, the bending moment normal to the boundary Γ_{m_n} is not a primary variable and hence Dirichlet data cannot be enforced in a straightforward manner.
The Dirichlet boundary condition in terms of the deflection of the plate is converted into integral form using Lagrange multipliers λ_w:

$$w = \hat{w} \quad \Longrightarrow \quad \int_{\Gamma_w} \lambda_w\, (w - \hat{w}) \quad \mathrm{d}\Gamma_w = 0 \quad \Longleftrightarrow \quad \int_{\Gamma_w} \lambda_w\, w \quad \mathrm{d}\Gamma_w = \int_{\Gamma_w} \lambda_w\, \hat{w} \quad \mathrm{d}\Gamma_w \tag{3.20}$$

The Dirichlet boundary condition on the bending moment m_n normal to the boundary Γ_{m_n} is prescribed in a weak manner using Lagrange multipliers λ_{m_n}:

$$\begin{aligned} m_n = \hat{m}_n \quad &\Longrightarrow \quad \int_{\Gamma_{m_n}} \lambda_{m_n}\, (m_n - \hat{m}_n) \quad \mathrm{d}\Gamma_{m_n} = 0 \\ &\Longleftrightarrow \quad \int_{\Gamma_{m_n}} \lambda_{m_n}\, m_n \quad \mathrm{d}\Gamma_{m_n} = \int_{\Gamma_{m_n}} \lambda_{m_n}\, \hat{m}_n \quad \mathrm{d}\Gamma_{m_n} \quad = \\ &= \quad \int_{\Gamma_{m_n}} \lambda_{m_n} \left[m_x\, cos^2(\varphi) + m_y\, sin^2(\varphi) + m_{xy}\, sin(2\,\varphi) \right] \quad \mathrm{d}\Gamma_{m_n} \end{aligned} \tag{3.21}$$

Adding additional constraints on the approximation fields is mandatory if curved boundaries shall be treated within the presented approach.

Natural boundary conditions are also enforced introducing Lagrange multipliers for the respective quantities within method 3. The Neumann boundary condition for the normal derivative of the deflection surface of the plate $w_{,n}$ is prescribed in integral form using the Lagrange multiplier $\lambda_{w,n}$:

$$
\begin{aligned}
w_{,n} = \hat{w}_{,n} \quad &\Longrightarrow \quad \int\limits_{\Gamma_{w,n}} \lambda_{w,n}\,(w_{,n} - \hat{w}_{,n}) \quad \mathrm{d}\Gamma_{w,n} = 0 \\
&\Longleftrightarrow \quad \int\limits_{\Gamma_{w,n}} \lambda_{w,n}\, w_{,n} \quad \mathrm{d}\Gamma_{w,n} = \int\limits_{\Gamma_{w,n}} \lambda_{w,n}\, \hat{w}_{,n} \quad \mathrm{d}\Gamma_{w,n} \quad = \\
&= \int\limits_{\Gamma_{w,n}} \lambda_{w,n} \Big[w_{,x}\, cos(\varphi) + w_{,y}\, sin(\varphi) \Big] \quad \mathrm{d}\Gamma_{w,n}
\end{aligned} \tag{3.22}
$$

Analogously the Neumann boundary condition for the effective shear force $\bar{q}_n$ normal to the partition of the boundary $\Gamma_{\bar{q}_n}$ may be fulfilled in a weak sense by introducing a Lagrange multiplier $\lambda_{\bar{q}_n}$ to convert the natural boundary condition into the following integral form:

$$
\begin{aligned}
\bar{q}_n = \hat{\bar{q}}_n \;\Longrightarrow \quad & \int\limits_{\Gamma_{\bar{q}_n}} \lambda_{\bar{q}_n}\,(\bar{q}_n - \hat{\bar{q}}_n) \quad \mathrm{d}\Gamma_{\bar{q}_n} = 0 \\
\Longleftrightarrow \quad & \int\limits_{\Gamma_{\bar{q}_n}} \lambda_{\bar{q}_n}\, \bar{q}_n \quad \mathrm{d}\Gamma_{\bar{q}_n} = \int\limits_{\Gamma_{\bar{q}_n}} \lambda_{\bar{q}_n}\, \hat{\bar{q}}_n \quad \mathrm{d}\Gamma_{\bar{q}_n} \quad = \\
= & \int\limits_{\Gamma_{\bar{q}_n}} \lambda_{\bar{q}_n} \Big[q_n + m_{nt,t} \Big] \quad \mathrm{d}\Gamma_{\bar{q}_n} = \int\limits_{\Gamma_{\bar{q}_n}} \lambda_{\bar{q}_n} \Big[q_x\, cos(\varphi) + q_y\, sin(\varphi) \\
& + \frac{\partial}{\partial t}\Big((m_y - m_x)\, sin(\varphi)\, cos(\varphi) + m_{xy}\, cos(2\,\varphi) \Big) \Big] \quad \mathrm{d}\Gamma_{\bar{q}_n} \quad = \\
= & \int\limits_{\Gamma_{\bar{q}_n}} \lambda_{\bar{q}_n} \Big[\overbrace{(m_{x,x} + m_{xy,y})}^{=q_x}\, cos(\varphi) + \overbrace{(m_{y,y} + m_{xy,x})}^{=q_y}\, sin(\varphi) \\
& + \Big(\big(\overbrace{(-m_{y,x}\, sin(\varphi) + m_{y,y}\, cos(\varphi))}^{=m_{y,t}} - \overbrace{(-m_{x,x}\, sin(\varphi) + m_{x,y}\, cos(\varphi))}^{=m_{x,t}} \big) \\
& sin(\varphi)\, cos(\varphi) + \overbrace{(-m_{xy,x}\, sin(\varphi) + m_{xy,y}\, cos(\varphi))}^{=m_{xy,t}}\, cos(2\,\varphi) \Big) \Big] \quad \mathrm{d}\Gamma_{\bar{q}_n}
\end{aligned} \tag{3.23}
$$

Where the derivative in tangential direction is rewritten using equation 2.21. With the Lagrange multipliers introduced it is possible to enforce all Neumann and Dirichlet boundary conditions described in section 2.6, namely clamped, pinned, free or symmetry boundary conditions on polygonal domains with curved boundries.
To apply a Finite Element Method the weak form of the system of partial differential equations is derived in the following sections.

3.3 Continuous Weak Form

Before introducing the continuous weak form the function space of square integrable functions $\mathrm{L}_2(\Omega)$ and the Sobolev space of square integrable functions with square integrable derivatives are defined [5, 10]:

$$\mathrm{L}^2(\Omega) := \left\{ \phi \,\middle|\, \int_\Omega [\phi]^2 \, \mathrm{d}\Omega = ||\phi||^2_{\mathrm{L}^2(\Omega)} < +\infty \right\} \tag{3.24}$$

$$\mathrm{H}^1(\Omega) := \left\{ \phi \in \mathrm{L}^2(\Omega), \phi_{,x} \in \mathrm{L}^2(\Omega), \phi_{,y} \in \mathrm{L}^2(\Omega) \right\} \tag{3.25}$$

If $\Gamma = \partial\Omega$ is smooth enough (for instance Lipschitzian), the trace $\gamma\phi = \phi|_\Gamma$ of $\phi \in \mathrm{H}^1(\Omega)$ on the boundary Γ may be defined. The traces of functions in $\mathrm{H}^1(\Omega)$ span a Hilbert space, denoted $\mathrm{H}^{1/2}(\Omega)$, that is a proper dense subspace of $\mathrm{L}^2(\Omega)$ with the dual space denoted as $\mathrm{H}^{-1/2}(\Omega)$ [5, p. 48].
For the complementary parts of the partitions $\Gamma_\diamond$ of the boundary of the domain $\partial\Omega$ an additional notation is introduced:

$$\Gamma^{\mathrm{c}}_\diamond := \{ \boldsymbol{x} \in \partial\Omega \setminus \Gamma_\diamond \} \qquad \text{with} \quad \diamond = w, w_{,n}, m_n, \bar{q}_n \tag{3.26}$$

The test functions ϕ_w, ϕ_{m_x}, ϕ_{m_y} and $\phi_{m_{xy}}$ are chosen from the Sobolev space of square integrable functions $\mathrm{H}^1(\Omega)$, whose first derivatives are also square integrable. Also for both continuous weak forms 3.27 and 3.28 the space of test functions corresponding to the Lagrange multipliers is $\mathrm{H}^{-1/2}(\Gamma)$ (compare [8]).
The choice of spaces is crucial for the quality of the approximation, in fact the spaces of test functions in the weak mixed formulation presented must meet the Babuška-Brezzi condition, i.e. an inf-sup condition. The weak formulations induce a saddle point problem for which existence and uniqueness must be proven, which will not be covered within this thesis.
Herein, the fulfilment of the inf-sup criterion is shown numerically by completion of convergence studies. For the mathematical analysis of this problem the reader is referred to *Babuška* [3], *Boffi et. al.* [5], *Brezzi* [6], *Ciarlet et al.* [7] and the references therein.

3.3.1 Continuous Weak Form - Methods 1 & 2

The continuous weak form of the multi-field boundary value problem of the Kirchhoff-Love plate including Lagrange multipliers for the Dirichlet boundary conditions on the deflection w and the bending moment normal to the boundary m_n is:

$$
\left\{
\begin{aligned}
&\text{find } \phi_w,\, \phi_{m_x},\, \phi_{m_y},\, \phi_{m_{xy}} \in \mathrm{H}^1(\Omega) \\
&\text{and } \mu_w \in \mathrm{H}^{-1/2}(\Gamma_w),\, \mu_{m_n} \in \mathrm{H}^{-1/2}(\Gamma_{m_n}) \text{ such that} \\
&\qquad - \int_\Omega \phi_{w,x}\, m_{x,x} + \phi_{w,y}\, m_{y,y} + \phi_{w,x}\, m_{xy,y} + \phi_{w,y}\, m_{xy,x}\, \mathrm{d}\Omega \\
&\qquad - \int_{\Gamma_{\bar{q}_n}} \phi_w \left[(m_{y,y} - m_{xy,x})\, n_y + (m_{x,x} - m_{xy,y})\, n_x \right] \mathrm{d}\Gamma_{\bar{q}_n} \\
&\quad + \int_{\Gamma_{\bar{q}_n}} 2 \left[-\phi_{w,x}\, n_y + \phi_{w,y}\, n_x \right] \left[(m_y - m_x)\, n_y\, n_x + m_{xy}\, (n_x^2 - n_y^2) \right] \mathrm{d}\Gamma_{\bar{q}_n} \\
&+ \int_{\Gamma^{\mathrm{c}}_{\bar{q}_n}} \phi_w \left[(m_{x,x} + m_{xy,y})\, n_x + (m_{y,y} + m_{xy,x})\, n_y \right] \mathrm{d}\Gamma^{\mathrm{c}}_{\bar{q}_n} + \int_{\Gamma_w} \phi_w\, \lambda_w\, \mathrm{d}\Gamma_w \quad = \\
&\qquad = \quad - \int_\Omega \phi_w\, p\, \mathrm{d}\Omega - \int_{\Gamma_{\bar{q}_n}} 2\, \phi_w\, \hat{\bar{q}}_n\, \mathrm{d}\Gamma_{\bar{q}_n} \\
&\qquad\qquad\qquad\qquad\qquad\qquad \forall \phi_w \in \mathrm{H}^1(\Omega)\,, \\
&\qquad - \int_\Omega \phi_{m_x,x}\, w_{,x}\, \mathrm{d}\Omega - \int_{\Gamma_{w,n}} \phi_{m_x}\, w_{,y}\, n_y\, \mathrm{d}\Gamma_{w,n} + \int_{\Gamma^{\mathrm{c}}_{w,n}} \phi_{m_x}\, w_{,x}\, n_x\, \mathrm{d}\Gamma^{\mathrm{c}}_{w,n} \\
&\quad + \int_{\Gamma_{m_n}} \phi_{m_x}\, \lambda_{m_n}\, n_x^2\, \mathrm{d}\Gamma_{m_n} + \int_\Omega \phi_{m_x}\, \tfrac{m_x - \nu\, m_y}{K\,(1-\nu^2)}\, \mathrm{d}\Omega = - \int_{\Gamma_{w,n}} \phi_{m_x}\, \hat{w}_{,n}\, \mathrm{d}\Gamma_{w,n} \\
&\qquad\qquad\qquad\qquad\qquad\qquad \forall \phi_{m_x} \in \mathrm{H}^1(\Omega)\,, \\
&\qquad - \int_\Omega \phi_{m_y,y}\, w_{,y}\, \mathrm{d}\Omega - \int_{\Gamma_{w,n}} \phi_{m_y}\, w_{,x}\, n_x\, \mathrm{d}\Gamma_{w,n} + \int_{\Gamma^{\mathrm{c}}_{w,n}} \phi_{m_y}\, w_{,y}\, n_y\, \mathrm{d}\Gamma^{\mathrm{c}}_{w,n} \\
&\quad + \int_{\Gamma_{m_n}} \phi_{m_y}\, \lambda_{m_n}\, n_y^2\, \mathrm{d}\Gamma_{m_n} + \int_\Omega \phi_{m_y}\, \tfrac{m_y - \nu\, m_x}{K\,(1-\nu^2)}\, \mathrm{d}\Omega = - \int_{\Gamma_{w,n}} \phi_{m_y}\, \hat{w}_{,n}\, \mathrm{d}\Gamma_{w,n} \\
&\qquad\qquad\qquad\qquad\qquad\qquad \forall \phi_{m_y} \in \mathrm{H}^1(\Omega)\,, \\
&\qquad - \int_\Omega \phi_{m_{xy},x}\, w_{,y} + \phi_{m_{xy},y}\, w_{,x}\, \mathrm{d}\Omega + \int_\Gamma \phi_{m_{xy}}\, (w_{,x}\, n_y + w_{,y}\, n_x)\, \mathrm{d}\Gamma \\
&\quad + \int_\Omega \phi_{m_{xy}}\, \tfrac{2\,(1+\nu)}{K\,(1-\nu^2)}\, m_{xy}\, \mathrm{d}\Omega + \int_{\Gamma_{m_n}} 2\, \phi_{m_{xy}}\, \lambda_{m_n}\, n_x\, n_y\, \mathrm{d}\Gamma_{m_n} = 0 \\
&\qquad\qquad\qquad\qquad\qquad\qquad \forall \phi_{m_{xy}} \in \mathrm{H}^1(\Omega)\,, \\
&\qquad\qquad \int_{\Gamma_w} \mu_w\, w\, \mathrm{d}\Gamma_w = \int_{\Gamma_w} \mu_w\, \hat{w}\, \mathrm{d}\Gamma_w \\
&\qquad\qquad\qquad\qquad\qquad\qquad \forall \mu_w \in \mathrm{H}^{-1/2}(\Gamma_w)\,, \\
&\qquad\qquad \int_{\Gamma_{m_n}} \mu_{m_n} \left(m_x\, n_x^2 + m_y\, n_y^2 + 2\, m_{xy}\, n_x\, n_y \right) \mathrm{d}\Gamma_{m_n} \quad = \\
&\qquad\qquad\qquad = \quad \int_{\Gamma_{m_n}} \mu_{m_n}\, \hat{m}_n\, \mathrm{d}\Gamma_{m_n} \\
&\qquad\qquad\qquad\qquad\qquad\qquad \forall \mu_{m_n} \in \mathrm{H}^{-1/2}(\Gamma_{m_n})\,.
\end{aligned}
\right. \tag{3.27}
$$

3.3.2 Continuous Weak Form - Method 3

The continuous weak form of the multi-field boundary value problem of the Kirchhoff-Love plate including Lagrange multipliers λ_w, λ_{m_n} and, contrary to the foregoing methods, also $\lambda_{w,n}$ and $\lambda_{\bar{q}_n}$ to enforce both Dirichlet and Neumann boundary conditions is:

$$
\left\{
\begin{aligned}
&\text{find } \phi_w,\, \phi_{m_x},\, \phi_{m_y},\, \phi_{m_{xy}} \in \mathrm{H}^1(\Omega) \text{ and } \mu_w \in \mathrm{H}^{-1/2}(\Gamma_w),\, \mu_{m_n} \in \mathrm{H}^{-1/2}(\Gamma_{m_n}),\\
&\mu_{w,n} \in \mathrm{H}^{-1/2}(\Gamma_{w,n}),\, \mu_{\bar{q}_n} \in \mathrm{H}^{-1/2}(\Gamma_{\bar{q}_n}) \text{ such that}\\
&\qquad -\int_\Omega \phi_{w,x}\, m_{x,x} + \phi_{w,y}\, m_{y,y} + \phi_{w,x}\, m_{xy,y} + \phi_{w,y}\, m_{xy,x}\, \mathrm{d}\Omega\\
&\quad + \int_\Gamma \phi_w \left[(m_{x,x} + m_{xy,y})\, n_x + (m_{y,y} + m_{xy,x})\, n_y \right] \mathrm{d}\Gamma + \int_{\Gamma_w} \phi_w\, \lambda_w \mathrm{d}\Gamma_w\\
&\qquad + \int_{\Gamma_{w,n}} (\phi_{w,x}\, n_x + \phi_{w,y}\, n_y)\, \lambda_{w,n} \mathrm{d}\Gamma_{w,n} = -\int_\Omega \phi_w\, p\, \mathrm{d}\Omega\\
&\qquad\qquad \forall \phi_w \in \mathrm{H}^1(\Omega)\,,\\
&\qquad -\int_\Omega \phi_{m_x,x}\, w_{,x}\, \mathrm{d}\Omega + \int_\Gamma \phi_{m_x}\, w_{,x}\, n_x\, \mathrm{d}\Gamma + \int_{\Gamma_{m_n}} \phi_{m_x}\, \lambda_{m_n}\, n_x^2\, \mathrm{d}\Gamma_{m_n}\\
&+ \int_{\Gamma_{\bar{q}_n}} \left(\phi_{m_x,x}\, (n_x + n_x\, n_y^2) - \phi_{m_x,y}\, (n_x^2\, n_y) \right) \lambda_{\bar{q}_n}\, \mathrm{d}\Gamma_{\bar{q}_n} + \int_\Omega \phi_{m_x}\, \tfrac{m_x - \nu\, m_y}{K\,(1-\nu^2)}\, \mathrm{d}\Omega = 0\\
&\qquad\qquad \forall \phi_{m_x} \in \mathrm{H}^1(\Omega)\,,\\
&\qquad -\int_\Omega \phi_{m_y,y}\, w_{,y}\, \mathrm{d}\Omega + \int_\Gamma \phi_{m_y}\, w_{,y}\, n_y\, \mathrm{d}\Gamma + \int_{\Gamma_{m_n}} \phi_{m_y}\, \lambda_{m_n}\, n_y^2\, \mathrm{d}\Gamma_{m_n}\\
&+ \int_{\Gamma_{\bar{q}_n}} \left(\phi_{m_y,y}\, (n_y + n_x^2\, n_y) - \phi_{m_y,x}\, (n_x\, n_y^2) \right) \lambda_{\bar{q}_n}\, \mathrm{d}\Gamma_{\bar{q}_n} + \int_\Omega \phi_{m_y}\, \tfrac{m_y - \nu\, m_x}{K\,(1-\nu^2)}\, \mathrm{d}\Omega = 0\\
&\qquad\qquad \forall \phi_{m_y} \in \mathrm{H}^1(\Omega)\,,\\
&\qquad -\int_\Omega \phi_{m_{xy},x}\, w_{,y} + \phi_{m_{xy},y}\, w_{,x}\, \mathrm{d}\Omega + \int_\Gamma \phi_{m_{xy}}\, (w_{,x}\, n_y + w_{,y}\, n_x)\, \mathrm{d}\Gamma\\
&\qquad + \int_\Omega \phi_{m_{xy}}\, \tfrac{2\,(1+\nu)}{K\,(1-\nu^2)}\, m_{xy}\, \mathrm{d}\Omega + \int_{\Gamma_{m_n}} 2\, \phi_{m_{xy}}\, \lambda_{m_n}\, n_x\, n_y\, \mathrm{d}\Gamma_{m_n}\\
&\int_{\Gamma_{\bar{q}_n}} \left(\phi_{m_{xy},x}\, n_y\, (1 - n_x^2 + n_y^2) + \phi_{m_{xy},y}\, n_x\, (1 + n_x^2 - n_y^2) \right) \lambda_{\bar{q}_n}\, \mathrm{d}\Gamma_{\bar{q}_n} = 0\\
&\qquad\qquad \forall \phi_{m_{xy}} \in \mathrm{H}^1(\Omega)\,,\\
&\qquad\qquad \int_{\Gamma_w} \mu_w\, w\, \mathrm{d}\Gamma_w = \int_{\Gamma_w} \mu_w\, \hat{w}\, \mathrm{d}\Gamma_w\\
&\qquad\qquad\qquad \forall \mu_w \in \mathrm{H}^{-1/2}(\Gamma_w)\,,\\
&\int_{\Gamma_{m_n}} \mu_{m_n} \left(m_x\, n_x^2 + m_y^2\, n_y + 2\, m_{xy}\, n_x\, n_y \right) \mathrm{d}\Gamma_{m_n} = \int_{\Gamma_{m_n}} \mu_{m_n}\, \hat{m}_n\, \mathrm{d}\Gamma_{m_n}\\
&\qquad\qquad\qquad \forall \mu_{m_n} \in \mathrm{H}^{-1/2}(\Gamma_{m_n})\,,\\
&\qquad\qquad \int_{\Gamma_{w,n}} \mu_{w,n}\, (w_{,x}\, n_x + w_{,y}\, n_y)\, \mathrm{d}\Gamma_{w,n} = \int_{\Gamma_{m_n}} \mu_{w,n}\, \hat{w}_{,n}\, \mathrm{d}\Gamma_{w,n}\\
&\qquad\qquad\qquad \forall \mu_{w,n} \in \mathrm{H}^{-1/2}(\Gamma_{w,n})\,,\\
&\int_{\Gamma_{\bar{q}_n}} \mu_{\bar{q}_n} \Big(m_{x,x}\, n_x\, (1 + n_y^2) - m_{x,y}\, n_x^2\, n_y + m_{y,y}\, n_y\, (1 + n_x^2) - m_{y,x}\, n_y^2\, n_x\\
&\qquad + m_{xy,x}\, n_y\, (1 - n_x^2 + n_y^2) + m_{xy,y}\, n_x\, (1 + n_x^2 - n_y^2) \Big)\, \mathrm{d}\Gamma_{\bar{q}_n} \quad =\\
&\qquad\qquad = \int_{\Gamma_{\bar{q}_n}} \mu_{\bar{q}_n}\, \hat{\bar{q}}_n\, \mathrm{d}\Gamma_{\bar{q}_n}\\
&\qquad\qquad\qquad \forall \mu_{\bar{q}_n} \in \mathrm{H}^{-1/2}(\Gamma_{\bar{q}_n})\,.
\end{aligned}
\right. \tag{3.28}
$$

3.4 Discrete Weak Form

Adopting the isoparametric concept to approximate the given domain Ω an ansatz is made. The number of globally continuous nodal based functions of the decomposition of the domain is therein denoted with n, the number of nodes on the boundary with m. The nodal values of the fields are marked by a right subscript corresponding to the shape function, whose function value is equal to 1 in the same node, the tilde above indicates the approximation:

$$
\begin{aligned}
w(\boldsymbol{x}) \approx \tilde{w}(\boldsymbol{x}) = \sum_{i=1}^{n} w_i \, N_i(\boldsymbol{x}) \qquad & m_x(\boldsymbol{x}) \approx \tilde{m}_x(\boldsymbol{x}) = \sum_{i=1}^{n} m_{x\,i} \, N_i(\boldsymbol{x}) \\
m_y(\boldsymbol{x}) \approx \tilde{m}_y(\boldsymbol{x}) = \sum_{i=1}^{n} m_{y\,i} \, N_i(\boldsymbol{x}) \qquad & m_{xy}(\boldsymbol{x}) \approx \tilde{m}_{xy}(\boldsymbol{x}) = \sum_{i=1}^{n} m_{xy\,i} \, N_i(\boldsymbol{x}) \\
\lambda_{\triangleright}(\boldsymbol{x}_{\Gamma_{\triangleright}}) \approx \tilde{\lambda}_{\triangleright}(\boldsymbol{x}_{\Gamma_{\triangleright}}) = \sum_{i=1}^{m} \lambda_{\triangleright\,i} \, M_i(\boldsymbol{x}_{\Gamma_{\triangleright}}) \qquad & \lambda_{\bowtie}(\boldsymbol{x}_{\Gamma_{\bowtie}}) \approx \tilde{\lambda}_{\bowtie}(\boldsymbol{x}_{\Gamma_{\bowtie}}) = \sum_{i=1}^{m} \lambda_{\bowtie\,i} \, M_i^d(\boldsymbol{x}_{\Gamma_{\bowtie}}) \\
\text{with:} \quad \boldsymbol{x} \in \Omega, \; \boldsymbol{x}_{\Gamma_{\triangleright}} \in \Gamma_{\triangleright}, \; \boldsymbol{x}_{\Gamma_{\bowtie}} \in \Gamma_{\bowtie}, \; \triangleright = w, m_n, \; \bowtie = w_{,n}, \bar{q}_n & \qquad (3.29)
\end{aligned}
$$

Following a Ritz-Galerkin approach, the discretisation of the trial functions is the same as for the corresponding field quantities and is labeled analogously with a tilde. The element local shape functions for the nodal based trial functions N_i are built from Lagrange polynomials.
The trial functions M_i are either also composed by 1-dimensional Lagrange Polynomials defined by nodes on the boundary or by Dirac-delta functions δ. The latter choice is referred to as the Point Collocation Method [8]. Within this approach the nodal value λ_i in a point $\boldsymbol{x}_{\Gamma\,i}$ on the boundary Γ_i is prescribed in a straightforward manner.
The shape functions M_i and M_i^d to approximate the trial spaces are chosen differently for the methods formulated within this thesis as presented in the following list:

Methods used to apply Boundary Conditions

1. Choose $M_i(\boldsymbol{x}) = \delta(\boldsymbol{x} - \boldsymbol{x}_{\Gamma\,i})$ and prescribe all Dirichlet boundary conditions (Point Collocation Method). Natural boundary conditions enter the system via boundary terms, the unit outward normal in corners is weighted by the element areas of the coinciding elements.

2. Enforce Dirichlet boundary conditions using $M_i(\boldsymbol{x}) = \Phi(\mathrm{P}_p)_i(\boldsymbol{x})$ with $\Phi(\mathrm{P}_p)_i$ being an image of a Lagrange polynomial of order $k \leq p$ defined in a reference element. The points defining the $M_i(\boldsymbol{x})$ are edge nodes of the neighbouring two dimensional Lagrange elements. Neumann boundary conditions are applied via evaluation of boundary terms.

3. Enforce Dirichlet boundary conditions using $M_i(\boldsymbol{x}) = \Phi(\mathrm{P}_p)_i(\boldsymbol{x})$ and natural boundary conditions via $M_i^d(\boldsymbol{x}) = \Phi(\mathrm{P}_{p-1})_i(\boldsymbol{x})$.

It is explicitly highlighted, that for the discretisation of the Lagrange multiplier spaces corresponding to the slope normal to an edge $w_{,n}$ and the effective shear force $\bar{q}_n$ Lagrange polynomials are used, which are one order lower than the ones used for the Lagrange multipliers corresponding to the deflection w or the bending moment m_n.
The geometry description for $M_i(\boldsymbol{x})$ is of the same order as the ansatz, i.e. isoparametric, using the nodes of a neighbouring two dimensional element. The ansatz for $M_i^d(\boldsymbol{x})$ is one order lower, leading to a superparametric mapping [4].
This choice was made since an isoparametric approach for all trial spaces led to a singular system of equations for the third method of applying boundary conditions. This is an immediate consequence of not fulfilling the Babuška-Brezzi stability criterion. The enforcement of boundary conditions via Lagrange multipliers on the one hand must not be too strict, but on the other hand allow for a proper

approximation [6, 3]. For the third method of applying boundary conditions the presented choice led to satisfactory results, which will be presented in chapter 4.
Considering the transformation equations introduced in section 2.5 the problem of choosing an angle φ within method 1 is imminent. For arbitrary corner angles only one Lagrange multiplier may be defined in the corner prescribing any of the described Dirichlet boundary conditions, since the resulting linear system of equations becomes singular, if the edge is in fact not an edge but a corner node of two or more coinciding elements along a boundary forming a straight line. The unit outward normal and thus the angle φ is therefore weighted by the areas of the elements with edges coinciding in the collocation point and only one condition for one multiplier is set in the node. This approach leads in general to an error, because the geometry description of the boundary is not C^1 continuous. For the methods 2 and 3 the choice of φ is trivial, since the integration points using Gauss quadrature are not located at the corners of the boundary.
To present the discrete weak form of the mixed boundary value problem the finite element trial spaces $\mathrm{D}(\Gamma)$ and $\mathrm{H}^s_{h,p}(\Xi)$ with $\Xi \subset \mathbb{R}^2$ are introduced [5, 8]:

$$\begin{aligned} \mathrm{H}^{-1/2} \supset \mathrm{D}(\Gamma) &:= \operatorname{span}\Big\{\delta(\boldsymbol{x} - \boldsymbol{x}_{\Gamma\, i})\Big\}_{i=1}^{m} \\ \mathrm{H}^{s} \supset \mathrm{H}^s_{h,p}(\Xi) &:= \operatorname{span}\Big\{M_i | M_i \in \mathrm{H}^s(\Xi),\, M_i \in \Phi(\mathrm{P}_p)\Big\}_{i=1}^{m} \end{aligned} \tag{3.30}$$

with m ... number of nodes in Ξ,

$\Phi(\mathrm{P}_p)$ ... image of a Lagrange polynomial of order $k \leq p$.

The continuous weak form is recast with the ansatz 3.29 using the test functions N_i, M_i and M_i^d chosen from the finite dimensional trial spaces 3.30. This results in the discrete weak forms of the multi-field boundary value problem 3.31 and 3.32, which are equivalent to linear systems of equations.

3.4.1 Discrete Weak Form - Methods 1 & 2

The discrete weak form of the mixed formulation of the boundary value problem considered, using methods 1 or 2 described in 3.2 to prescribe boundary conditions is:

$$
\left\{
\begin{array}{l}
\text{find } \tilde{\phi}_w,\, \tilde{\phi}_{m_x},\, \tilde{\phi}_{m_y},\, \tilde{\phi}_{m_{xy}} \in \mathrm{H}^1_{h,p}(\Omega), \\
\text{and } \tilde{\mu}_w \in \mathrm{D}(\Gamma_w)\,, \tilde{\mu}_{m_n} \in \mathrm{D}(\Gamma_{m_n}) \text{ (method 1)}, \\
\text{or } \tilde{\mu}_w \in \mathrm{H}^{-1/2}_{h,p}(\Gamma_w)\,, \tilde{\mu}_{m_n} \in \mathrm{H}^{-1/2}_{h,p}(\Gamma_{m_n}) \text{ (method 2) such that} \\
\\
\quad -\int\limits_{\Omega} \tilde{\phi}_{w,y}\, \tilde{m}_{x,x} + \tilde{\phi}_{w,y}\, \tilde{m}_{y,y} + \tilde{\phi}_{w,x}\, \tilde{m}_{xy,y} + \tilde{\phi}_{w,y}\, \tilde{m}_{xy,x}\ \mathrm{d}\Omega \\
\quad -\int\limits_{\Gamma_{\bar{q}n}} \tilde{\phi}_w \left[(\tilde{m}_{y,y} - \tilde{m}_{xy,x})\, n_y + (\tilde{m}_{x,x} - \tilde{m}_{xy,y})\, n_x \right] \mathrm{d}\Gamma_{\bar{q}n} \\
+\int\limits_{\Gamma_{\bar{q}n}} 2 \left[-\tilde{\phi}_{w,x}\, n_y + \tilde{\phi}_{w,y}\, n_x \right] \left[(\tilde{m}_y - \tilde{m}_x)\, n_y\, n_x + \tilde{m}_{xy}\, (n_x^2 - n_y^2) \right] \mathrm{d}\Gamma_{\bar{q}n} \\
+\int\limits_{\Gamma^{\mathrm{c}}_{\bar{q}n}} \tilde{\phi}_w \left[(\tilde{m}_{x,x} + \tilde{m}_{xy,y})\ n_x + (\tilde{m}_{y,y} + \tilde{m}_{xy,y})\ n_y \right] \mathrm{d}\Gamma^{\mathrm{c}}_{\bar{q}n} + \int\limits_{\Gamma_w} \tilde{\phi}_w\, \tilde{\lambda}_w \mathrm{d}\Gamma_w \quad = \\
\quad = \quad -\int\limits_{\Omega} \tilde{\phi}_w\, p\ \mathrm{d}\Omega - \int\limits_{\Gamma_{\bar{q}n}} 2\, \tilde{\phi}_w\, \hat{\tilde{q}}_n\ \mathrm{d}\Gamma_{\bar{q}n} \\
\qquad\qquad \forall \tilde{\phi}_w \in \mathrm{H}^1_{h,p}(\Omega)\,, \\
\\
\quad -\int\limits_{\Omega} \tilde{\phi}_{m_x,x}\, \tilde{w}_{,x}\ \mathrm{d}\Omega - \int\limits_{\Gamma_{w,n}} \tilde{\phi}_{m_x}\, \tilde{w}_{,y}\, n_y\ \mathrm{d}\Gamma_{w,n} + \int\limits_{\Gamma^{\mathrm{c}}_{w,n}} \tilde{\phi}_{m_x}\, \tilde{w}_{,x}\, n_x\ \mathrm{d}\Gamma^{\mathrm{c}}_{w,n} \\
+\int\limits_{\Gamma_{m_n}} \tilde{\phi}_{m_x}\, \tilde{\lambda}_{m_n}\, n_x^2\ \mathrm{d}\Gamma_{m_n} + \int\limits_{\Omega} \tilde{\phi}_{m_x}\, \frac{\tilde{m}_x - \nu\, \tilde{m}_y}{K\,(1-\nu^2)}\ \mathrm{d}\Omega = -\int\limits_{\Gamma_{w,n}} \tilde{\phi}_{m_x}\, \hat{w}_{,n}\ \mathrm{d}\Gamma_{w,n} \\
\qquad\qquad \forall \tilde{\phi}_{m_x} \in \mathrm{H}^1_{h,p}(\Omega)\,, \\
\\
\quad -\int\limits_{\Omega} \tilde{\phi}_{m_y,y}\, \tilde{w}_{,y}\ \mathrm{d}\Omega - \int\limits_{\Gamma_{w,n}} \tilde{\phi}_{m_y}\, \tilde{w}_{,x}\, n_x\ \mathrm{d}\Gamma_{w,n} + \int\limits_{\Gamma^{\mathrm{c}}_{w,n}} \tilde{\phi}_{m_y}\, \tilde{w}_{,y}\, n_y\ \mathrm{d}\Gamma^{\mathrm{c}}_{w,n} \\
+\int\limits_{\Gamma_{m_n}} \tilde{\phi}_{m_y}\, \tilde{\lambda}_{m_n}\, n_y^2\ \mathrm{d}\Gamma_{m_n} + \int\limits_{\Omega} \tilde{\phi}_{m_y}\, \frac{\tilde{m}_y - \nu\, \tilde{m}_x}{K\,(1-\nu^2)}\ \mathrm{d}\Omega = -\int\limits_{\Gamma_{w,n}} \tilde{\phi}_{m_y}\, \hat{w}_{,n}\ \mathrm{d}\Gamma_{w,n} \\
\qquad\qquad \forall \tilde{\phi}_{m_y} \in \mathrm{H}^1_{h,p}(\Omega)\,, \\
\\
\quad -\int\limits_{\Omega} \tilde{\phi}_{m_{xy},x}\, \tilde{w}_{,y} + \tilde{\phi}_{m_{xy},y}\, \tilde{w}_{,x}\ \mathrm{d}\Omega + \int\limits_{\Gamma} \tilde{\phi}_{m_{xy}}\, (\tilde{w}_{,x}\, n_y + \tilde{w}_{,y}\, n_x)\ \mathrm{d}\Gamma \\
+\int\limits_{\Omega} \tilde{\phi}_{m_{xy}}\, \frac{2\,(1+\nu)}{K\,(1-\nu^2)}\, \tilde{m}_{xy}\ \mathrm{d}\Omega + \int\limits_{\Gamma_{m_n}} 2\, \tilde{\phi}_{m_{xy}}\, \tilde{\lambda}_{m_n}\, n_x\, n_y\ \mathrm{d}\Gamma_{m_n} = 0 \\
\qquad\qquad \forall \tilde{\phi}_{m_{xy}} \in \mathrm{H}^1_{h,p}(\Omega)\,, \\
\\
\qquad \int\limits_{\Gamma_w} \tilde{\mu}_w\, \tilde{w}\ \mathrm{d}\Gamma_w = \int\limits_{\Gamma_w} \tilde{\mu}_w\, \hat{w}\ \mathrm{d}\Gamma_w \\
\qquad\qquad \forall \tilde{\mu}_w \in \mathrm{D}(\Gamma_w) \text{ - method 1}\,, \\
\qquad\qquad \forall \tilde{\mu}_w \in \mathrm{H}^{-1/2}_{h,p}(\Gamma_w) \text{ - method 2}\,, \\
\\
\quad \int\limits_{\Gamma_{m_n}} \tilde{\mu}_{m_n} \left(\tilde{m}_x\, n_x^2 + \tilde{m}_y\, n_y^2 + 2\, \tilde{m}_{xy}\, n_x\, n_y \right) \mathrm{d}\Gamma_{m_n} \quad = \\
\quad = \quad \int\limits_{\Gamma_{m_n}} \tilde{\mu}_{m_n}\, \hat{m}_n\ \mathrm{d}\Gamma_{m_n} \\
\qquad\qquad \forall \tilde{\mu}_{m_n} \in \mathrm{D}(\Gamma_{m_n}) \text{ - method 1}\,, \\
\qquad\qquad \forall \tilde{\mu}_{m_n} \in \mathrm{H}^{-1/2}_{h,p}(\Gamma_{m_n}) \text{ - method 2}\,.
\end{array}
\right. \tag{3.31}
$$

3.4.2 Discrete Weak Form - Method 3

The discrete weak form of the mixed formulation of the boundary value problem considered, using method 3 described in 3.2 to prescribe boundary conditions is:

$$
\left\{
\begin{array}{l}
\text{find } \tilde{\phi}_w,\, \tilde{\phi}_{m_x},\, \tilde{\phi}_{m_y},\, \tilde{\phi}_{m_{xy}} \in \mathrm{H}^1_{h,p}(\Omega), \\
\tilde{\mu}_w \in \mathrm{H}^{-1/2}_{h,p}(\Gamma_w),\, \tilde{\mu}_{m_n} \in \mathrm{H}^{-1/2}_{h,p}(\Gamma_{m_n}), \\
\text{and } \tilde{\mu}_{w,n} \in \mathrm{H}^{-1/2}_{h,p-1}(\Gamma_w),\, \tilde{\mu}_{\bar{q}_n} \in \mathrm{H}^{-1/2}_{h,p-1}(\Gamma_{m_n}) \text{ such that} \\
\\
\quad -\int\limits_{\Omega} \tilde{\phi}_{w,x}\, \tilde{m}_{x,x} + \tilde{\phi}_{w,y}\, \tilde{m}_{y,y} + \tilde{\phi}_{w,x}\, \tilde{m}_{xy,y} + \tilde{\phi}_{w,y}\, \tilde{m}_{xy,x}\ \mathrm{d}\Omega \\
\quad +\int\limits_{\Gamma} \tilde{\phi}_w \left[(\tilde{m}_{x,x} + \tilde{m}_{xy,y})\ n_x + (\tilde{m}_{y,y} + \tilde{m}_{xy,x})\ n_y \right] \mathrm{d}\Gamma + \int\limits_{\Gamma_w} \tilde{\phi}_w\, \tilde{\lambda}_w \mathrm{d}\Gamma_w \\
\quad +\int\limits_{\Gamma_{w,n}} \left(\tilde{\phi}_{w,x}\, n_x + \tilde{\phi}_{w,y}\, n_y \right) \tilde{\lambda}_{w,n} \mathrm{d}\Gamma_{w,n} = -\int\limits_{\Omega} \tilde{\phi}_w\, p\ \mathrm{d}\Omega \\
\qquad\qquad \forall \tilde{\phi}_w \in \mathrm{H}^1_{h,p}\,, \\
\quad -\int\limits_{\Omega} \tilde{\phi}_{m_x,x}\, \tilde{w}_{,x}\ \mathrm{d}\Omega + \int\limits_{\Gamma} \tilde{\phi}_{m_x}\, \tilde{w}_{,x}\, n_x\ \mathrm{d}\Gamma + \int\limits_{\Gamma_{m_n}} \tilde{\phi}_{m_x}\, \tilde{\lambda}_{m_n}\, n_x^2\ \mathrm{d}\Gamma_{m_n} \\
+\int\limits_{\Gamma_{\bar{q}_n}} \left(\tilde{\phi}_{m_x,x}\, (n_x + n_x\, n_y^2) - \tilde{\phi}_{m_x,y}\, (n_x^2\, n_y) \right) \tilde{\lambda}_{\bar{q}_n}\ \mathrm{d}\Gamma_{\bar{q}_n} + \int\limits_{\Omega} \tilde{\phi}_{m_x}\, \tfrac{\tilde{m}_x - \nu\, \tilde{m}_y}{K\,(1-\nu^2)}\ \mathrm{d}\Omega = 0 \\
\qquad\qquad \forall \tilde{\phi}_{m_x} \in \mathrm{H}^1_{h,p}\,, \\
\quad -\int\limits_{\Omega} \tilde{\phi}_{m_y,y}\, \tilde{w}_{,y}\ \mathrm{d}\Omega + \int\limits_{\Gamma} \tilde{\phi}_{m_y}\, \tilde{w}_{,y}\, n_y\ \mathrm{d}\Gamma + \int\limits_{\Gamma_{m_n}} \tilde{\phi}_{m_y}\, \tilde{\lambda}_{m_n}\, n_y^2\ \mathrm{d}\Gamma_{m_n} \\
+\int\limits_{\Gamma_{\bar{q}_n}} \left(\tilde{\phi}_{m_y,y}\, (n_y + n_x^2\, n_y) - \tilde{\phi}_{m_y,x}\, (n_x\, n_y^2) \right) \tilde{\lambda}_{\bar{q}_n}\ \mathrm{d}\Gamma_{\bar{q}_n} + \int\limits_{\Omega} \tilde{\phi}_{m_y}\, \tfrac{\tilde{m}_y - \nu\, \tilde{m}_x}{K\,(1-\nu^2)}\ \mathrm{d}\Omega = 0 \\
\qquad\qquad \forall \tilde{\phi}_{m_y} \in \mathrm{H}^1_{h,p}\,, \\
\\
\quad -\int\limits_{\Omega} \tilde{\phi}_{m_{xy},x}\, \tilde{w}_{,y} + \tilde{\phi}_{m_{xy},y}\, \tilde{w}_{,x}\ \mathrm{d}\Omega + \int\limits_{\Gamma} \tilde{\phi}_{m_{xy}}\, (\tilde{w}_{,x}\, n_y + \tilde{w}_{,y}\, n_x)\ \mathrm{d}\Gamma \\
\quad +\int\limits_{\Omega} \tilde{\phi}_{m_{xy}}\, \tfrac{2\,(1+\nu)}{K\,(1-\nu^2)}\, \tilde{m}_{xy}\ \mathrm{d}\Omega + \int\limits_{\Gamma_{m_n}} 2\, \tilde{\phi}_{m_{xy}}\, \tilde{\lambda}_{m_n}\, n_x\, n_y\ \mathrm{d}\Gamma_{m_n} \\
\int\limits_{\Gamma_{\bar{q}_n}} \left(\tilde{\phi}_{m_{xy},x}\, n_y\, (1 - n_x^2 + n_y^2) + \tilde{\phi}_{m_{xy},y}\, n_x\, (1 + n_x^2 - n_y^2) \right) \tilde{\lambda}_{\bar{q}_n}\ \mathrm{d}\Gamma_{\bar{q}_n} = 0 \\
\qquad\qquad \forall \tilde{\phi}_{m_{xy}} \in \mathrm{H}^1_{h,p}\,, \\
\int\limits_{\Gamma_w} \tilde{\mu}_w\, \tilde{w}\ \mathrm{d}\Gamma_w = \int\limits_{\Gamma_w} \tilde{\mu}_w\, \hat{w}\ \mathrm{d}\Gamma_w \\
\qquad\qquad \forall \tilde{\mu}_w \in \mathrm{H}^{-1/2}_{h,p}(\Gamma_w)\,, \\
\int\limits_{\Gamma_{m_n}} \tilde{\mu}_{m_n} \left(\tilde{m}_x\, n_x^2 + \tilde{m}_y\, n_y^2 + 2\, \tilde{m}_{xy}\, n_x\, n_y \right) \mathrm{d}\Gamma_{m_n} = \int\limits_{\Gamma_{m_n}} \tilde{\mu}_{m_n}\, \hat{m}_n\ \mathrm{d}\Gamma_{m_n} \\
\qquad\qquad \forall \tilde{\mu}_{m_n} \in \mathrm{H}^{-1/2}_{h,p}(\Gamma_{m_n})\,, \\
\int\limits_{\Gamma_{w,n}} \tilde{\mu}_{w,n}\ (\tilde{w}_{,x}\, n_x + \tilde{w}_{,y}\, n_y)\ \mathrm{d}\Gamma_{w,n} = \int\limits_{\Gamma_{m_n}} \tilde{\mu}_{w,n}\, \hat{w}_{,n}\ \mathrm{d}\Gamma_{w,n} \\
\qquad\qquad \forall \tilde{\mu}_{w,n} \in \mathrm{H}^{-1/2}_{h,p-1}(\Gamma_{w,n})\,, \\
\int\limits_{\Gamma_{\bar{q}_n}} \tilde{\mu}_{\bar{q}_n} \Big(\tilde{m}_{x,x}\, n_x\, (1 + n_y^2) - \tilde{m}_{x,y}\, n_x^2\, n_y + \tilde{m}_{y,y}\, n_y\, (1 + n_x^2) - \tilde{m}_{y,x}\, n_y^2\, n_x \\
\quad +\tilde{m}_{xy,x}\, n_y\, (1 - n_x^2 + n_y^2) + \tilde{m}_{xy,y}\, n_x\, (1 + n_x^2 - n_y^2) \Big)\ \mathrm{d}\Gamma_{\bar{q}_n} \quad = \\
\qquad = \int\limits_{\Gamma_{\bar{q}_n}} \tilde{\mu}_{\bar{q}_n}\, \hat{\tilde{q}}_n\ \mathrm{d}\Gamma_{\bar{q}_n} \\
\qquad\qquad \forall \tilde{\mu}_{\bar{q}_n} \in \mathrm{H}^{-1/2}_{h,p-1}(\Gamma_{\bar{q}_n}).
\end{array}
\right. \tag{3.32}
$$

For both discrete weak forms the discrete inf-sup criterion must hold, which may be verified completing patch tests [4, 18]. The verification of the presented finite element formulations is done numerically by completion of convergence studies using solutions obtained via the manufactured solution method as well as several other reference solutions on a non-uniform mesh with curved boundaries, which are presented in chapter 4.
The mixed finite element formulation of the Kirchhoff-Love plate may now be used to approximate the solution. To further clarify the discretisation, the element stiffness matrix and the assembly of the global system stiffness matrix is described in the following sections.

3.4.3 Element Stiffness Matrices and Load Vector

The discrete weak forms may equivalently be rewritten as linear systems of equations [4, 18]. Solving those systems of the form $\boldsymbol{K}_g\,\boldsymbol{a} = \boldsymbol{f}$ yields an approximation $\boldsymbol{a}$ of the nodal degrees of freedom, which define the solution fields according to the ansatz made. The global stiffness matrix $\boldsymbol{K}_g$ and global load vector $\boldsymbol{f}$ are most efficiently computed by assembling contributions from the elements, i.e. element stiffness matrices $\boldsymbol{K}_l$ and element load vectors $\boldsymbol{b}_l$ corresponding to an element nodal degree of freedom vector $\boldsymbol{u}_l$, and the Lagrange multipliers.

$$\boldsymbol{K}_l = \begin{pmatrix} \boldsymbol{0} & \boldsymbol{K}_{l\,12} & \boldsymbol{K}_{l\,13} & \boldsymbol{K}_{l\,14} \\ \boldsymbol{K}_{l\,21} & \boldsymbol{K}_{l\,22} & \boldsymbol{K}_{l\,23} & \boldsymbol{0} \\ \boldsymbol{K}_{l\,31} & \boldsymbol{K}_{l\,32} & \boldsymbol{K}_{l\,33} & \boldsymbol{0} \\ \boldsymbol{K}_{l\,41} & \boldsymbol{0} & \boldsymbol{0} & \boldsymbol{K}_{l\,44} \end{pmatrix}, \qquad \boldsymbol{u}_l = \begin{pmatrix} \boldsymbol{w} \\ \boldsymbol{m}_x \\ \boldsymbol{m}_y \\ \boldsymbol{m}_{xy} \end{pmatrix}_l, \qquad \boldsymbol{b}_l = \begin{pmatrix} \boldsymbol{b}_{l\,1} \\ \boldsymbol{b}_{l\,2} \\ \boldsymbol{b}_{l\,3} \\ \boldsymbol{0} \end{pmatrix} \tag{3.33}$$

The submatrices $\boldsymbol{K}_l[i\,j]$ of the element stiffness matrix and the entries in the element load vector $\boldsymbol{b}_l$ for the methods introduced are computed as shown in the following equations. These matrices are assembled into the plates' stiffness matrix $\boldsymbol{K}_p$. Since the ansatz made for all primary field variables is the same, subscripts indicating the field are skipped. All shape functions involved are represented as vectors.

Submatrices and Vectors - Methods 1 & 2

$$\begin{aligned} \boldsymbol{K}_{l\,12} = &- \int_\Omega \boldsymbol{N}_{,x}^\top \boldsymbol{N}_{,x}\,\mathrm{d}\Omega - \int_{\Gamma_{\bar{q}n}} \boldsymbol{N}^\top \boldsymbol{N}_{,x}\,n_x + 2\,n_x\,n_y \left(\boldsymbol{N}_{,y}^\top n_x - \boldsymbol{N}_{,x}^\top n_y\right) \boldsymbol{N}\,\mathrm{d}\Gamma_{\bar{q}n} \\ &+ \int_{\Gamma^c_{\bar{q}n}} \boldsymbol{N}^\top \boldsymbol{N}_{,x}\,n_x\,\mathrm{d}\Gamma^c_{\bar{q}n} \end{aligned} \tag{3.34a}$$

$$\begin{aligned} \boldsymbol{K}_{l\,13} = &- \int_\Omega \boldsymbol{N}_{,y}^\top \boldsymbol{N}_{,y}\,\mathrm{d}\Omega - \int_{\Gamma_{\bar{q}n}} \boldsymbol{N}^\top \boldsymbol{N}_{,y}\,n_y + 2\,n_x\,n_y \left(-\boldsymbol{N}_{,y}^\top n_x + \boldsymbol{N}_{,x}^\top n_y\right) \boldsymbol{N}\,\mathrm{d}\Gamma_{\bar{q}n} \\ &+ \int_{\Gamma^c_{\bar{q}n}} \boldsymbol{N}^\top \boldsymbol{N}_{,y}\,n_y\,\mathrm{d}\Gamma^c_{\bar{q}n} \end{aligned} \tag{3.34b}$$

$$\begin{aligned} \boldsymbol{K}_{l\,14} = &- \int_\Omega \boldsymbol{N}_{,x}^\top \boldsymbol{N}_{,y} + \boldsymbol{N}_{,y}^\top \boldsymbol{N}_{,x}\,\mathrm{d}\Omega - \int_{\Gamma_{\bar{q}n}} \boldsymbol{N}^\top\,(\boldsymbol{N}_{,x}\,n_y + \boldsymbol{N}_{,y}\,n_x) - 2\left(n_x^2 - n_y^2\right) \\ &\left(\boldsymbol{N}_{,y}^\top n_x - \boldsymbol{N}_{,x}^\top n_y\right) \boldsymbol{N}\,\mathrm{d}\Gamma_{\bar{q}n} + \int_{\Gamma^c_{\bar{q}n}} \boldsymbol{N}^\top\,(\boldsymbol{N}_{,y}\,n_x + \boldsymbol{N}_{,x}\,n_y)\,\mathrm{d}\Gamma^c_{\bar{q}n} \end{aligned} \tag{3.34c}$$

$$\boldsymbol{K}_{l\,21} = -\int_{\Omega} \boldsymbol{N}_{,x}^{\top}\boldsymbol{N}_{,x}\ \mathrm{d}\Omega - \int_{\Gamma_{w,n}} \boldsymbol{N}^{\top}\boldsymbol{N}_{,y}\, n_y\ \mathrm{d}\Gamma_{w,n} + \int_{\Gamma^c_{w,n}} \boldsymbol{N}^{\top}\boldsymbol{N}_{,x}\, n_x\ \mathrm{d}\Gamma^c_{w,n} \tag{3.34d}$$

$$\boldsymbol{K}_{l\,22} = \frac{1}{K\,(1-\nu^2)}\int_{\Omega} \boldsymbol{N}^{\top}\,\boldsymbol{N}\ \mathrm{d}\Omega\,, \qquad \boldsymbol{K}_{l\,23} = -\frac{\nu}{K\,(1-\nu^2)}\int_{\Omega} \boldsymbol{N}^{\top}\boldsymbol{N}\ \mathrm{d}\Omega \tag{3.34e}$$

$$\boldsymbol{K}_{l\,31} = -\int_{\Omega} \boldsymbol{N}_{,y}^{\top}\boldsymbol{N}_{,y}\ \mathrm{d}\Omega - \int_{\Gamma_{w,n}} \boldsymbol{N}^{\top}\boldsymbol{N}_{,x}\, n_x\ \mathrm{d}\Gamma_{w,n} + \int_{\Gamma^c_{w,n}} \boldsymbol{N}^{\top}\boldsymbol{N}_{,y}\, n_y\ \mathrm{d}\Gamma^c_{w,n} \tag{3.34f}$$

$$\boldsymbol{K}_{l\,32} = \boldsymbol{K}_{l\,32}^{\top} = \boldsymbol{K}_{l\,23}\,, \qquad \boldsymbol{K}_{l\,33} = \boldsymbol{K}_{l\,33}^{\top} = \boldsymbol{K}_{l\,22} \tag{3.34g}$$

$$\boldsymbol{K}_{l\,41} = -\int_{\Omega} \boldsymbol{N}_{,x}^{\top}\boldsymbol{N}_{,y} + \boldsymbol{N}_{,y}^{\top}\boldsymbol{N}_{,x}\ \mathrm{d}\Omega + \int_{\Gamma} \boldsymbol{N}^{\top}\left(\boldsymbol{N}_{,x}\, n_y + \boldsymbol{N}_{,y}\, n_x\right)\ \mathrm{d}\Gamma \tag{3.34h}$$

$$\boldsymbol{K}_{l\,44} = \frac{2\,(1+\nu)}{K\,(1-\nu^2)}\int_{\Omega} \boldsymbol{N}^{\top}\boldsymbol{N}\ \mathrm{d}\Omega \tag{3.34i}$$

$$\boldsymbol{b}_{l\,1} = -\int_{\Omega} \boldsymbol{N}^{\top} p\ \mathrm{d}\Omega - \int_{\Gamma_{\bar{q}n}} 2\,\boldsymbol{N}^{\top}\hat{\bar{q}}_n\ \mathrm{d}\Gamma_{\bar{q}_n}\,, \qquad \boldsymbol{b}_{l\,2} = -\int_{\Gamma_{w,n}} \boldsymbol{N}^{\top}\hat{w}_{,n}\ \mathrm{d}\Gamma_{w,n} = \boldsymbol{b}_{l\,3} \tag{3.35}$$

Submatrices and Vectors - Method 3

$$\boldsymbol{K}_{l\,12} = -\int_{\Omega} \boldsymbol{N}_{,x}^{\top}\boldsymbol{N}_{,x}\ \mathrm{d}\Omega + \int_{\Gamma} \boldsymbol{N}^{\top}\boldsymbol{N}_{,x}\, n_x\ \mathrm{d}\Gamma \tag{3.36a}$$

$$\boldsymbol{K}_{l\,13} = -\int_{\Omega} \boldsymbol{N}_{,y}^{\top}\boldsymbol{N}_{,y}\ \mathrm{d}\Omega + \int_{\Gamma} \boldsymbol{N}^{\top}\boldsymbol{N}_{,y}\, n_y\ \mathrm{d}\Gamma \tag{3.36b}$$

$$\boldsymbol{K}_{l\,14} = -\int_{\Omega} \boldsymbol{N}_{,x}^{\top}\boldsymbol{N}_{,y} + \boldsymbol{N}_{,y}^{\top}\boldsymbol{N}_{,x}\ \mathrm{d}\Omega + \int_{\Gamma} \boldsymbol{N}^{\top}\left(\boldsymbol{N}_{,y}\, n_x + \boldsymbol{N}_{,x}\, n_y\right)\ \mathrm{d}\Gamma \tag{3.36c}$$

$$\boldsymbol{K}_{l\,21} = -\int_{\Omega} \boldsymbol{N}_{,x}^{\top}\boldsymbol{N}_{,x}\ \mathrm{d}\Omega + \int_{\Gamma} \boldsymbol{N}^{\top}\boldsymbol{N}_{,x}\, n_x\ \mathrm{d}\Gamma \tag{3.36d}$$

$$\boldsymbol{K}_{l\,22} = \frac{1}{K\,(1-\nu^2)}\int_{\Omega} \boldsymbol{N}^{\top}\,\boldsymbol{N}\ \mathrm{d}\Omega\,, \qquad \boldsymbol{K}_{l\,23} = -\frac{\nu}{K\,(1-\nu^2)}\int_{\Omega} \boldsymbol{N}^{\top}\boldsymbol{N}\ \mathrm{d}\Omega \tag{3.36e}$$

$$\boldsymbol{K}_{l\,31} = -\int_{\Omega} \boldsymbol{N}_{,y}^{\top}\boldsymbol{N}_{,y}\ \mathrm{d}\Omega + \int_{\Gamma} \boldsymbol{N}^{\top}\boldsymbol{N}_{,y}\, n_y\ \mathrm{d}\Gamma \tag{3.36f}$$

$$\boldsymbol{K}_{l\,32} = \boldsymbol{K}_{l\,32}^{\top} = \boldsymbol{K}_{l\,23}\,, \qquad \boldsymbol{K}_{l\,33} = \boldsymbol{K}_{l\,33}^{\top} = \boldsymbol{K}_{l\,22} \tag{3.36g}$$

$$\boldsymbol{K}_{l\,41} = -\int_{\Omega} \boldsymbol{N}_{,x}^{\top}\boldsymbol{N}_{,y} + \boldsymbol{N}_{,y}^{\top}\boldsymbol{N}_{,x}\;\mathrm{d}\Omega + \int_{\Gamma} \boldsymbol{N}^{\top}\left(\boldsymbol{N}_{,x}\,n_y + \boldsymbol{N}_{,y}\,n_x\right)\;\mathrm{d}\Gamma \tag{3.36h}$$

$$\boldsymbol{K}_{l\,44} = \frac{2\,(1+\nu)}{K\,(1-\nu^2)} \int_{\Omega} \boldsymbol{N}^{\top}\boldsymbol{N}\;\mathrm{d}\Omega \tag{3.36i}$$

$$\boldsymbol{b}_{l\,1} = -\int_{\Omega} \boldsymbol{N}^{\top} p\;\mathrm{d}\Omega\,, \qquad \boldsymbol{b}_{l\,2} = \boldsymbol{0} = \boldsymbol{b}_{l\,3} \tag{3.37}$$

The element load vector simplifies significantly, if the boundary conditions are enforced via Lagrange multipliers, which are added to the system after assembling the plates' stiffness matrix $\boldsymbol{K}_p$.

3.4.4 Lagrange Multipliers

The global system of equations has the following form:

$$\boldsymbol{K}_g\,\boldsymbol{a} = \boldsymbol{f} \qquad \Longrightarrow \qquad \begin{pmatrix} \boldsymbol{K}_p & \boldsymbol{C}^{\top} \\ \boldsymbol{C} & \boldsymbol{0} \end{pmatrix} \begin{pmatrix} \boldsymbol{u} \\ \boldsymbol{\lambda} \end{pmatrix} = \begin{pmatrix} \boldsymbol{b} \\ \boldsymbol{d} \end{pmatrix} \tag{3.38}$$

Where the plates' stiffness matrix $\boldsymbol{K}_p$ is assembled from element stiffness matrices $\boldsymbol{K}_l$ and the additional constraints are discretised via stiffness matrices of the Lagrange multipliers C. The vector $\boldsymbol{\lambda}$ therein contains the degrees of freedom of the Lagrange multipliers λ_i, which correspond to the entries in $\boldsymbol{C}$ and $\boldsymbol{d}$. The matrix $\boldsymbol{C}$ is analogously to $\boldsymbol{K}_p$ computed from element contributions.

Lagrange Multipliers - Methods 1 & 2

Within the methods 1 and 2 Lagrange multipliers are utilised to enforce Dirichlet boundary conditions solely. The matrix $\boldsymbol{C}$ is assembled from $\boldsymbol{C}_l$ corresponding to entries in $\boldsymbol{\lambda}_l$ and $\boldsymbol{d}_l$. Additionally the primary field variables are written above, to clarify the position of the submatrices:

$$\boldsymbol{C}_l = \begin{array}{c} \begin{matrix} w & m_x & m_y & m_{xy} \end{matrix} \\ \begin{pmatrix} \boldsymbol{C}_w & \boldsymbol{0} & \boldsymbol{0} & \boldsymbol{0} \\ \boldsymbol{0} & \boldsymbol{C}_{m_n\,2} & \boldsymbol{C}_{m_n\,3} & \boldsymbol{C}_{m_n\,4} \end{pmatrix} \end{array}, \qquad \boldsymbol{\lambda}_l = \begin{pmatrix} \boldsymbol{\lambda}_w \\ \boldsymbol{\lambda}_{m_n} \end{pmatrix}_l, \qquad \boldsymbol{d}_l = \begin{pmatrix} \boldsymbol{d}_w \\ \boldsymbol{d}_{m_n} \end{pmatrix} \tag{3.39}$$

The submatrices of $\boldsymbol{C}_l$ and the entries in $\boldsymbol{d}_l$ for the methods 1 and 2 are computed as shown in the following equations. Since the ansatz made for all primary field variables is the same, subscripts indicating the field are again skipped.

$$\boldsymbol{C}_w = \int_{\Gamma_w} \boldsymbol{M}^{\top}\boldsymbol{N}\;\mathrm{d}\Gamma_w\,, \qquad \boldsymbol{C}_{m_n\,2} = \int_{\Gamma_{m_n}} \boldsymbol{M}^{\top}\boldsymbol{N}\,n_x^2\;\mathrm{d}\Gamma_{m_n} \tag{3.40a}$$

$$\boldsymbol{C}_{m_n\,3} = \int_{\Gamma_{m_n}} \boldsymbol{M}^{\top}\boldsymbol{N}\,n_y^2\;\mathrm{d}\Gamma_{m_n}\,, \qquad \boldsymbol{C}_{m_n\,4} = \int_{\Gamma_{m_n}} \boldsymbol{M}^{\top}\boldsymbol{N}\,2\,n_x\,n_y\;\mathrm{d}\Gamma_{m_n} \tag{3.40b}$$

$$\boldsymbol{d}_w = \int_{\Gamma_w} \boldsymbol{M}^{\top}\hat{w}\;\mathrm{d}\Gamma_w \qquad \boldsymbol{d}_{m_n} = \int_{\Gamma_{m_n}} \boldsymbol{M}^{\top}\hat{m}_n\;\mathrm{d}\Gamma_{m_n} \tag{3.41}$$

Lagrange Multipliers - Method 3

Within method 3 Dirichlet as well as Neumann boundary conditions are applied via Lagrange multipliers. Analogous to the previously presented the matrix $\boldsymbol{C}_l$ is assembled from Lagrange multiplier element contributions $\boldsymbol{C}_l$:

$$\boldsymbol{C}_l = \begin{array}{c} \begin{matrix} w & m_x & m_y & m_{xy} \end{matrix} \\ \begin{pmatrix} \boldsymbol{C}_w & \mathbf{0} & \mathbf{0} & \mathbf{0} \\ \boldsymbol{C}_{w,n} & \mathbf{0} & \mathbf{0} & \mathbf{0} \\ \mathbf{0} & \boldsymbol{C}_{m_n\,2} & \boldsymbol{C}_{m_n\,3} & \boldsymbol{C}_{m_n\,4} \\ \mathbf{0} & \boldsymbol{C}_{\bar{q}_n\,2} & \boldsymbol{C}_{\bar{q}_n\,3} & \boldsymbol{C}_{\bar{q}_n\,4} \end{pmatrix} \end{array}, \qquad \boldsymbol{\lambda}_l = \begin{pmatrix} \boldsymbol{\lambda}_w \\ \boldsymbol{\lambda}_{w,n} \\ \boldsymbol{\lambda}_{m_n} \\ \boldsymbol{\lambda}_{\bar{q}_n} \end{pmatrix}_l, \qquad \boldsymbol{d}_l = \begin{pmatrix} \boldsymbol{d}_w \\ \boldsymbol{d}_{w,n} \\ \boldsymbol{d}_{m_n} \\ \boldsymbol{d}_{\bar{q}_n} \end{pmatrix} \tag{3.42}$$

The matrices $\boldsymbol{C}_w$, all $\boldsymbol{C}_{m_n}$ and the entries $\boldsymbol{d}_w$ and $\boldsymbol{d}_{m_n}$ are computed similar to methods 1 and 2, the remaining entries are defined in the following equations. The subscripts of the shape functions indicating the field are again skipped.

$$\boldsymbol{C}_{w,n} = \int_{\Gamma_{w,n}} \boldsymbol{M}^{d\,\top} \left(\boldsymbol{N}_{,x}\, n_x + \boldsymbol{N}_{,y}\, n_y\right)\, \mathrm{d}\Gamma_{w,n} \tag{3.43a}$$

$$\boldsymbol{C}_{\bar{q}_n\,2} = \int_{\Gamma_{\bar{q}n}} \boldsymbol{M}^{d\,\top} \left(\boldsymbol{N}_{,x}\, n_x\,(1+n_y^2) - \boldsymbol{N}_{,y}\, n_x^2\, n_y\right)\, \mathrm{d}\Gamma_{\bar{q}_n} \tag{3.43b}$$

$$\boldsymbol{C}_{\bar{q}_n\,3} = \int_{\Gamma_{\bar{q}n}} \boldsymbol{M}^{d\,\top} \left(\boldsymbol{N}_{,y}\, n_y\,(1+n_x^2) - \boldsymbol{N}_{,x}\, n_x\, n_y^2\right)\, \mathrm{d}\Gamma_{\bar{q}_n} \tag{3.43c}$$

$$\boldsymbol{C}_{\bar{q}_n\,4} = \int_{\Gamma_{\bar{q}n}} \boldsymbol{M}^{d\,\top} \left(\boldsymbol{N}_{,x}\, n_y\,(1-n_x^2+n_y^2) - \boldsymbol{N}_{,y}\, n_x\,(1+n_x^2-n_y^2)\right)\, \mathrm{d}\Gamma_{\bar{q}_n} \tag{3.43d}$$

$$\boldsymbol{d}_{w,n} = \int_{\Gamma_{w,n}} \boldsymbol{M}^{d\,\top} \hat{w}_{,n}\, \mathrm{d}\Gamma_{w,n} \qquad \boldsymbol{d}_{\bar{q}_n} = \int_{\Gamma_{\bar{q}_n}} \boldsymbol{M}^{d\,\top} \hat{\bar{q}}_n\, \mathrm{d}\Gamma_{\bar{q}_n} \tag{3.44}$$

With the introduced element matrices $\boldsymbol{K}_l$ and $\boldsymbol{C}_l$ the global stiffness matrix $\boldsymbol{K}_g$ is assembled. The numbering of the degrees of freedom on the element level is chosen differently from the global numbering. Hence the submatrices of the element stiffness matrix and the load vector are still computed in a straight forward manner, but additionally the plates' stiffness matrix $\boldsymbol{K}_p$ has a banded structure. The resulting linear system of equations is indefinite and may become severly ill-conditioned for large numbers of Lagrange multipliers. The linear system is solved using LU-decomposition, since $\boldsymbol{K}_g$ is not symmetric due to the boundary term evaluation.
Further desired quantities such as the shear forces or the forces F_c arising in the corners of the plate may be computed in a postprocessing step using the shape functions and their derivatives. The expected order of convergence for primary variables is $\mathcal{O}(h^p)$ and hence for the shear forces $\mathcal{O}(h^{p-1})$, which is a tremendous advantage of this mixed method over standard linear displacement based plate elements.

4 Numerical results

The mixed finite element formulations derived are tested considering several examples and convergence studies are performed to compare the effectiveness of the three approaches to prescribe boundary conditions. The problems considered include Manufactured Solutions, to verify the imposing of inhomogeneous boundary conditions on non-uniform meshes with curved boundaries, as well as reference solutions for square and circular domains obtained via derivation in a classical sense taken from well-known references [17, 2].
The studies presented are merely an extract of the investigations carried out, but illustrate all major aspects observed. The errors computed are the absolute and relative $\mathrm{L}_2(\Omega)$ errors, which are always depicted in logarithmic scale on the ordinate paired with the global mesh refinement factor n_{elem} on the abscissa. The expected rates of convergence are plotted as dashed lines of the same color as the associated curves referring to different ansatz orders.
The parameters considered are $t = 0.2\,[m]$, $E = 30000\,[N/m^2]$ and $\nu = 0.3\,[-]$, resulting in $K \approx 21.98$. Therefore the loading is also entered in $[N/m^2]$ and equals $p = 0.75\,[N/m^2]$ for the mechanical problems examined. As long as the values entered do not lead to a significant increase of round-off errors, they do not have an impact on the quality of the approximation.

4.1 Manufactured Solution

To test the implementation of varying inhomogeneous boundary conditions in a mesh, that is represented exactly, the deformation w is assumed and inserting into the governing equations yields the associated fields and the loading p. The boundary conditions constructed in this manner are available in any point of the domain and may therefore easily applied to approximate the solution to the given boundary value problem. Additionally singularities, inducing reduced convergence rates, are avoided by choosing an appropriate function w:

$$w(\boldsymbol{x}) = \left(sin\Big(\frac{x}{5}\Big) + 2\, cos\Big(\frac{x\,y}{5}\Big) \right) 10^{-5} \tag{4.1}$$

Rewriting the governing equations given in chapter 2 gives the following expressions, which may be computed trivially [2]:

$$\begin{aligned} m_x &= -K\,(w_{,xx} + \nu\, w_{,yy})\,, \qquad m_y = -K\,(w_{,yy} + \nu\, w_{,xx})\,, \qquad m_{xy} = -K\,(1-\nu)\,w_{,xy} \\ q_x &= -K\,(w_{,xxx} + w_{,yyx}) = -K\,(\Delta w)_{,x}\,, \qquad q_y = -K\,(w_{,yyy} + w_{,xxy}) = -K\,(\Delta w)_{,y} \end{aligned} \tag{4.2}$$

The load per unit area $p(\boldsymbol{x})$ solving the partial differential equation 2.12 in $\Omega \subset \mathbb{R}^2$ is:

$$\Delta^2 w = \frac{p}{K} \quad \Longleftrightarrow \quad p = K\,\Delta^2 w = K\,(w_{,xxxx} + w_{,xxyy} + w_{,yyyy}) \tag{4.3}$$

The explicit expressions are not given here for brevity. The Dirichlet and Neumann data is computed in each integration or collocation point. Using the transformation equations 2.19 the values enforced depend on the angle φ, which is computed using the element area weighted unit outward normal of the coinciding elements.

4.1.1 Mesh Construction

The mesh considered is generated via mapping a mesh of a rectangular domain with side lengths of l_x and l_y by a mapping $\Phi_1(\boldsymbol{x})$ scaled by c_g:

$$\Phi_1 : \boldsymbol{x} \mapsto \tilde{\boldsymbol{x}}\,, \qquad \Phi_1(\boldsymbol{x}) = \begin{pmatrix} x + 1 + c_g \, \frac{l_x}{5} \, cos\left(\frac{\pi\, x}{3\, l_x}\right) \, sin\left(\frac{\pi\, y}{3\, l_y}\right) \\ \\ y + 1 + c_g \, \frac{3\, l_y}{10} \, sin\left(\left(\frac{\pi\, x}{l_x} + \frac{\pi}{2}\right)\frac{3}{2}\right) \end{pmatrix}, \qquad \text{with:} \quad c_g \in \mathbb{R} \tag{4.4}$$

If the configuration of the mapping $\Phi_1(\boldsymbol{x})$ is not done with enough caution, the approximation properties of the mesh are severely corrupted or degenerated elements occur.
On the resulting domain, the solution of the boundary value problem is approximated enforcing Dirichlet boundary conditions in w and m_n. Neumann boundary conditions are met since the loading is constructed, and the implementation involving the treating of inhomogeneous Neumann boundary conditions is tested.

4.1.2 Manufactured solution - Dirichlet and Neumann boundary conditions

The presented mixed finite element formulation is utilised to approximate the solution to the boundary value problem of the Kirchhoff-Love plate with all essential and natural boundary conditions enforced along the whole boundary of the domain. The mesh considered as well as markers indicating nodes on a boundary with given boundary conditions is depicted in figure 4.1.

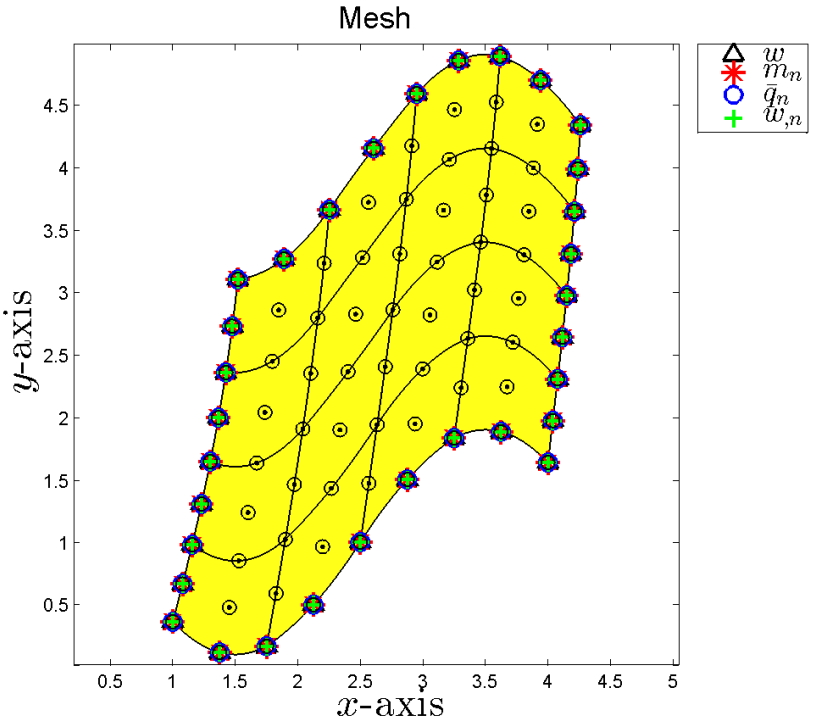

Fig. 4.1: Mesh considered: 4×4 quadrilateral elements of second order

The performed convergence studies indicate, that the methods approximate the solution of the deflection of the plate with optimal convergence rates and are in some cases superconvergent for the first orders using quadrilateral Lagrange elements (see figure 4.2). Using triangular Lagrange elements also leads to superconvergent behaviour for some orders, but linear triangles do not converge at all (see figure 4.3). This result is known and discussed in the literature, e.g. *Boffi et al.*[5].

In general quadrilateral elements performed better or gave the same results as triangular elements in most cases, which may be due to the mixed terms involved in the shape functions. The methods 1 and 2 yield almost identical results in this test and are therefore not depicted individually.

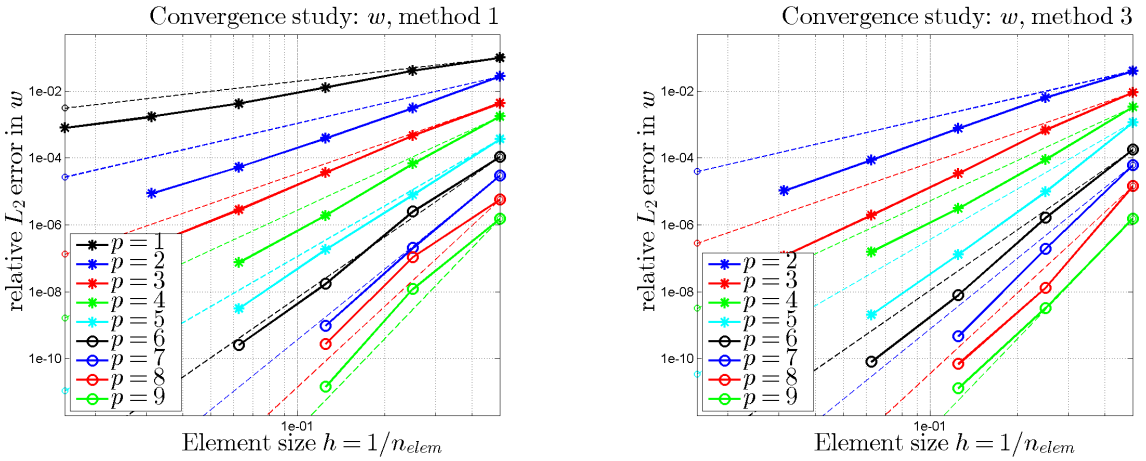

(a) Methods 1 and 2 **(b)** Method 3

Fig. 4.2: Convergence studies in w using quadrilateral elements

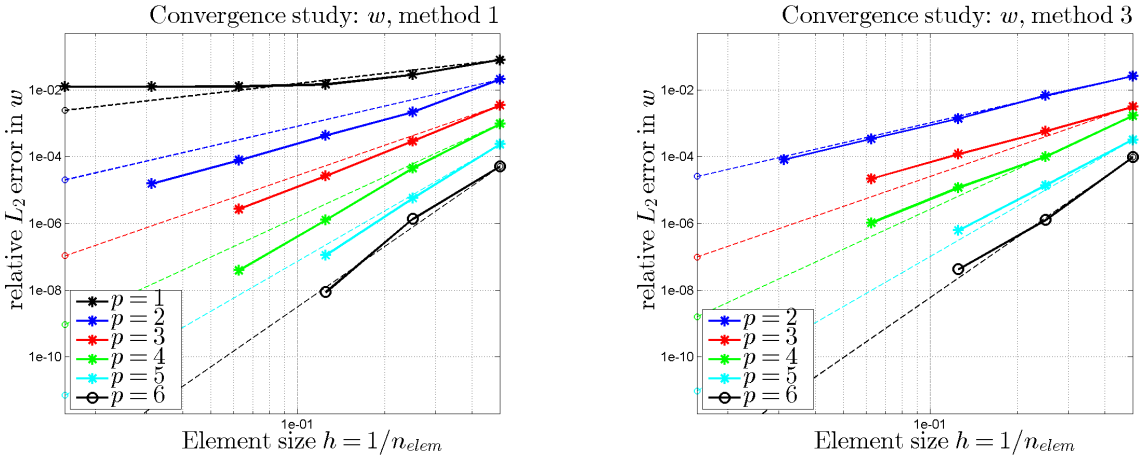

(a) Methods 1 and 2 **(b)** Method 3

Fig. 4.3: Convergence studies in w using triangular elements

The approximation of the internal moments of the plate is in general worse than the deflection although the shape functions used to discretise the ansatz have the same polynomial degree. The reason being that, the internal moment fields are more sensible to mesh distortion, as concluded from section 4.2. Methods 1 and 2 yield almost identical results. Figure 4.4 compares the convergence behaviour of the bending moment m_x using methods 1 and 3.
The results obtained show uniform convergence, which is for some orders slightly worse than the expected $\mathcal{O}(h^p)$. Nevertheless higher order convergence rates are reached and the mentioned effect remains small in this specific test.

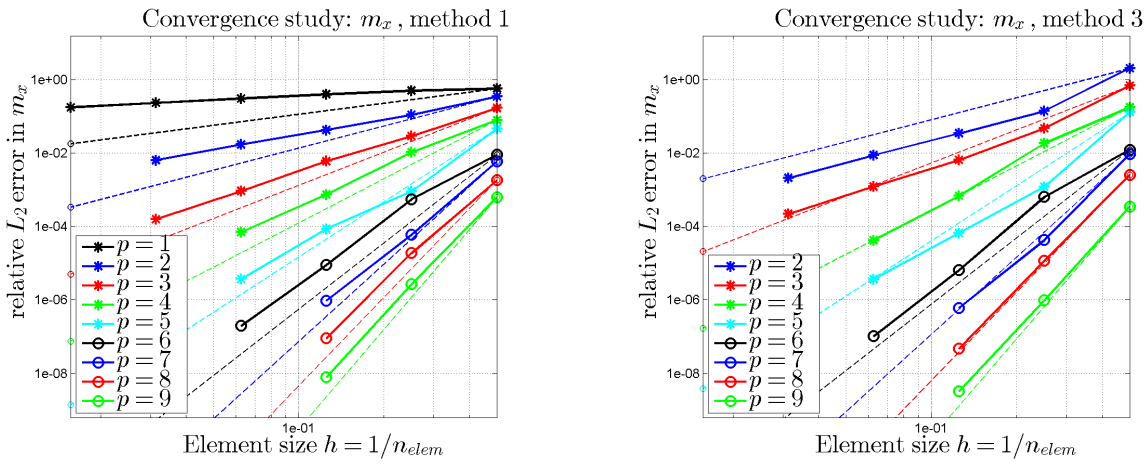

(a) Methods 1 and 2 **(b)** Method 3

Fig. 4.4: Convergence studies in m_x using quadrilateral elements

The shear forces are computed in a postprocessing step from the bending moments and hence also suffer from this loss of accuracy and do in general not reach the expected $\mathcal{O}(h^{p-1})$ rate of convergence (see figure 4.5), if the mesh is distorted. Nevertheless method 3 performs slightly better comparing the shear forces and internal moments.
The discontinuous nodal values of the shear forces are averaged over the weighted element areas and interpolated into the integration points using the shape functions, which are one order higher. Nevertheless the gained accuracy is not significant.

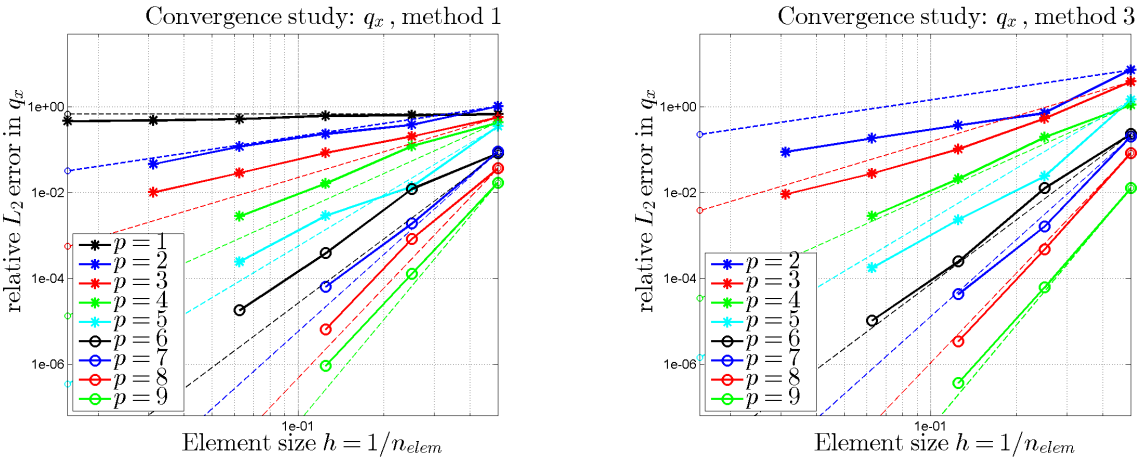

(a) Methods 1 and 2 **(b)** Method 3

Fig. 4.5: Convergence studies in q_x using quadrilateral elements

After solving the linear system of equations the Lagrange multipliers λ_{m_n} are used to compute the relative L_2 error in m_n, which is a boundary condition on Γ_{m_n}. Within methods 2 and 3 the Lagrange elements on the boundary are utilised to integrate over the boundary. If method 1 is used, Lagrange elements are constructed. This results in three convergence studies depicted in figure 4.6, showing optimal convergence rates.
The improper convergence of m_n using linear triangles is clearly visible in the study of method 1. Though the kink in the corresponding curve emerges at the fifth refinement step, while the kink in the convergence curve of the deformation w using the same method occurs in the third refinement step (see figures 4.6c and 4.6d). The respective kink is not apparent in the convergence curve of

m_n using method 2 and the curves associated with the deformation w are of the same appearance. Which leads to the conclusion, that the boundary conditions in m_n are approximated sufficiently for all methods used.

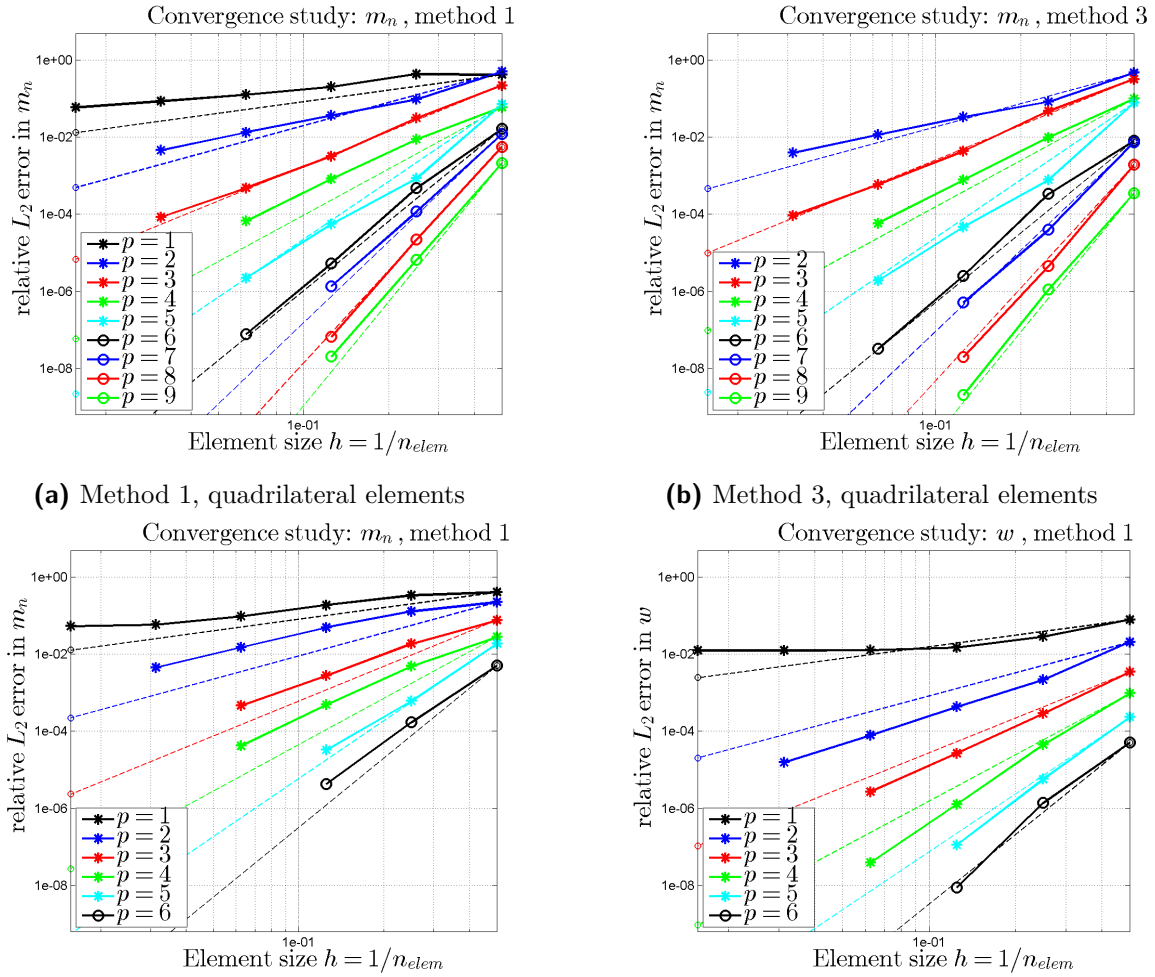

(a) Method 1, quadrilateral elements

(b) Method 3, quadrilateral elements

(c) Method 1, triangular elements

(d) Method 1, triangular elements

Fig. 4.6: Convergence studies in m_n and w, comparing triangular and quadrilateral elements

Finally the solution fields w, m_x and q_x are presented using the shape functions and their derivatives of each element (see figure 4.7, left). Additionally the relative L_2 error distribution is shown for a mesh of 15×15 quintic elements (see figure 4.7, right). The contributions to the L_2 error are depicted as point values and a surface is reconstructed using a Delauney triangulation. All methods result in similar L_2 error distributions, with high values in corners, along edges or across the domain, where solution values are close to zero. The error calculation in theses points involves larger round-off errors, but studies examinig the absolute L_2 error show the same effects as the ones depicted.
The boundary conditions are enforced using method 2, but as already mentioned, every method produces converging results.
Moreover the derivatives of the primary variables feature strong jumps and peaks in the element corners on the boundary, as observed in figure 4.7e. The introduction of Kirchhoff's effective shear force $\bar{q}_n$ as a boundary condition, substituting the shear force and twisting moment, reflects in the quality and appearance of the solution. To emphasize this issue, all figures containing shear forces do not display averaged nodal values, but the raw data computed. The geometry of the mesh is exact, but features kinks between the elements on the boundary. The internal moments and the shear forces therefore yield higher errors on the boundaries, where m_n is prescribed.

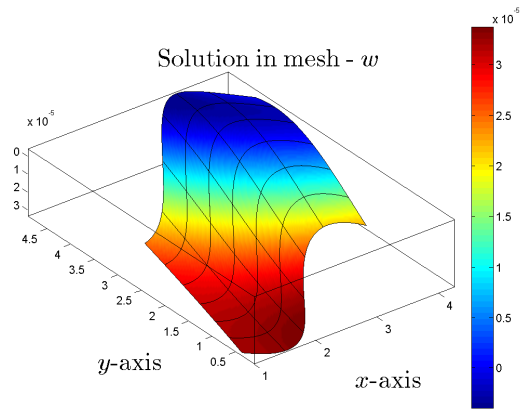

(a) Solution: deformation w

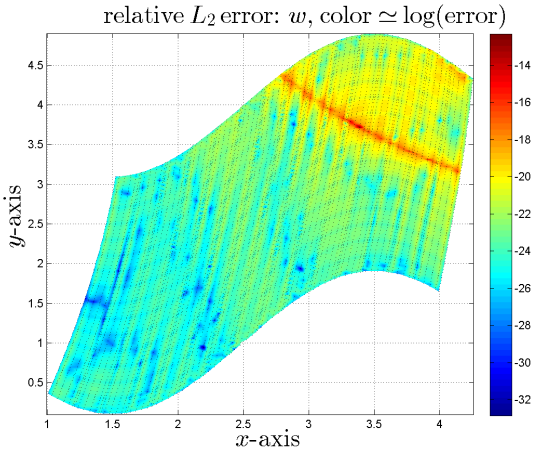

(b) Error: deformation w

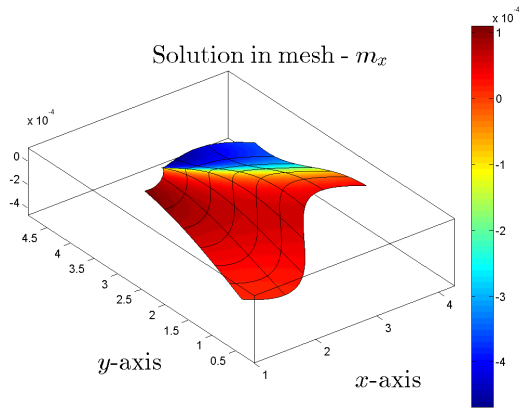

(c) Solution: bending moment m_x

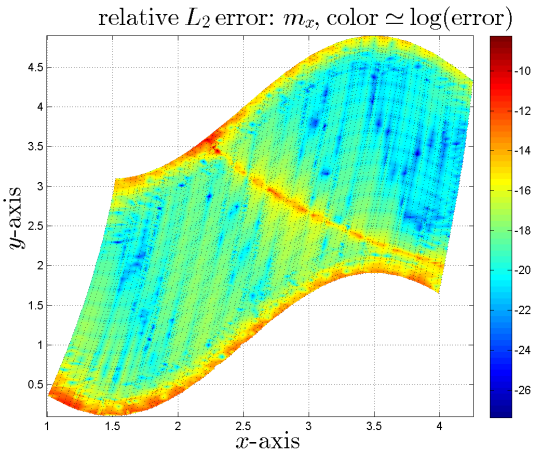

(d) Error: bending moment m_x

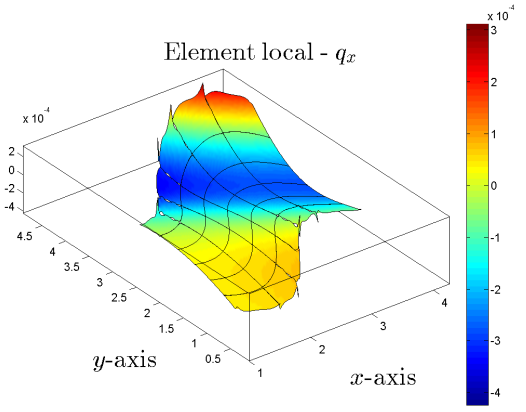

(e) Solution: shear force q_x

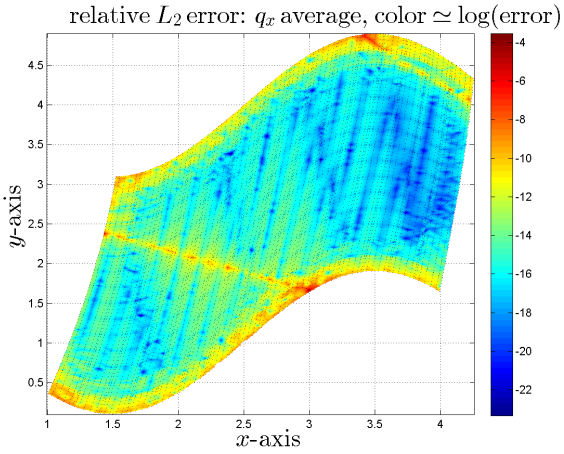

(f) Error: shear force q_x average

Fig. 4.7: Mesh of 6×6 quintic elements - solutions (l.) and L_2 error distribution in Ω (r.)

Finally the study of this test is complemented by commenting on the behaviour of linear triangles. Using linear triangles the solution of the deformation of the plate is of smooth appearance and therefore not presented again. The incorrect approximation of w is only detected examining the convergence tables already shown. All bending moments however, and therefore the shear forces, feature major errors. The bending moment fields show oscillations, which remain under h-refinement.

Increasing the order of the Finite Elements used diminishes the effect, but does not completely erase it, as can also be seen in figure 4.7 (right). Figure 4.8 depicts the solution m_x in the domain meshed with 1600 linear triangular elements. Method 2 is chosen to apply boundary conditions, but all methods result in solutions featuring oscillations.

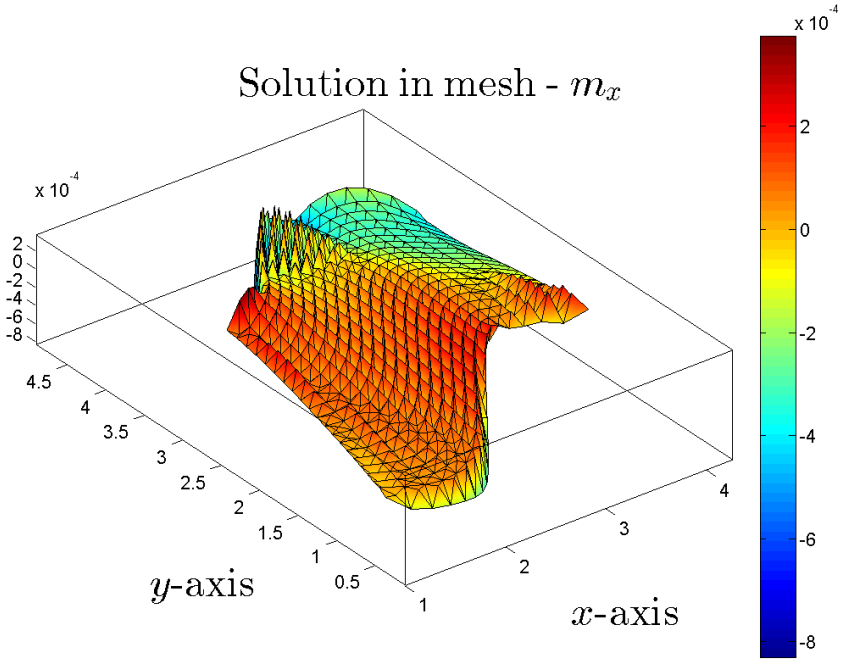

Fig. 4.8: Oscillations in the bending moment m_x - 1600 linear triangular elements

4.1.3 Manufactured solution - Dirichlet boundary conditions

Within the following study the same manufactured solution given in equation 4.1 is considered. In this examination again the Dirichlet boundary conditions in w and m_n are prescribed, but the Neumann boundary conditions are treated as unknown. Therefore the associated terms entering the linear system of equations in case of unknown natural boundary conditions are tested and the convergence behaviour is investigated.
Analysing the results shows, that the results and observations are identical to the ones observed considering Dirichlet and Neumann boundary conditions. All methods yield higher order convergence, applying any method results in almost identical convergence studies not only in the deformations but in every study. The deformation of the plate is again superconvergent for some orders and is in general better approximated than the internal moments of the plate.
The shear forces converge with $\mathcal{O}(h^{p-1})$. Linear triangular elements do not converge, but the expected $\mathcal{O}(h^p)$ convergence is reached for higher order triangular elements. Enforcing the boundary conditions is for all methods accomplished with success, the errors in the domain are distributed similar to those already imaged in figure 4.7 (r.), i.e. high values occur in corners or along edges and in points, where the solution value is almost zero.
The results are not shown here since they feature the same characteristics as the ones in figure 4.7 (l.).

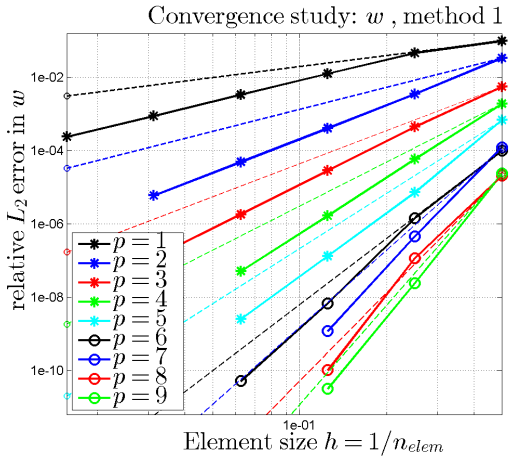

(a) Methods 1 and 2, quadrilaterals

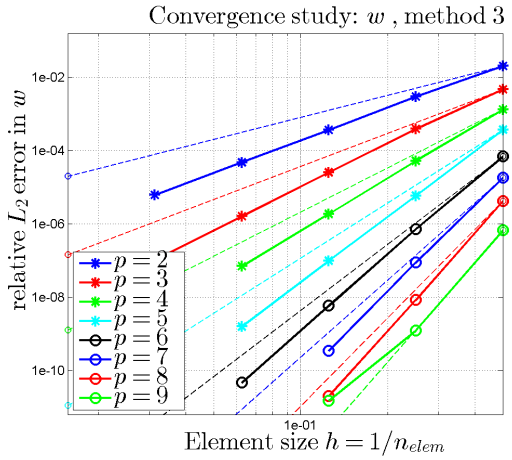

(b) Method 3, quadrilaterals

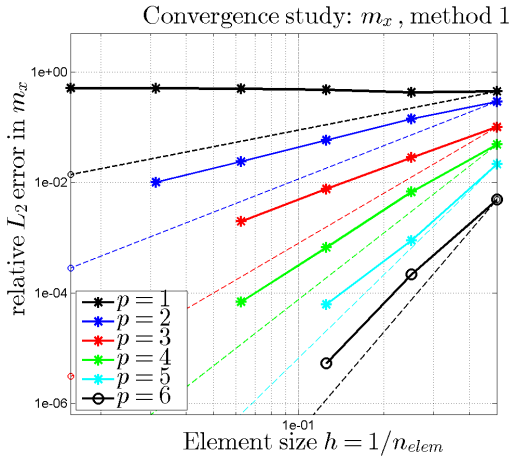

(c) Methods 1 and 2, triangles

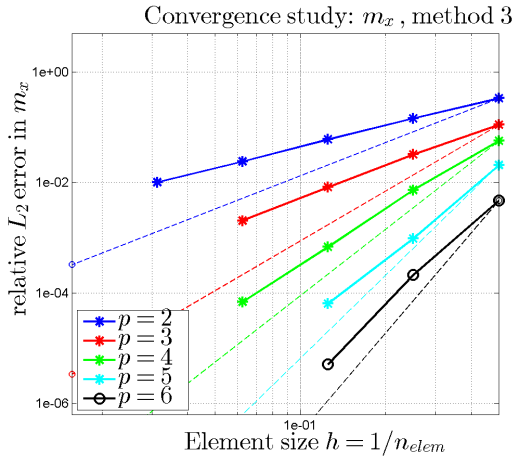

(d) Method 3, triangles

Fig. 4.9: Convergence studies in w (t.) and m_x (b.) using quadrilateral (t.) and triangular (b.) elements

These results complete the studies on plates with manufactured solution on a mapped rectangular domain.

4.2 Square Plates with Various Boundary Conditions

Within this section the convergence behaviour of the presented mixed Finite Element formulations is tested on square plates using the three methods to apply boundary conditions. Therein the main focus lies on comparing the different methods and solutions with symmetry boundary conditions introduced.
Therefore the convergence of moments and shear forces is not examined, since they would typically yield worse results than the deformation analogous to the previous section.

4.2.1 Square Plates - Analytical Solutions

For a sinusoidal load distribution, which vanishes at the edges of the plate, the solution to the boundary value problem of a simply supported rectangular plate is known explicitly (compare 4.5).

This load distribution is of minor practical interest, but any load distribution may be approximated by a double trigonometric series, which converges in the limit case to the desired load distribution. This result was first obtained by *Navier* [15] and is presented in a coordinate system with origin in the point $x = y = 0$ [17]:

$$p(\boldsymbol{x}) = \sum_{m=1}^{\infty} \sum_{n=1}^{\infty} a_{mn}\, sin\left(\frac{m\,\pi\,x}{l_x}\right)\, sin\left(\frac{n\,\pi\,y}{l_y}\right)$$
$$\text{with:} \quad a_{mn} \in \mathbb{R}\,, \quad 0 \leq x \leq l_x\,, \quad 0 \leq y \leq l_y$$

$$\Longrightarrow\; w = \frac{1}{\pi^4\,K} \sum_{m=1}^{\infty} \sum_{n=1}^{\infty} \frac{a_{mn}}{\left(\frac{m^2}{l_x^2} + \frac{n^2}{l_y^2}\right)^2}\, sin\left(\frac{m\,\pi\,x}{l_x}\right)\, sin\left(\frac{n\,\pi\,y}{l_y}\right) \tag{4.5}$$

The factors a_{mn} in the general solution for a pinned rectangular plate simplify in the case of uniform loading of magnitude p_0 to $a_{mn} = \frac{16\,p_0}{\pi^2\,m\,n}$. This solution transferred to a coordinate system with origin in the center of a square plate with side length l can also be written as:[17]

$$w_p = \frac{4\,p_0\,l^4}{\pi^5\,K} \sum_{m=1,3,5\ldots}^{\infty} \frac{-1^{\frac{m-1}{2}}}{m^5}\, cos\left(\frac{m\,\pi\,x}{l}\right)\, \left(1 - \frac{\alpha_m\, tanh(\alpha_m) + 2}{2\, cosh(\alpha_m)}\, cosh\left(\frac{m\,\pi\,y}{l}\right)\right.$$
$$\left. + \frac{\alpha_m\, y}{l\, cosh(\alpha_m)}\, sinh\left(\frac{m\,\pi\,y}{l}\right)\right) \quad , \quad \text{with:} \quad \alpha_m = \frac{m\,\pi}{2} \tag{4.6}$$

Both presented solutions converge fast but lead to numerical problems evaluating the expressions gained. In a solution with 200 terms considered the sum of the changes relative to the last increments by adding another term is $\approx 10^{-10}$ in the deflection.
The deformation of a clamped square plate under constant loading is constructed by superposition of the solution of a pinned square plate w_p given in equation 4.6 and two solutions w_m of square plates loaded by pairs of bending moments distributed along opposing edges. The necessary condition to determine the intensity of those moments, defined by coefficients C_m for $m = 1, 3, 5...$ is the zero normal derivative $w_{,n}$ on the boundary of the clamped plate, which yields the linear system of equations [17]:

$$\frac{C_m}{m}\left(tanh(\alpha_m) + \frac{\alpha_m}{cosh^2(\alpha_m)}\right) + \frac{8\,m}{\pi} \sum_{n=1,3,5\ldots}^{\infty} \frac{C_n}{n^3}\, \frac{1}{\left(1 + \frac{m^2}{n^2}\right)^2} \quad =$$

$$= \quad \frac{4\,p_0\,l^2}{\pi^3}\, \frac{1}{m^4}\left(\frac{\alpha_m}{cosh^2(\alpha_m)} - tanh(\alpha_m)\right) \tag{4.7}$$

Solving for a given number m as the maximum index in the sums gives the constants C_m. The two solutions w_m of a square plate loaded by pairs of moments acting on opposing edges with the plates flexural regidity K and α_m from equation 4.6 are obtained as [17]:

$$w_m = -\frac{l^2}{2\,\pi\,K} \sum_{m=1,3,5\ldots}^{\infty} C_m\, \frac{-1^{\frac{m-1}{2}}}{m^2\, cosh(\alpha_m)}\, cos\left(\beta_m\, x\right)$$

$$\left(\beta_m\, y\, sinh\left(\beta_m\, y\right) - \alpha_m\, tanh(\alpha_m)\, cosh\left(\beta_m\, y\right)\right) \qquad \text{with:} \quad \beta_m = \frac{m\,\pi}{l} \tag{4.8}$$

Finally the solution w_c of a clamped square plate is given as [17]:

$$w_c = w_p + 2\,w_m \tag{4.9}$$

The associated solution fields for the internal forces are computed using the relations given in equation 4.2, i.e. differentiating the expressions for w_p and w_c.

4.2.2 Mesh Construction

A rectangular mesh is constructed in a cartesian grid with $0 \leq x \leq l_x$ and $0 \leq y \leq l_y$. The node coordinates of the mesh are mapped by Φ_2:

$$\Phi_2 : \boldsymbol{x} \mapsto \tilde{\boldsymbol{x}}\,, \qquad \Phi_2(\boldsymbol{x}) := \begin{pmatrix} x + \frac{l_x}{10}\, sin\left(\frac{\pi\, x}{l_x}\right)\, sin\left(\frac{\pi\, y}{l_y}\right) \\ y + \frac{l_y}{10}\, sin\left(\frac{\pi\, x}{l_x}\right)\, sin\left(\frac{\pi\, y}{l_y}\right) \end{pmatrix} \tag{4.10}$$

This mapping gives back the same coordinates for points lying on the edges and ensures, that the element geometry is disturbed and not uniform in the mesh. Thereby, it shall be excluded that results are improved or disturbed due to a mesh regularity which, in general, can not be expected.
Additionally the whole domain is rotated by transforming the coordinates of the mesh via Φ_3, adding an angle $\Delta\varphi$ and transforming it back using Φ_3^{-1} [11]:

$$\Phi_3 : \boldsymbol{x} \mapsto \boldsymbol{r}\,, \qquad \Phi_3(\boldsymbol{x}) := \begin{pmatrix} r \\ \varphi \end{pmatrix} = \begin{pmatrix} \sqrt{x^2 + y^2} \\ arg(x + i\, y) \end{pmatrix} \tag{4.11}$$

$$\Phi_3^{-1} : \boldsymbol{r} \mapsto \boldsymbol{x}\,, \qquad \Phi_3^{-1}(\boldsymbol{r}) := \begin{pmatrix} x \\ y \end{pmatrix} = \begin{pmatrix} r\, cos(\varphi) \\ arg(x + i\, y) \end{pmatrix} \tag{4.12}$$

Therefore the coordinates $\tilde{\boldsymbol{x}}$ in the new mesh are obtained via:

$$\tilde{\boldsymbol{x}} = \Phi_3^{-1}\left(\Phi_3(\boldsymbol{x}) + \begin{pmatrix} 0 \\ \Delta\varphi \end{pmatrix}\right) \tag{4.13}$$

4.2.3 Clamped square plate

In the studies presented in this section the solution of a clamped plate with and without symmetry boundary conditions is investigated. Without symmetry boundary conditions all four edges of the plate are treated as clamped boundary partitions. The deflection w as well as the slope normal to the edge $w_{,n}$ is set to zero, i.e. $\partial\Omega = \Gamma = \Gamma_w = \Gamma_{w,n}$ as depicted in figure 4.10a.
Since the plate is double symmetric only one quarter of the plate may be meshed, but the focus lies on convergence rates, meaning that the same meshing routine, given in section 4.2.2, may be used. The boundary conditions for two adjacent edges are the same as for the clamped plate, but the other two adjacent edges are symmetry boundaries as imaged in figure 4.10b, i.e. the normal derivative $w_{,n}$ of the deflection on these edges and the effective shear force $\bar{q}_n$ is zero.
This study allows for a direct observation of the effects of the Kirchchoff effective shear force as a boundary condition in the presented approach. In fact the convergence studies show, that quadrilateral elements perform better or converge with the same convergence rate than triangular elements, being less sensitive to the applied boundary conditions. Using quadrilaterals in the context of methods 1 and 2 yield higher order convergence rates (see figure 4.11), but higher orders than $p = 5$ are not obtained. This is independent of boundary conditions in $\bar{q}_n$ and the use of an absolute error measure. Using quadrilateral elements and applying all boundary conditions via Lagrange multipliers enables convergence rates higher than $p = 5$ only for the symmetric case, but the orders $p = 3$ and $p = 5$ were found to converge with $\mathcal{O}(h^{p-1})$ (see figure 4.12a).
Using a triangulation to approximate the domain it is again observed, that convergence rates higher than $\mathcal{O}(h^5)$ are not reached with $p = 6$ being the highest order of triangular Lagrange elements used. Using any method presented yields said reduced convergence rates, if no symmetry boundary condition is applied (see figure 4.12b). Otherwise the maximum rate of convergence reduces drastically to $\mathcal{O}(h)$ for orders $p = 2$ and $p = 3$ and to $\mathcal{O}(h^2)$ for the higher orders used (see figure 4.13a) for

methods 1 and 2 and for method 3 the reduction is less predictive showing the expected behaviour for orders $p = 3$ and $p = 5$ and reduced convergence for all other ansatz orders (see figure 4.13b). Linear triangular elements are similar to the foregoing studies found to be non-convergent.

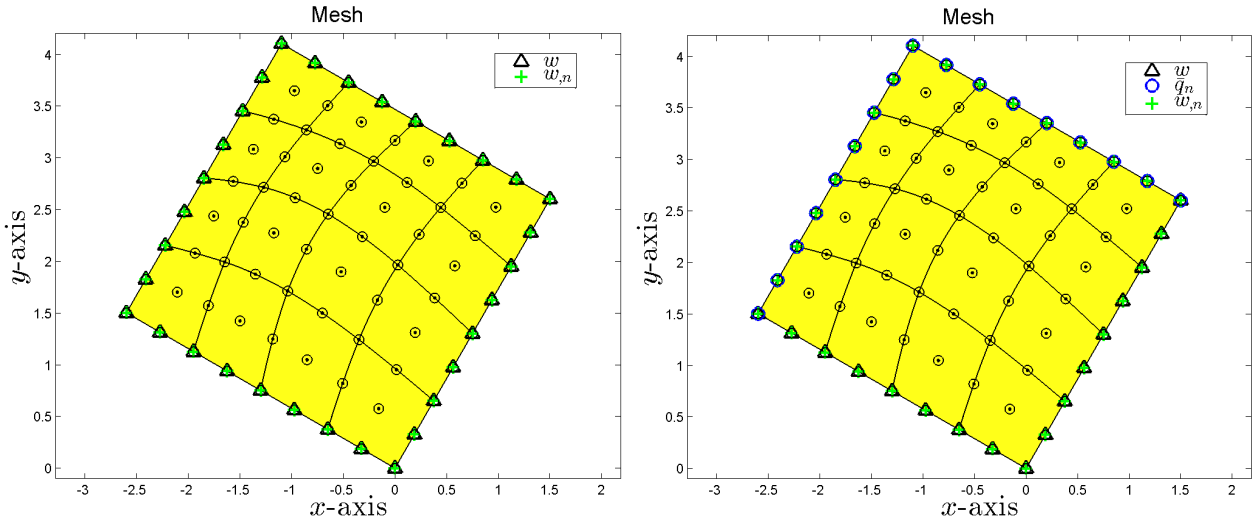

(a) Clamped plate **(b)** Clamped plate using symmetry BC

Fig. 4.10: Boundary conditions considered in the mapped rectangular mesh

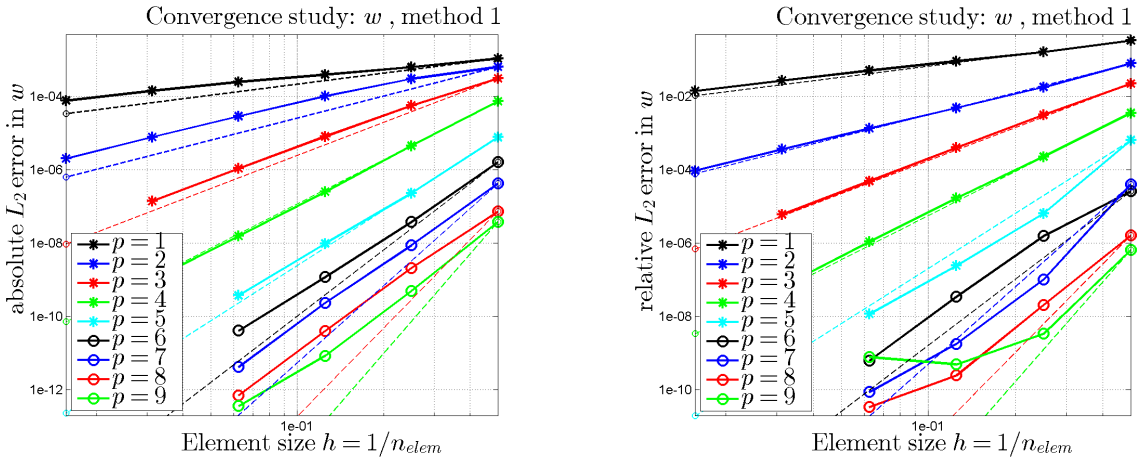

(a) Methods 1 and 2, no BC in $\bar{q}_n$ **(b)** Methods 1 and 2, with BC in $\bar{q}_n$

Fig. 4.11: Absolute (l.) and relative (r.) L_2 error in w using quadrilateral elements

In conclusion quadrilateral elements performed better than triangular elements, although an approximation with $\mathcal{O}(h^p)$ is in general not achieved for higher orders.
It is again mentioned that the analytical solution, presented as a series expression in 4.2.1, is evaluated using the same amount of terms in the sums for every study. The minimum relative L_2 error in w reached is $\approx 10^{-10}$ in the manufactured as well as in this solution and can be observed in the studies plotted (see figure 4.11b). In fact the remaining error in the approximation of the analytical solution depends on the field variable expressed as well as the coordinate system, since the terms involved in the analytical solution are evaluated with varying precision. To circumvent analytical solutions of mechanical problems obtained via methods using any kind of approximation or truncation, circular plates are considered in section 4.3.

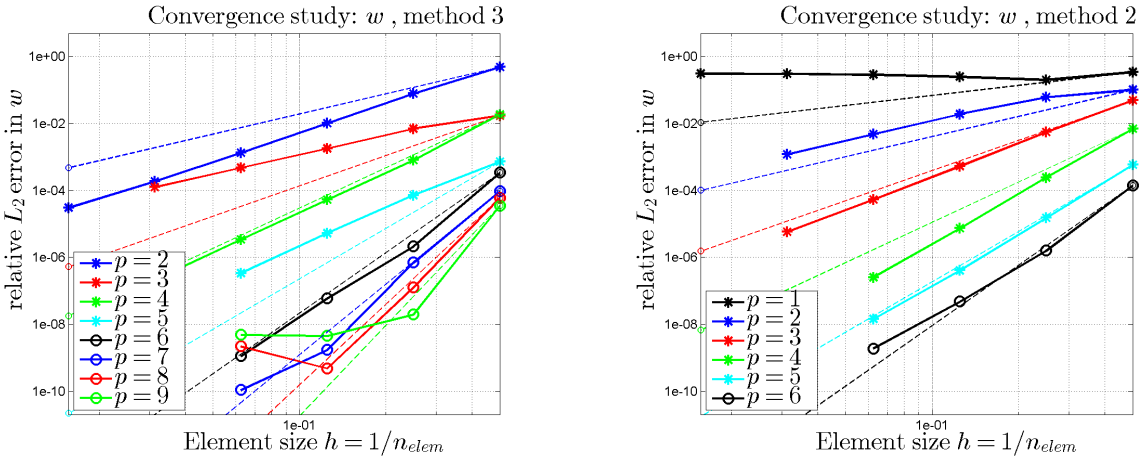

(a) Method 3, with BC in $\bar{q}_n$ **(b)** Methods 1,2 and 3, no BC in $\bar{q}_n$

Fig. 4.12: Convergence studies in w using quadrilateral (l.) and triangular (r.) elements

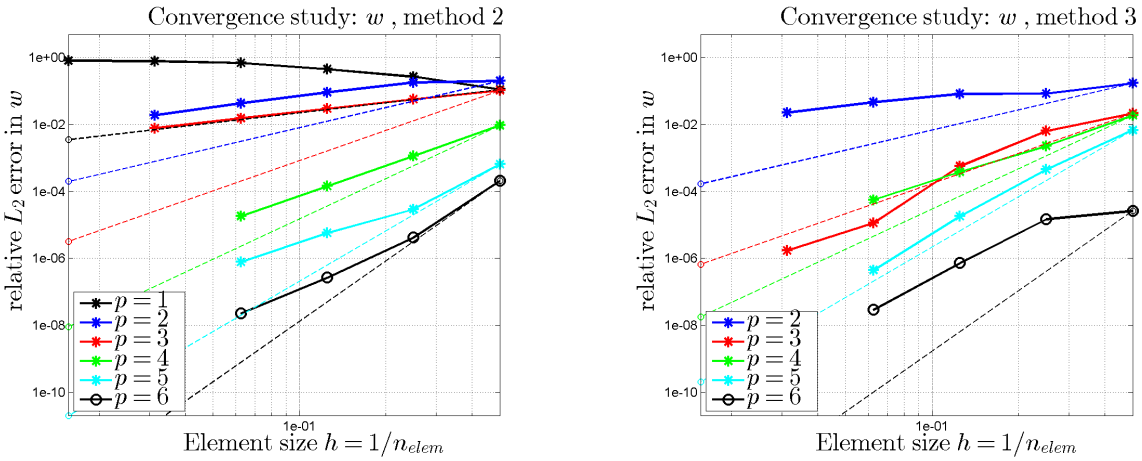

(a) Methods 1 and 2, with BC in $\bar{q}_n$ **(b)** Method 3, with BC in $\bar{q}_n$

Fig. 4.13: Convergence studies in w using triangular elements

Examining the absolute L_2 error distribution within the domain gives additional insight on the loss of accuracy. As can be seen from figure 4.14, errors in the corners of the domain are in general orders higher than in the center, although the solution w is zero. Along the edges within a small zone the error is also increased. Using a relative error measure in integration points near the boundary, thus having values of the deformation w tending to zero, would lead to a drastic increase of round-off errors involved in the error computation in that point. Therefore the absolute L_2 error is computed. Methods 1 and 2 feature wave patterns of increased accuracy within the domain for some constellations (see figure 4.14a), while the flickering colors in most of the L_2 error distributions indicate, that quadrilateral as well as triangular elements suffer from oscillations.
Comparing the distributions of the L_2 error resulting from approximations using symmetry boundary conditions with the corresponding ones without the effective shear force introduced, it can be seen that independent of element type or method used, the error does not have a kink or jump in corners, where the effective shear force is prescribed (see figure 4.15).
In all the corners of the clamped plate either the resulting corner force F_c or the deflection tend to zero, since the sum of twisting moment on the symmetry edge m_{nt} and shear force q_n at the supported corner tend to zero. Therefore the forces F_c , which in general arise at kinks on the boundary $\Gamma_{\bar{q}_n}$, are not the source of the reduced convergence.

Another point supporting this hypothesis is made comparing the error distribution of the clamped plate with the distribution observed when studying the manufactured solution (see figure 4.7b). For the manufactured solution the twisting moments and therefore forces F_c at the corners are non-zero, which leads to the conclusion, that the forces F_c do not hinder convergence.
Furthermore the absolute L_2 error distribution in figure 4.15b shows, that the error in the corner with two adjacent edges being clamped is in fact not always singular. Areas close to the corner and in the center of the domain give higher contributions to the overall absolute errors, while the other patterns observed of course remain.

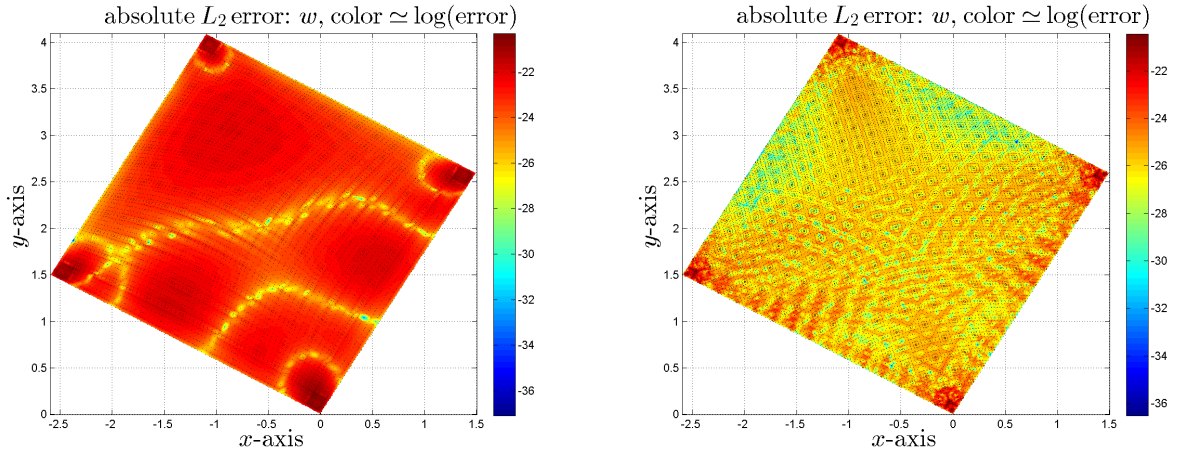

(a) Methods 1 and 2, quintic Quadrilaterals **(b)** Method 3, quintic triangles

Fig. 4.14: Absolute L_2 error distribution in the domain without symmetry BC

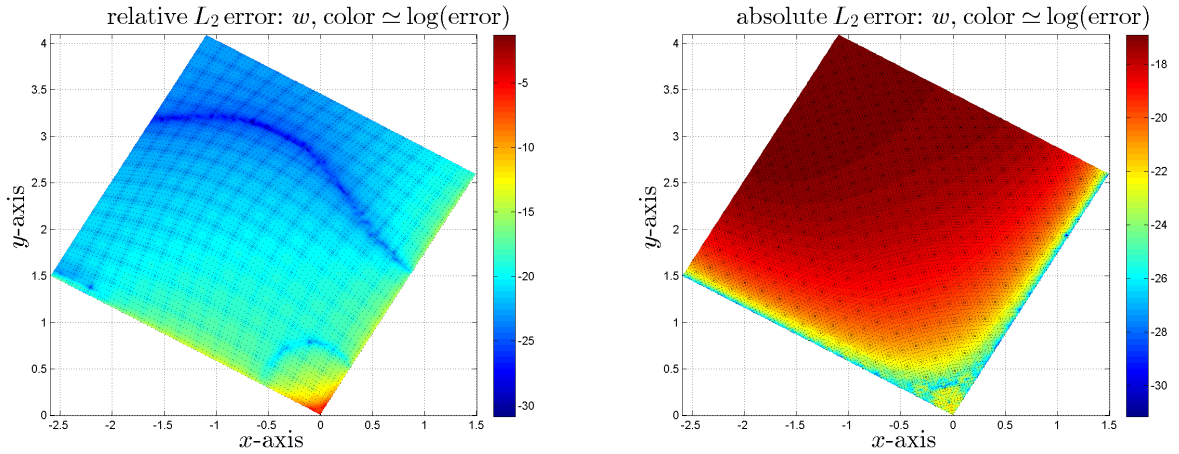

(a) Methods 1 and 2, quintic Quadrilaterals **(b)** Methods 1 and 2, quintic triangles

Fig. 4.15: Relative (l.) and absolute (r.) L_2 error distribution in the domain with symmetry BC

Additionally to the convergence curves of the deformation and the L_2 error distribution the condition numbers of the global stiffness matrix $\boldsymbol{K}_g$ are estimated during the study. It is observed, that the condition number in general grows with $\approx h^2$, neither depending on the method used, the element class considered nor on the enforcement of boundary conditions involving the effective shear force. In figure 4.16b a representative study using method 2 and symmetry boundary conditions is depicted. However, considering same decompositions method 1 yields significantly lower initial convergence numbers than method 2, which again gives significantly lower initial condition numbers than method 3, when Lagrange multipliers for the Neumann boundary conditions are used. The magnitude of the initial estimate of the condition number of $\boldsymbol{K}_g$ grows with symmetry boundary conditions used and

Lagrange multipliers defined. Moreover using method 1 without symmetry boundary conditions, the condition number estimate is found to grow with $\approx h$ (see figure 4.16a). The consistent growth of the estimate of the condition number of $\boldsymbol{K}_g$ does not indicate any issues, though the absolute numbers are in fact very high for the finest meshes considered. The numerical error in the load vector has strong influence, but is not worse compared to the previous study.
Approximating the solution of the Kirchhoff-Love boundary value problem for a clamped plate typical in mechanics with Dirichlet boundary conditions in w and Neumann boundary conditions in $w_{,n}$ and $\bar{q}_n$ higher order convergence rates are obtained. The effect of the Kirchhoff effective shear force applied as a boundary condition on the solution is strongly dependant on the method and element type used. The L_2 error distributions shown indicate, that the reduced convergence rates are an effect of small oscillations appearing using any of the methods presented, which grow in intensity, if no symmetry boundary condition is applied. Since the solution is extremely sensitive to boundary conditions in the field of the deformation w, the Lagrange multipliers λ_w approximating the boundary condition may be too inaccurate to enable higher convergence rates than $\approx \mathcal{O}(h^6)$.
In the next section the pinned square plate is examined to verify the results obtained for the clamped plate.

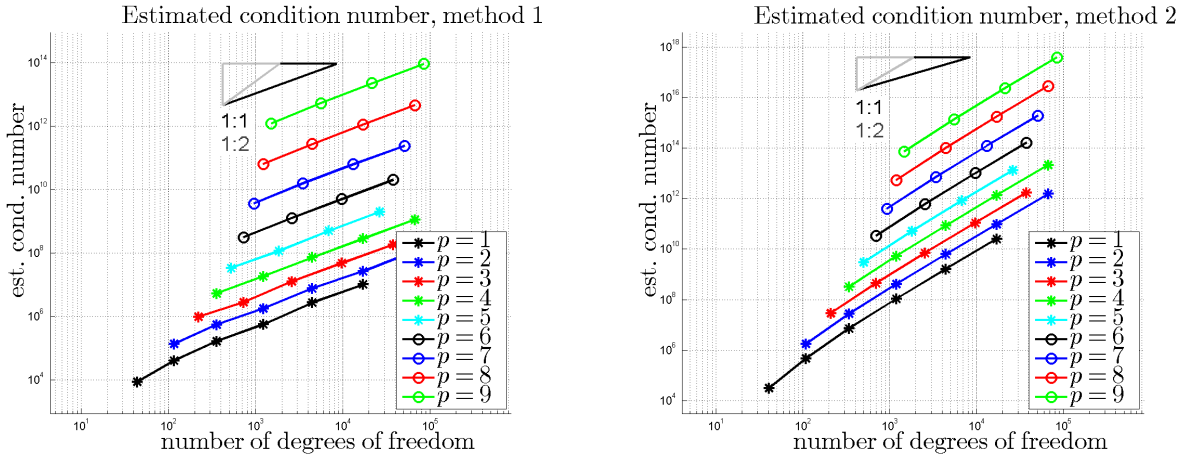

(a) Method 1, no BC in $\bar{q}_n$

(b) Methods 1, 2 and 3, all other combinations

Fig. 4.16: Estimates of the condition number of the global stiffness matrix $\boldsymbol{K}_g$

4.2.4 Pinned square plate

Similar to the clamped square plate the pinned square plate is investigated with and without symmetry boundary conditions. Therefore the simple pinned square plate is approximated enforcing homogeneous boundary conditions in the deflection w and the bending moment m_n normal to the edge on the whole boundary of the domain, i.e. $\partial\Omega = \Gamma_w = \Gamma_{m_n}$. Introducing symmetry boundary conditions on two adjacent edges is done as described in section 2.6.5 by prescribing values for the normal slope to a boundary $w_{,n}$ on $\Gamma_{w,n}$ and the effective shear force $\bar{q}_n$ on $\Gamma_{\bar{q}_n}$. The boundary conditions indicated by markers in the nodes on the boundary of the mesh for both cases are depicted in figure 4.17.

Again this setting allows for a direct observation of the effects of the Kirchhoff effective shear force on the quality of the approximation. Using the point collocation method to enforce boundary conditions yields a maximum convergence rate of $\mathcal{O}(h^2)$ for all orders p used, when no boundary condition in $\bar{q}_n$ is enforced. Introducing symmetry boundaries reduces convergence of orders $p = 3$ and higher for quadrilaterals (see figure 4.18a), while triangular elements analogously to the clamped plate are found to be more sensible to this boundary condition. The convergence of the absolute L_2 error in

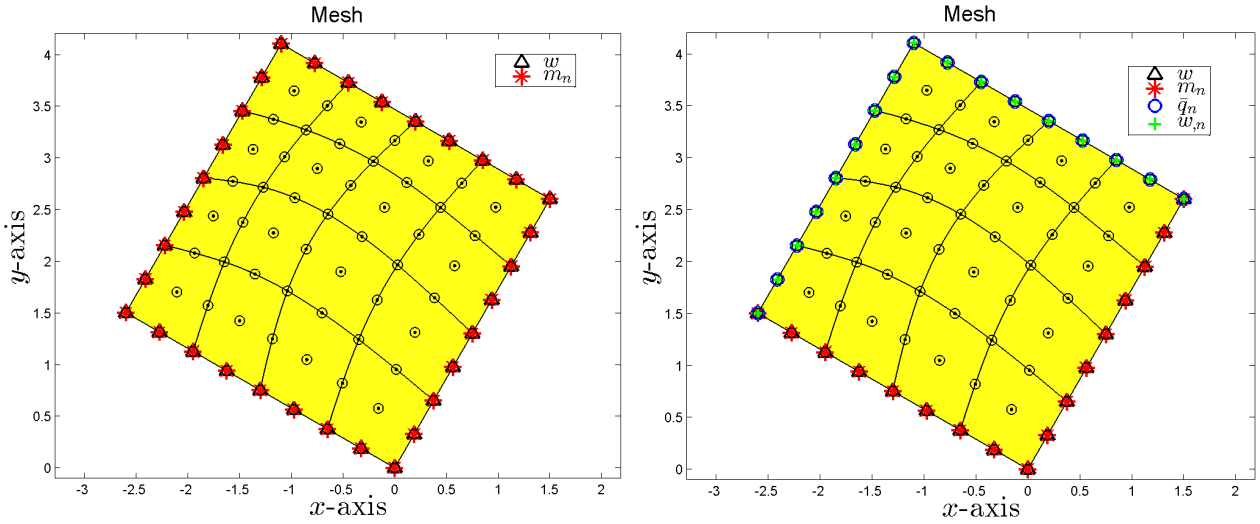

(a) Pinned plate **(b)** Pinned plate using symmetry

Fig. 4.17: Boundary conditions considered in the mapped rectangular mesh

m_n on the boundary Γ_{m_n} is sub-linear with $\approx \mathcal{O}(h^{0.5})$ and therefore not presented.
Utilising method 2 it is observed, that all reach the expected convergence rates $\mathcal{O}(h^p)$ if quadrilaterals or no symmetry boundary condition is used. The studies obtained are similar to those corresponding to the clamped plate and therefore only one study corresponding to method 2 with symmetry boundary conditions is shown in figure 4.18b, wherein it is observed, that introducing symmetry boundary conditions is also beneficial in some constellations. The absolute L_2 error in m_n on the boundary Γ_{m_n} is approximated with $\approx \mathcal{O}(h^{p+2})$ for the first orders using quadrilaterals (see figure 4.19a) and with $\approx \mathcal{O}(h^4)$ for higher orders and with $\approx \mathcal{O}(h^p)$ using triangular elements.
Method 3 yields similar results to method 2, but also shows effects similar to the ones occurring in the studies of the clamped plate, i.e. being less predictive for symmetry boundary conditions or triangular elements on the one side, but also yielding the best results in other constellations.

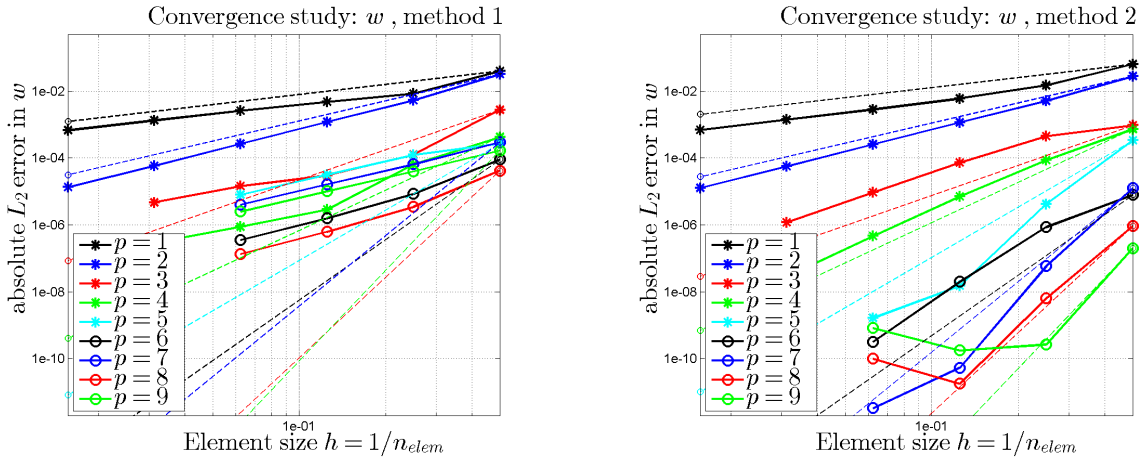

(a) Method 1, with BC in $\bar{q}_n$ **(b)** Method 2, with BC in $\bar{q}_n$

Fig. 4.18: Convergence studies in w using quadrilateral elements

The L_2 error distribution in the domain shows, that oscillations are present again. Being minor for quadrilateral elements in the study of the clamped plate, similar effects are in the case of the pinned plate much more distinctive. For the pinned plate with no symmetry boundary condition the solutions obtained via methods 2 and 3 feature oscillations, which vanish with the introduction of

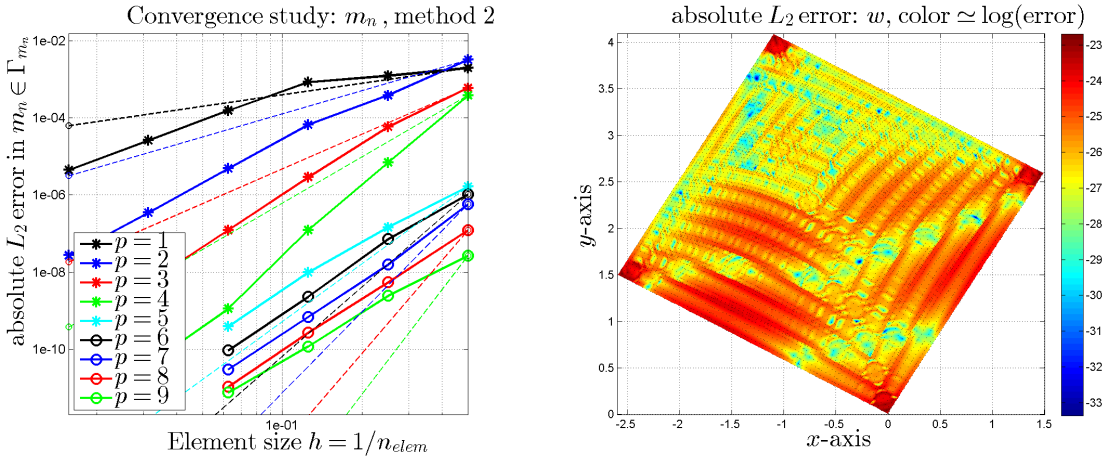

(a) Methods 2 and 3, with BC in $\bar{q}_n$ **(b)** Methods 2 and 3, without BC in $\bar{q}_n$

Fig. 4.19: Convergence study in m_n and L_2 error distribution, independent of element type

symmetry boundaries (compare figures 4.19b and 4.20b). Using method 1, which yields the worst results, the boundary conditions are not applied properly, indicated by high absolute L_2 errors and incorrect behaviour in the regions around the corner (see figure 4.20a). The high error in the corners is introduced via averaging the unit outward normal with the areas of the coinciding elements, which is the best possible result obtained for arbitrary geometries. The maximum convergence rate of the L_2 error in w is $\approx \mathcal{O}(h^2)$.

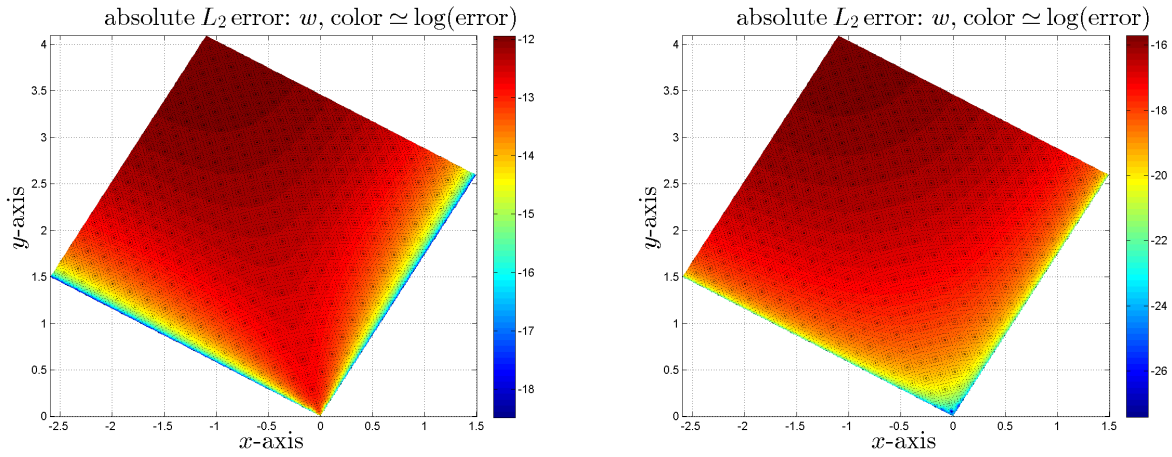

(a) Method 1, incorrect behaviour in the corner **(b)** Methods 2 and 3, correct behaviour in the corner

Fig. 4.20: L_2 error distribution with symmetry BC, independent of element type

The estimated condition number of the global stiffness matrix $\boldsymbol{K}_g$ grows, similar to the clamped plate problem, with $\mathcal{O}(h^2)$ for all cases but method 1 using no symmetry boundary conditions. This is of no advantage, since the bending moment in the corners is prescribed inaccurately.
For the pinned square plate higher order convergence rates are reached using methods 2 and 3 with quadrilaterals or without symmetry boundary conditions. The L_2 error distributions indicate, that using only pinned boundaries increases accuracy, but also introduces oscillations.
Method 1 is not able to enforce the boundary conditions in m_n correctly which is in this particular case of right angles resulting in the maximum error. The errors are high but distributed smoothly. Comparing with the manufactured solution, which yielded the expected $\mathrm{O}(h^p)$ convergence rates and also featured corners with almost right angles, it is concluded, that the errors induced by the corners are not the main reason for the reduced convergence but the error in the domain as a consequence

of the incorrect enforcement along the boundaries.
The studies of the square plate again indicated, that the introduction of the effective shear force $\bar{q}_n$ does not *per se* hinder higher order convergence rates, but quadrilaterals were found to be more robust than triangular elements.
For all the presented methods the treatment of kinks in the boundary of the domain is found to be of utmost importance. The twisting moment m_{nt} along the boundary of pinned or clamped square plates is in general non-zero, but the deflection vanishes on the boundary. Therefore statements concerning the contributions of the forces concentrated in the corners F_c to the deflection of the plate do not play a role.
The further investigation of L_2 error distributions revealed, that all of the methods presented suffer from oscillations using lower order elements. This was already observed in the case of linear triangles, which were non-convergent for any mesh refinement. Using higher order elements reduces the effect in general. The L_2 error distributions in the figures presented show, that the three methods are of different sensitivity concerning the oscillations.
However the approximate solution due to Navier, which includes sums of trigonometric expressions, is troublesome. Therefore the square plate with sinusoidal load distribution was studied (see figure 4.21), showing results similar to the manufactured solution. Oscillations occurred for all three methods independent of symmetry boundary conditions and element type. Super convergent behaviour of all primary field variables was observed up to the minimum error for all orders using methods 2 and 3, no symmetry boundary conditions, quadrilateral elements and an undistorted rectangular mesh (see figure 4.21a). The node distortion within the mesh already reduces the $\mathcal{O}(h^{p+1})$ convergence rate to the expected level for orders higher than $p = 1$ (see figure 4.21b), applying symmetry boundary conditions adds in the effects described in this section. Method 1 showed the same behaviour as the pinned plate with constant loading, i.e. reduced convergence for all orders p. In conclusion, the small oscillations are significantly reduced with h and p refinement except for linear triangles.

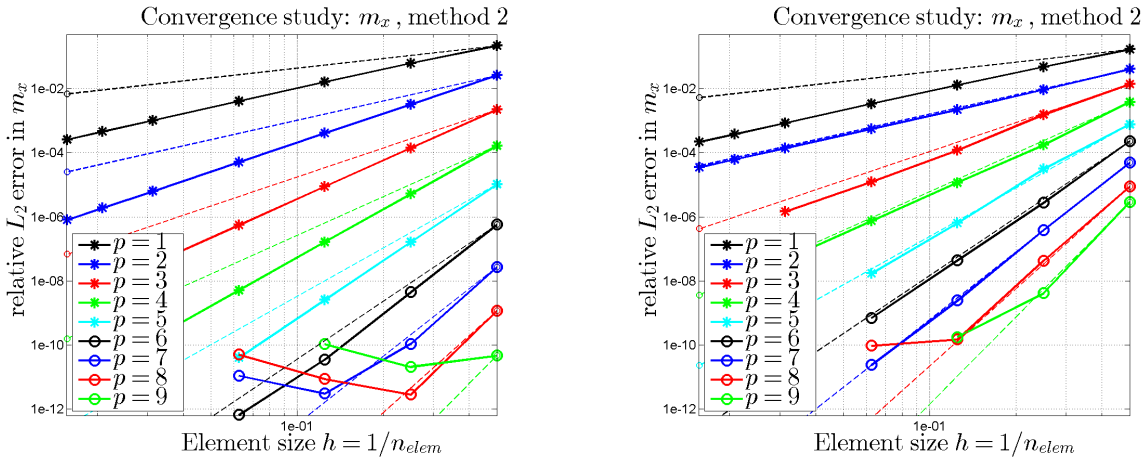

(a) Uniform mesh, elements of same size

(b) Distorted inner mesh nodes via Φ_2

Fig. 4.21: Sinusoidal load distribution: m_x, methods 2 and 3, no symmetry BC, quadrilaterals

Revisiting the L_2 error distribution for the manufactured solution in figure 4.7b one can see, that small oscillations are present. The reason for the oscillations not dominating the error remains unknown, since both relative and absolute error measures were used giving equivalent results. The factor c_g in the mapping Φ_1 is set to $c_g = 0$ resulting in a square mesh (figure 4.22a). Comparing the relative L_2 errors using method 2 and 50×50 quadratic triangular elements identical color-scaling reveals, that the initial relative L_2 error for the unrotated square plate shows the same oscillation patterns. Therefore the approximative character of the Navier solution is not the reason for the patterns observed in the L_2 error distributions. The study of the manufactured solution on the square domain yielded optimal convergence rates. The routines used are exactly the same and studies of the pinned

square plate in a not rotated mesh still give same results as the rotated mesh. Possible reason remaining is solely, that the solution itself influences the convergence behaviour in an unexpected way (since it is smooth in Ω and not singular). The approximative solution considered as a reference solution is not exact, though the error involved is for a constant number of terms in the sum the same, which would not trigger different behaviour of the methods considered and the convergence curves would stagnate at a certain level.

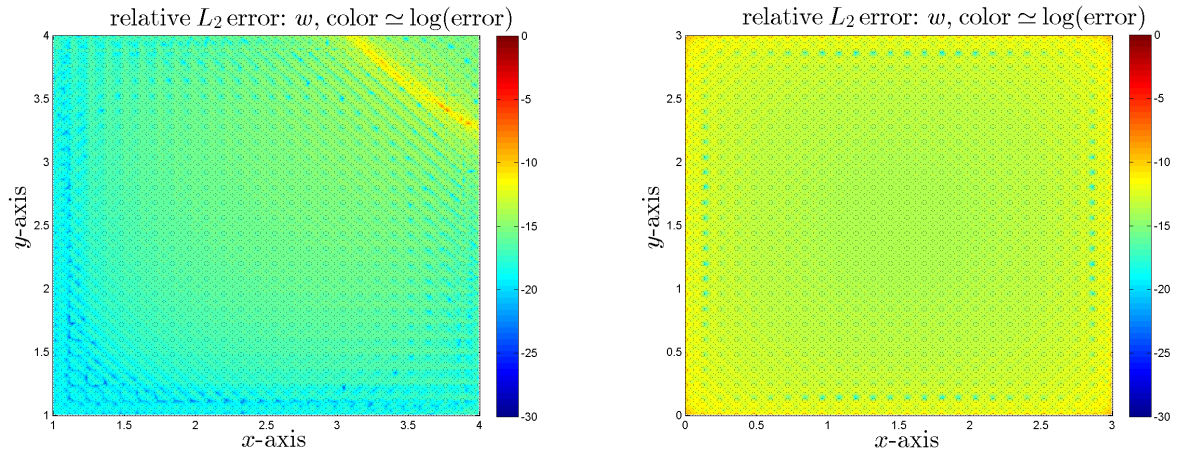

(a) Manufactured solution, $c_g = 0$ **(b)** Unrotated square mesh

Fig. 4.22: Oscillations in the meshes, method 2, all boundaries pinned, 50×50 quadratic triangular elements

The geometry of the square domain considered is exactly represented for any polynomial order p of the Lagrange shape functions chosen. To further examine the behaviour of the presented mixed Finite Element formulations considering real mechanical problems and to investigate the influence of approximating the domain Ω circular plates are considered next.

4.3 Circular Plates with Various Boundary Conditions

Within this section the convergence and distribution of the L_2 error of the solutions obtained via mixed finite element formulations is examined. The geometry of the square plate is therein only approximated using the shape functions. Enforcing boundary conditions using the three presented methods on the geometry description and applying the Kirchhhoff effective shear force along the symmetry axes as a boundary condition is the main focus of the following elaborations.

4.3.1 Circular Plates - Analytical Solutions

The analytical solutions of the deformations of clamped and pinned circular plates with radius R and bending stiffness K under constant loading p_0, transformed via $\Phi_3^{-1}(\boldsymbol{r}) : \boldsymbol{r} \mapsto \boldsymbol{x}$, are [17]:

$$\text{clamped:} \qquad w_{cc} = \frac{p_0}{64\,K}\left(R^2 - r^2\right)^2 \overset{\Phi_3^{-1}}{=} \frac{p_0}{64\,K}\left(R^2 - x^2 - y^2\right)^2 \tag{4.14}$$

$$\text{pinned:} \qquad w_{pc} = \frac{p_0}{64\,K}\left(R^2 - r^2\right)\left(\frac{5+\nu}{1+\nu}R^2 - r^2\right) \quad =$$

$$\overset{\Phi_3^{-1}}{=} \frac{p_0}{64\,K}\left(R^2 - x^2 - y^2\right)\left(\frac{5+\nu}{1+\nu}R^2 - x^2 - y^2\right) \tag{4.15}$$

The solutions presented are symmetric with respect to the center of the plate and are not obtained involving any approximations or truncations.

4.3.2 Mesh Construction

The domain of a circular plate is constructed via manipulation of a polygon with corners lying on the boundary of the disk. The nodes on the edges on the boundary of the domain do not lie on the circle describing the boundary. In order to reach higher order convergence the edge-nodes of higher order elements need to lie on the boundary.
As a first approach the nodes on the boundary of the domain were forced onto the circle solving the corresponding Dirichlet boundary value problem of linear elasticity with plane strain assumption on the polygon [2]:

$$\begin{cases} \text{find } u_x \text{ and } u_y \text{ in } \Omega, \text{ such that} \\ \\ u_{x,xx} + \frac{1-\nu}{2}\, u_{x,yy} + \frac{1+\nu}{2}\, u_{y,xy} &= 0 \quad \text{in } \Omega \subset \mathbb{R}^2\,, \\ u_{y,yy} + \frac{1-\nu}{2}\, u_{y,xx} + \frac{1+\nu}{2}\, u_{x,xy} &= 0 \quad \text{in } \Omega \subset \mathbb{R}^2\,, \\ u_x &= \hat{u}_x \quad \text{on } \Gamma = \partial\Omega\,, \\ u_y &= \hat{u}_y \quad \text{on } \Gamma = \partial\Omega\,. \end{cases} \tag{4.16}$$

Therein u_x and u_y are the nodal displacement degrees of freedom and ν is Poisson's ratio. As depicted in figure 4.23a, the nodes in the resulting mesh are shifted smoothly and a circular mesh with all nodes on the boundary being on a circle remain.
The second approach taken is to apply a transfinite mapping algorithm by *Šolin et al.* [16], to map the points of the elements on the boundary onto the circle. The outcome is a mesh with elements on the boundary, that have one curved edge, as can be seen in figure 4.23b. Elements within the domain are not adapted.

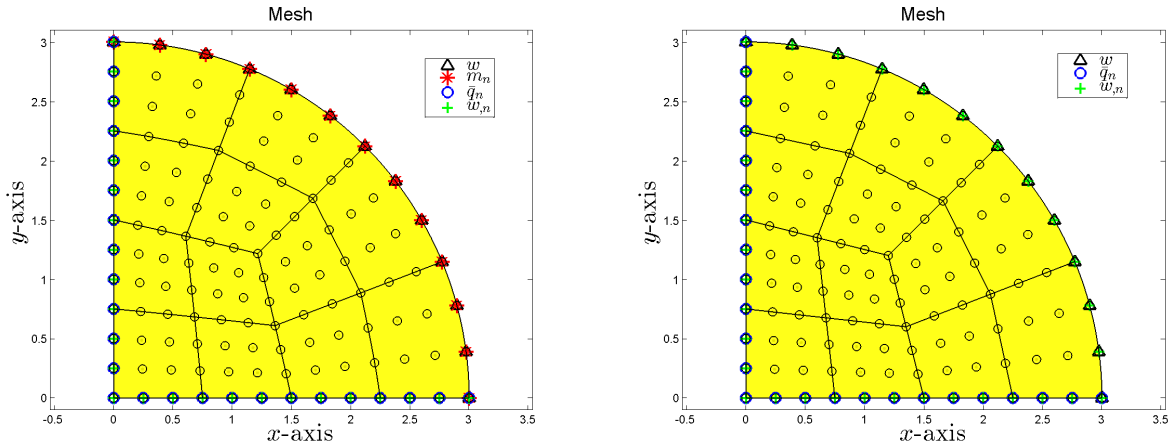

(a) Mesh constructed via solving linear elasticity **(b)** Mesh constructed using transfinite mappings

Fig. 4.23: Circular mesh with the boundary conditions used, symmetry applied

The mesh generation procedure solving linear elasticity in $\mathbb{R}^2$ is especially for large problems cumbersome, but easily implemented, if the needed finite element code is available. The second approach is based on element-local mappings and is therefore not associated with as much computational effort as the first mesh generation. Both topics are not covered within this thesis, the interested reader is

referred to *Bathe* [4] and *Šolin et al.*[16].
In the following circular Kirchhoff-Love plates are studied. The Kirchhoff effective shear force as well as the slope normal to the boundary is prescribed at symmetry boundaries and the effects are examined.

4.3.3 Circular Plate - Mesh obtained via Linear Elasticity in $\mathbb{R}^2$

The convergence studies of the circular plate with pinned or clamped boundaries without symmetry boundary conditions show convergence with $\mathcal{O}(h^p)$ or $\mathcal{O}(h^{p+1})$ for lower order elements depending on the method and element used, but the expected convergence rates for shape functions of order $p = 4$ or higher are never reached (see figure 4.24a). To indentify the reason for this behaviour the efforts described in the following are made.
The estimate of the convergence number of the global stiffness matrix $\boldsymbol{K}_g$ is growing with $\approx \mathcal{O}(h^2)$ similar to plates already considered and is therefore not presented again. The manufactured solution is utilized on the circular mesh and convergence studies are completed. These showed the same reduced convergence rates as clamped and pinned plates, but smaller initial errors (see figure 4.24b).

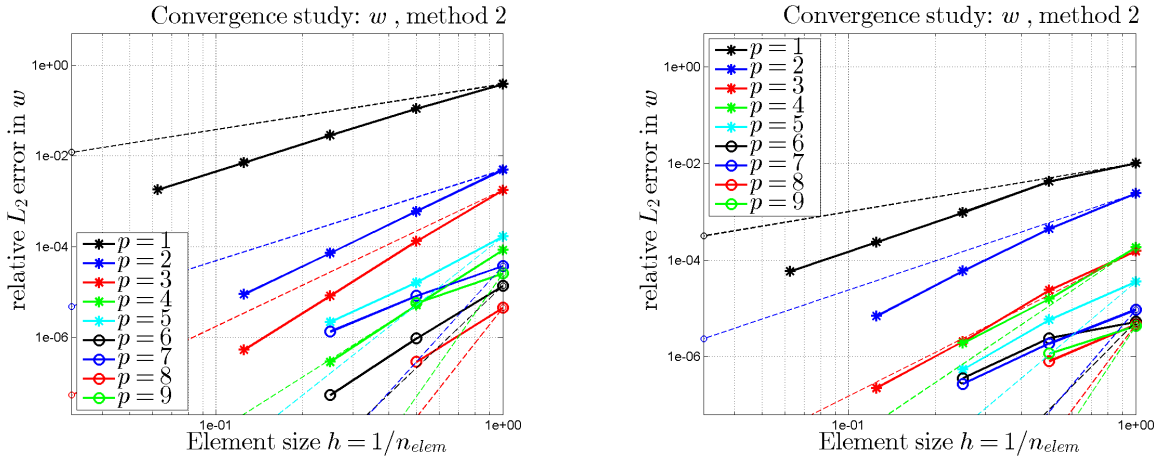

(a) Pinned circular plate **(b)** Manufactured solution

Fig. 4.24: Circular mesh without symmetry BC, prescribing $\hat{w}$ and $\hat{m}_n$ on $\partial\Omega$

From the convergence curve of the bending moment m_n it is concluded, that the boundary conditions are not enforced properly using any of the presented methods for any homogeneous or inhomogeneous boundary conditions applied, resulting in curves similar to those in figure 4.25a.
The absolute L_2 error distribution in w is depicted in figure 4.25b and shows oscillations in the bending moment m_x. The symmetry boundary conditions do not enhance the oscillations, which are clearly visible only in the internal moment fields. As already pointed out, the occuring oscillations do not *per se* hinder higher order convergence. The oscillations vanish under h and p refinement.

The area of the circle is approximated with convergence orders of $\mathcal{O}(h^{p+1})$, as can be seen in figure 4.26a, and the manufactured solution on the polygonal domain, which was used to construct the mesh, yields the expected convergence rates using the same boundary conditions (see figure 4.26b). From the successful integration in the circular mesh and the optimal convergence on the polygonal domain it is concluded, that the mesh construction procedure is of minor quality.

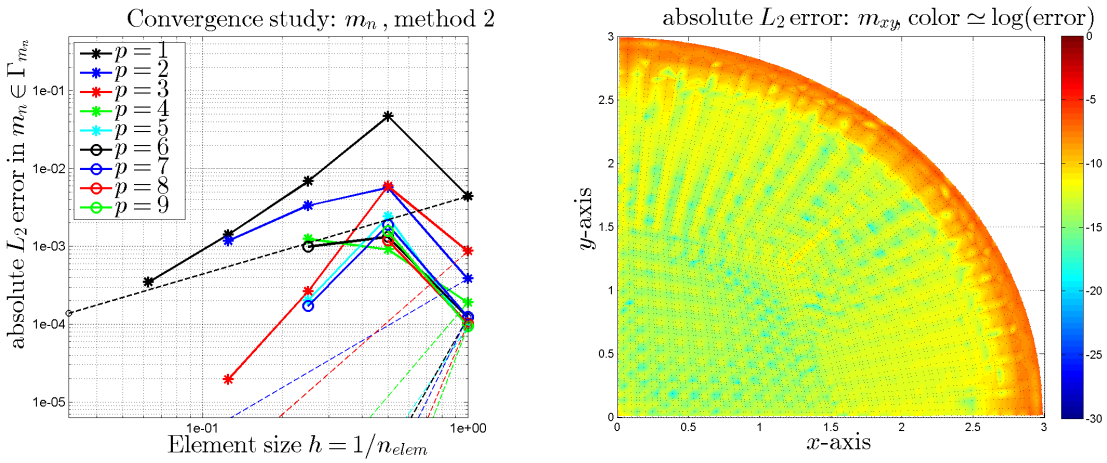

(a) Pinned plate without symmetry BC

(b) Quarter of a pinned plate

Fig. 4.25: Absolute L_2 errors in circular mesh, BC in $\hat{w}$ and $\hat{m}_n$ on $\partial\Omega$

The testing of the mesh properties is completed by prescribing boundary conditions in every primary field variable, i.e. w, m_x, m_y and m_{xy}, in every node of the mesh. The resulting convergence study is similar to 4.24a and hence indicates, that the interpolation error is dominating the approximation error and also the reason for the improper convergence rates. The same result may be obtained using the Kronecker Delta property of the Lagrange Elements, yielding a global stiffness matrix $\boldsymbol{K}_g$ equal to the second order isotropic tensor $\boldsymbol{I}$, or by simply interpolating the known solution in the domain directly.

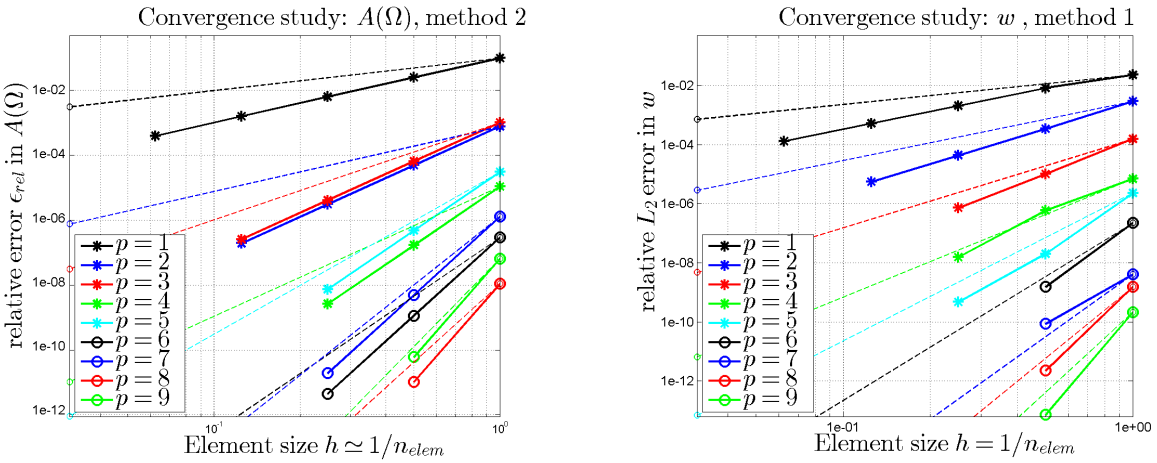

(a) Converging area $A(\Omega)$ of the circular mesh constructed via solving linear elasticity

(b) Manufactured solution on polygonal domain from which the circular mesh was constructed

Fig. 4.26: Convergence studies using quadratic elements

In conclusion the manipulation of the polygonal mesh by solving a Dirichlet boundary value problem for linear elasticity with plane strain assumption yields a mesh which is not able to provide optimal convergence rates for an ansatz of polynomial order $p = 4$ or higher. The determinant of the Jacobi matrix evaluated at the nodes that were originally on the circle and are forced to stay exactly on the circle reaches nearly singular values, as can be seen in figure 4.27a. Increasing the polynomial order of the shape functions simultaneously increases the pointedness of the cusps observed.
For comparison the determinant of the Jacobi matrix in the domain resulting from the second approach involving transfinite mappings is depicted in figure 4.27b. It is observed that the points on the boundary do not feature nearly singular values.

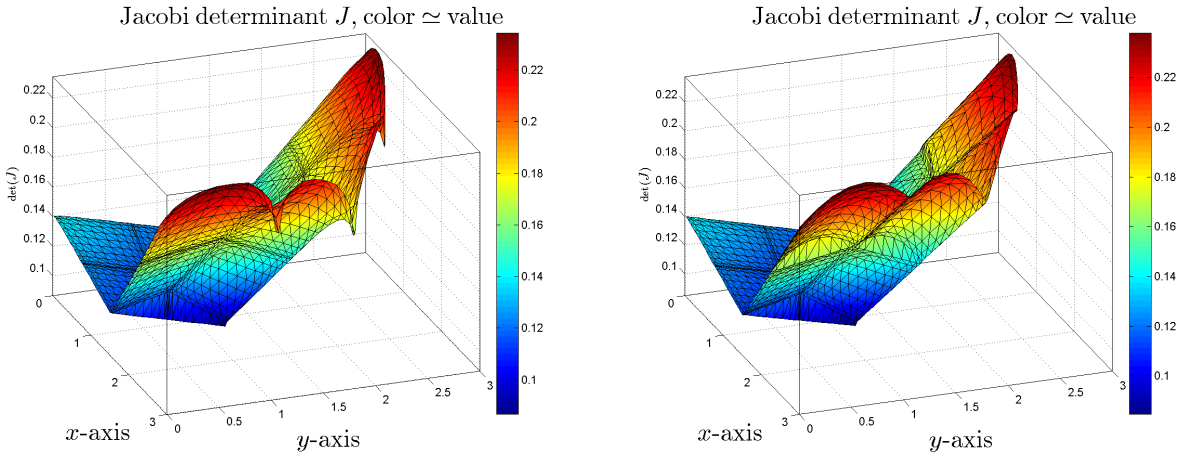

(a) Mesh constructed via solving linear elasticity **(b)** Mesh constructed using transfinite mappings

Fig. 4.27: Determinant of the Jacobi matrix evaluated in a quarter of the mesh, quadrilateral elements of order $p = 9$

4.3.4 Circular Plate - Mesh obtained via Transfinite Mapping

Clamped boundary conditions

The transfinite mapping applied to the polygonal domain to approximate the geometry of a circle enabled the completion of convergence studies with success. Similar to the studies concerning the manufactured solution convergence orders of $\mathcal{O}(h^p)$ were reached. Surprisingly the orders $p = 1$ to 3 were found to behave differently than higher orders. In the following all methods showed equivalent convergence behaviour if not mentioned otherwise.
The introduction of the Kirchhoff effective shear force as a boundary condition did only influence the convergence behaviour of the orders $p = 1$ to 3 using quadrilateral elements, as can be seen in figure 4.28. The internal moments are approximated with accuracy loss of one order for $p \leq 3$ and with $\mathcal{O}(h^p)$ for higher orders (see figure 4.29a).
Triangular elements are more sensitive to symmetry boundary conditions and similarly to quadrilaterals polynomial orders of $p = 4$ or higher were found to show expected behaviour or even superconvergence. The internal moments are approximated with an accuracy loss of half an order (see figure 4.29b).

The absolute L_2 error in the domain is examined and similar patterns were observed for all methods presented. The distribution of the error does not differ whether symmetry boundary conditions are enforced or not. In the deformation field no oscillations were found using a mesh of 300 quadrilateral or 600 triangular cubic finite elements per quarter of the circular plate, whereas the internal moment fields featured patterns similar to those observed in the previous studies (see figure 4.30). Prescribing the slope normal to the boundary $w_{,n}$ resulted in arc-shaped zones of enhanced accuracy in the internal moment fields similar to the ones observed in the deflection field of the rectangular plate (see figure 4.15a).

Symmetry boundary conditions on the circular clamped plate are successfully enforced yielding higher order convergence rates. The pinned circular plate remains to be studied.

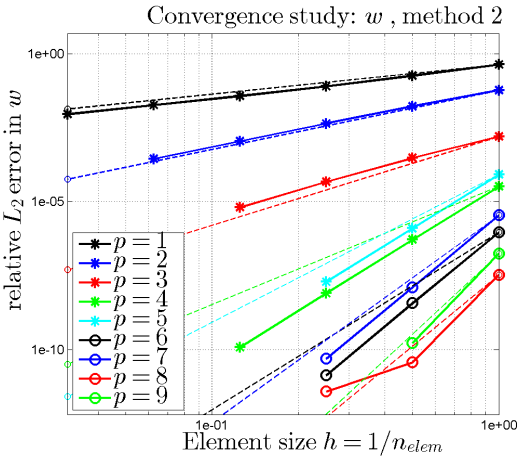

(a) Methods 1 to 3, without BC in $\bar{q}_n$

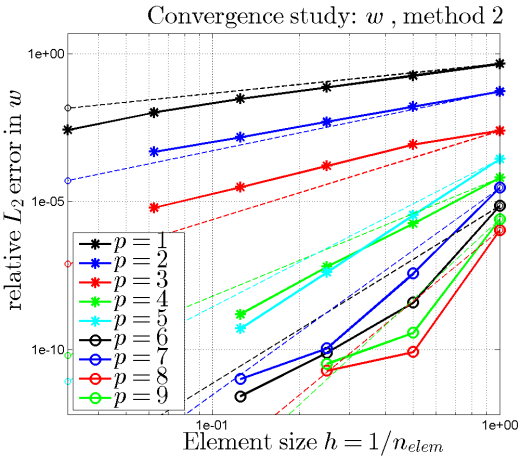

(b) Methods 1 to 3, with BC in $\bar{q}_n$

Fig. 4.28: Convergence studies in w using quadrilateral elements

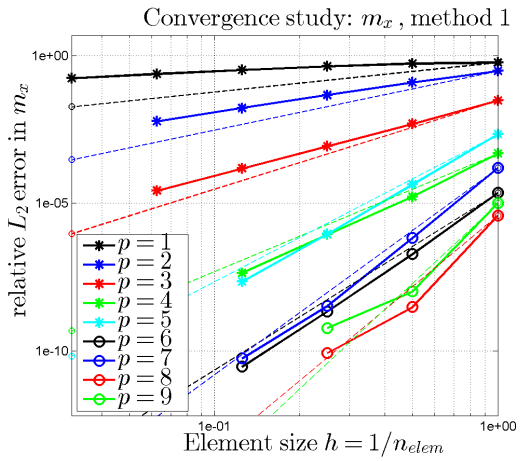

(a) Methods 1 and 2, with BC in $\bar{q}_n$

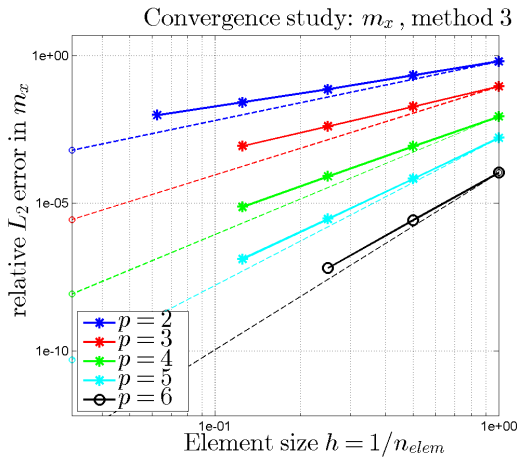

(b) Method 3, with BC in $\bar{q}_n$

Fig. 4.29: Convergence studies in m_x using quadrilateral (l.) and triangular elements (r.) elements

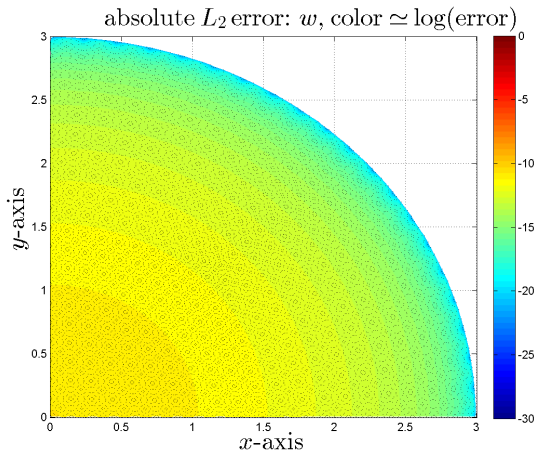

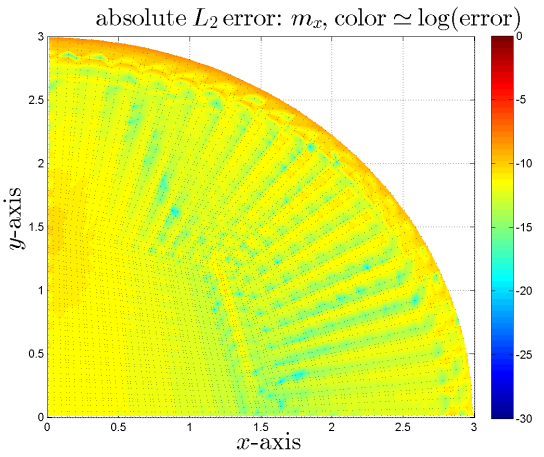

Fig. 4.30: Distribution of the absolute L_2 error in w (l.) and m_x (r.), independent of element and method used

Pinned boundary conditions

The convergence studies of the circular plate show widely similar results to those obtained for the clamped circular plate. It is mentioned, that in the limit case the approximated circular plate without symmetry boundary conditions has no kink in the boundary. Additionally the bending moment m_n is not prescribed on symmetry boundaries, hence method 1 does not suffer from a major loss of accuracy as faced in the case of square plates. The results obtained via methods 1 and 2 are identical or equivalent for the most part.
The orders $p = 1$ to 3 again showed worse convergence behaviour compared to the orders $p = 4$ and higher. Without symmetry boundary conditions convergence rates of $\mathcal{O}_h^{p+1}$ are reached for $p \geq 4$ in w, similar to 4.28a.
Contrary to the studies of the clamped circular plate the quadrilateral elements were found to be as sensitive as triangular elements to the symmetry boundary condition introduced and feature kinks for some orders, as can be seen in figure 4.31.

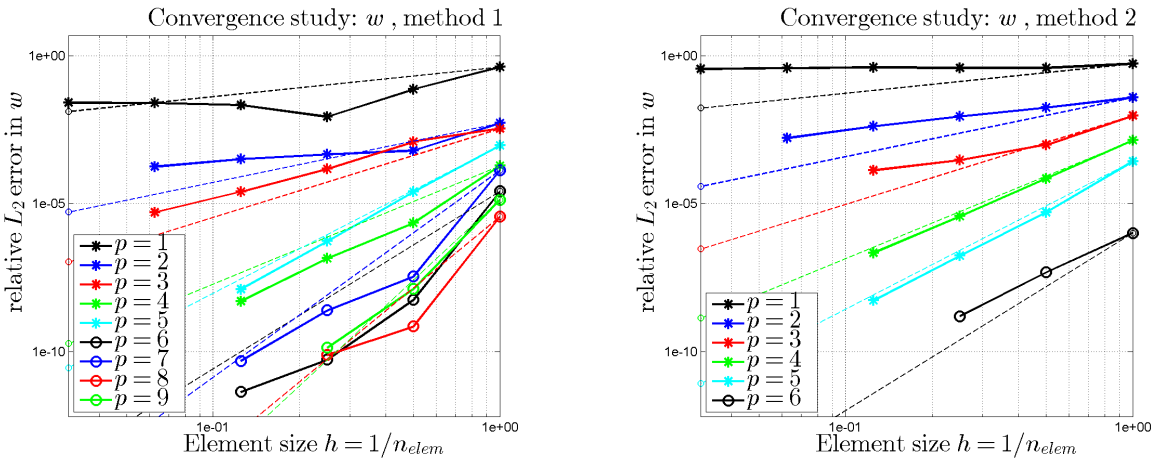

(a) Methods 1 and 2, with BC in $\bar{q}_n$ **(b)** Method 1 and 2, with BC in $\bar{q}_n$

Fig. 4.31: Convergence studies in w using quadrilateral (l.) and triangular (r.) elements

Method 3 with symmetry boundary conditions introduced using quadrilateral or triangular elements showed super-convergent behaviour, approximating the solution better than without symmetry boundary conditions, as can be seen in figure 4.32. This case is considered to be a result of the combination of the regularity of the mesh and the solution, though method 3 yields mostly the best results with effective shear forces as boundary conditions.

The internal bending moments converge with the same or slightly reduced convergence orders compared to the deformation, as depicted in figure 4.33.

The absolute L_2 error distributions are calculated and show the same patterns as the ones presented in 4.30 corresponding to the clamped circular plate, i.e. no oscillations in the deformation field visible, but in the internal moment fields.
The examinations of the circular plate demonstrated the importance of a proper domain decomposition. While the mesh constructed via solving linear elasticity in $\mathbb{R}^2$ and thus forcing the nodes on the boundary yielded a mesh of minor quality, the application of transfinite mappings was successful. The impact on the approximation quality of applying symmetry boundary conditions depends on the boundary data on the other boundaries, how boundary conditions are enforced in general, the choice of element and lastly the order. For a wide variety of constellations the expected convergence rates of $\mathcal{O}(h^p)$ were reached. Certain constellations combined with a regular mesh enabled rates of $\mathcal{O}(h^{p+1})$ or even more. This concludes the numerical examples considered.

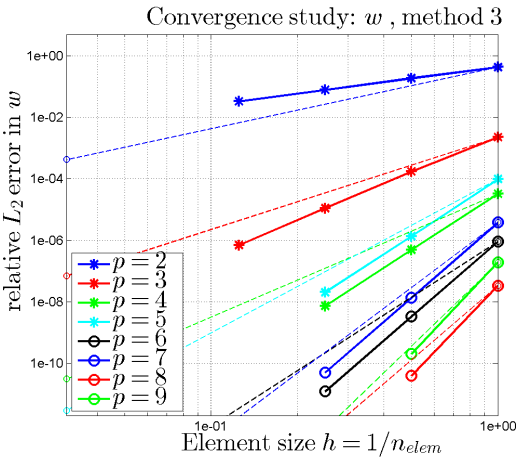

(a) Method 3, without BC in $\bar{q}_n$

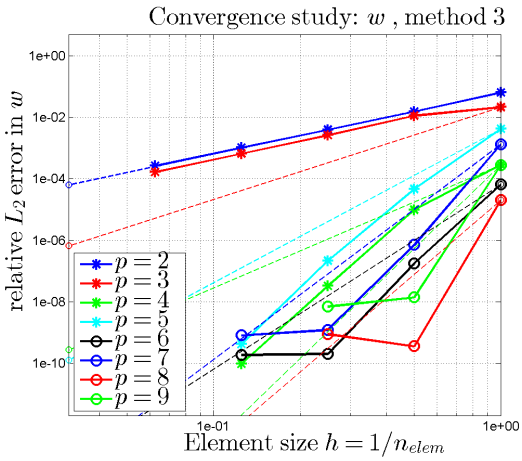

(b) Method 3, with BC in $\bar{q}_n$

Fig. 4.32: Convergence studies in w using quadrilateral elements

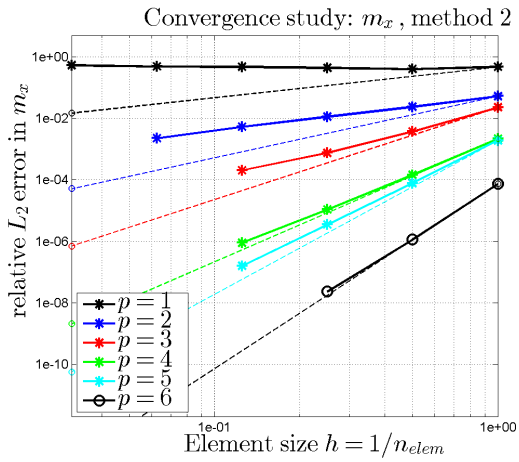

(a) Methods 1 and 2, with BC in $\bar{q}_n$

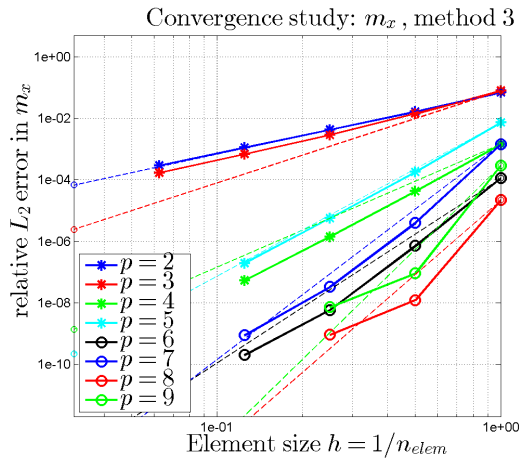

(b) Method 3, with BC in $\bar{q}_n$

Fig. 4.33: Convergence studies in m_x using triangular (l.) and quadrilateral (r.) elements

5 Conclusion

A mixed FEM for the approximation of the boundary value problem related to the Kirchhoff-Love Plate is verified by convergence studies and higher order convergence rates are achieved. Prescribing Dirichlet boundary conditions by introducing Lagrange multipliers, which are defined along the whole corresponding partition of the boundary of the domain, yields optimal convergence rates but also causes oscillations in most cases. These oscillations lead to nonconvergence of linear triangular elements but drastically decrease with order elevation.
Allowing arbitrary geometries, kinks in the boundary of the domain are inevitable, causing the unit outward normal to be discontinuous. As a result the solution fields feature jumps and kinks in the corners on the boundary of the domain, where edges with Lagrange multipliers corresponding to the same variables depending on the angle φ coincide. However, for an arbitrary domain with corners this does not *per se* hinder higher order convergence, as can be seen from the manufactured solution on the mapped square domain.
On the domains considered, all of the presented methods yield optimal convergence rates except for the square plate with constant load distribution, but sinusoidal load distribution and the manufactured solution resulted in convergence rates of $\mathcal{O}(h^p)$.
The examination of circular plates demonstrates the importance of proper higher-order meshes for optimal rates of convergence. It was found that for meshes which are generated by solving a shell problem in linear elasticity, the convergence rates were bounded. However, using transfinite mappings as proposed by *Šolin* [16], leads to meshes which enable optimal rates.
The introduction of the Kirchhoff effective shear force has significant impact on the quality of the approximation, with quadrilaterals being less sensitive than triangular elements, but again higher order convergence rates are not hindered *per se*.
Furthermore, the deformations are better approximated than the internal moments of the plate if disturbances are present in the mesh. Nevertheless the quantities of interest, which are the internal bending moments and shear forces besides the deformation of the plate, are directly obtained via solving the emerging linear system of equations.
Concerning the oscillations, which were found in most cases, the method may be further improved by reducing the number of collocation points or by choosing less degrees of freedom for the Lagrange multipliers or by decreasing the order of the one-dimensional Lagrange polynomials, which is a commonly known technique [5]. The Lagrange multipliers may lead to an over-constraint problem, nevertheless, optimal convergence rates were observed in the bulk of the studies conducted.
In conclusion, the aim of this thesis, to achieve higher order convergence rates on plates of arbitrary geometry possibly featuring curved boundaries with pinned, clamped, free or symmetry boundary conditions using standard Lagrange elements, was successfully gained.

Bibliography

[1] Hermann Ahrens and Dieter Dinkler. *Finite-Element-Methoden, Teil 2*. 1994.

[2] Holm Altenbach, Johannes Altenbach, and Konstantin Naumenko. *Ebene Flächentragwerke - Grundlagen der Modellierung und Berechnung von Scheiben und Platten*. Springer Vieweg, 2016.

[3] Ivo Babuška. "The finite element method with Lagrangian multipliers". In: *Numerische Mathematik* 20.3 (1973), pp. 179–192.

[4] Klaus-Jürgen Bathe. *Finite Element Procedures*. Prentice Hall, 2006.

[5] Daniele Boffi, Franco Brezzi, Michel Fortin, et al. *Mixed Finite Element Methods and Applications*. Springer, 2013.

[6] Franco Brezzi. "On the existence, uniqueness and approximation of saddle-point problems arising from Lagrangian multipliers". In: *Revue française d'automatique, informatique, recherche opérationnelle. Analyse numérique* 8.2 (1974), pp. 129–151.

[7] Philippe G Ciarlet and Pierre-Arnaud Raviart. "A mixed finite element method for the biharmonic equation". In: *Proceedings of Symposium on Mathematical Aspects of Finite Elements in PDE*. 1974, pp. 125–145.

[8] Sonia Fernández-Méndez and Antonio Huerta. "Imposing essential boundary conditions in mesh-free methods". In: *Computer methods in applied mechanics and engineering* 193.12 (2004), pp. 1257–1275.

[9] Gerhard A Holzapfel. *Nonlinear Solid Mechanics II*. John Wiley & Sons, Inc., 2000.

[10] Michael Jung and Ulrich Langer. *Methode der finiten Elemente für Ingenieure*. Springer, 2001.

[11] Christian Karpfinger. "Komplexe Zahlen–Polarkoordinaten". In: *Höhere Mathematik in Rezepten*. Springer, 2015, pp. 65–71.

[12] Gustav R Kirchhoff. "Über das Gleichgewicht und die Bewegung einer elastischen Scheibe". In: *Journal für die reine und angewandte Mathematik* (1850).

[13] Augustus E H Love. "The small free vibrations and deformation of a thin elastic shell". In: *Philosophical Transactions of the Royal Society of London. A* 179 (1888), pp. 491–546.

[14] Arpád Nádai. *Die elastischen Platten*. Springer, 1925.

[15] Claude-Louis Navier. "Extrait des recherches sur la flexion des plans elastiques". In: *Bull. Sci. Soc. Philomarhique de Paris* 5 (1823), pp. 95–102.

[16] Pavel Šolin, Karel Segeth, and Ivo Dolezel. *Higher-order finite element methods*. CRC Press, 2003.

[17] Stephen Timoshenko and Sergius Woinowski-Krieger. *Theory of Plates and Shells*. 2nd edition. McGraw-Hill, 1959.

[18] Olgierd C Zienkiewicz, Robert L. Taylor, and J.Z. Zhu. *The Finite Element Method: Its Basis and Fundamentals*. Elsevier, 2013.